Master's thesis

2019

Kathrine Albjerk Hamran

NTNU
Norwegian University of
Science and Technology
Faculty of Engineering
Department of Energy and Process Engineering

Kathrine Albjerk Hamran

Simulations and Measurements of Friction in Oscillating Flow

June 2019

NTNU
Norwegian University of
Science and Technology

NTNU
Norwegian University of
Science and Technology

NTNU
Norwegian University of
Science and Technology

Simulations and Measurements of Friction in Oscillating Flow

Kathrine Albjerk Hamran

Energy and Environmental Engineering
Submission date: June 2019
Supervisor: Pål-Tore Selbo Storli
Co-supervisor: Torbjørn Kristian Nielsen

Norwegian University of Science and Technology
Department of Energy and Process Engineering

Norwegian University of Science and Technology

Faculty of Engineering
Department of Energy and Process Engineering

EPT-M-2019

MASTER THESIS

for
student Kathrine Albjerk Hamran

Spring 2019

Simulations and measurements of friction in oscillating flow
Simuleringer og målinger av friksjon i oscillerende strømning

Background
The friction in oscillating flow in pipes and tunnels is not well described, despite being important for energy efficiencies and system stability. Without a good representation of such losses operation of hydraulic systems such as hydropower plants might be suboptimal. One example is rapid changes to the operating point of a hydropower plant, where flow oscillations are induced. Even if the operational scheduling is performed based on considerations optimising the revenues, the operation might not be optimised since losses from the oscillations are not included. At the Waterpower Laboratory at NTNU a test rig for oscillatory flow has been established. The test rig is intended for measurement of head loss, but measurements of more detail is of high interest.

Objective
The candidate should prepare for other measurements of energy losses in fluid flow, as well as establish numerical models for simulation of oscillation flow for testing different models representing losses in oscillatory flow.

The following tasks are to be considered:

1. Literature search on models of frictional losses in flowing fluids
2. Determine an experimental technique enabling results of higher level of detail than currently possible
3. Execute measurements, if possible with the new measurement capabilities installed, including recalibration of the flowmeter and on an additional pipe length for new frequencies of oscillations
4. Perform simulations of flow oscillations using different models of friction with different solution schemes
5. Investigate modifications of existing friction models to ensure a better fit with the experimental results
6. If the student will go to Nepal for an excursion, earlier and further work will be presented as a publication and presented at the conference; 9th *International symposium on Current Research in Hydropower Technologies (CRHT-IX)* at Kathmandu University

-- “ --

Address
N-7034 Trondheim
Norway

Location
K. Hejes vei 1b

Tel. +47 73 59 38 60
Fax +47 73 59 35 80
Org. no. NO 974 767 880

Within 14 days of receiving the written text on the master thesis, the candidate shall submit a research plan for his project to the supervisor.

When the thesis is evaluated, emphasis is put on processing of the results, and that they are presented in tabular and/or graphic form in a clear manner, and that they are analyzed carefully.

The thesis should be formulated as a research report with summary both in English and Norwegian, conclusion, literature references, table of contents etc. During the preparation of the text, the candidate should make an effort to produce a well-structured and easily readable report. In order to ease the evaluation of the thesis, it is important that the cross-references are correct. In the making of the report, strong emphasis should be placed on both a thorough discussion of the results and an orderly presentation.

The candidate is requested to initiate and keep close contact with his/her academic supervisor(s) throughout the working period. The candidate must follow the rules and regulations of NTNU as well as passive directions given by the Department of Energy and Process Engineering.

Risk assessment of the candidate's work shall be carried out, in cooperation with your supervisor, according to the department's procedures. The risk assessment must be documented and included as part of the final report. Events related to the candidate's work adversely affecting the health, safety or security, must be documented and included as part of the final report. If the documentation on risk assessment represents a large number of pages, the full version is to be submitted electronically to the supervisor and an excerpt is included in the report.

Pursuant to "Regulations concerning the supplementary provisions to the technology study program/Master of Science" at NTNU §20, the Department reserves the permission to utilize all the results and data for teaching and research purposes as well as in future publications.

The final report is to be submitted digitally in INSPERA. An executive summary of the thesis including title, student's name, supervisor's name, year, department name, and NTNU's logo and name, shall be submitted to the department as a separate pdf file. Based on an agreement with the supervisor, the final report and other material and documents may be given to the supervisor in digital format.

Submission deadline: 11 June 2019.

☒ Work to be done in lab (Water power lab, Fluids engineering lab, Thermal engineering lab)
☐ Field work

Department for Energy and Process Engineering 10/1 2019

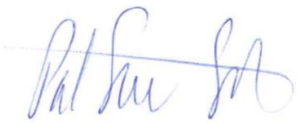

Pål-Tore Storli
Supervisor

Co-Supervisor(s): Torbjørn Kristian Nielsen

Abstract

The friction in transient mass oscillations in hydropower plants is not well described, despite the importance it has for energy efficiencies, system stability and optimization of the operational schedule of the hydropower plant. Experiments of transient mass oscillations between a small reservoir and a surge shaft have been conducted. Measurements of the flow rate and pressure were done with an electromagnetic flowmeter and pressure transducers, respectively. The oscillations in the hydraulic system were induced by closing a valve downstream of the surge shaft. The initial flow conditions in the experiments were steady flows with Reynolds number between 26 000 and 52 200.

The experimental results were compared with simulations in MATLAB. The transient equations were solved with two different solution methods, one where rigid liquid column theory was used and one where the method of characteristics was used. For both solution schemes, different friction models were tested. Among these were the quasi-steady friction model and a one-term model. Some modifications of the friction models were also investigated.

When the quasi-steady friction model was used within the method of characteristics scheme, the damping of the oscillations was underpredicted by the simulation compared to the experiment. The mean relative error for the local extrema was between 4.4% and 6.3% for the different flow rates. With the one-term model, the simulations yielded too much damping for the first five peaks, but for the following peaks, it did not yield enough damping. When the quasi-steady model was used within a rigid liquid column scheme, the results were closer to the measured values than with the method of characteristics. The mean relative errors between the simulations and the measurements for this case were between 1.45% and 1.70%. This was similar to the results obtained with the one-term model for the rigid liquid column simulations. One modification where the quasi-steady model and the one-term model were combined reduced the relative errors even further.

A few different measurement techniques which will enable more detailed experimental results were also discussed. Particle image velocimetry is suggested as the best method in this case for further investigations of the flow during transient mass oscillations.

Sammendrag

Friksjonen i massesvingninger i vannkraftverk er ikke tilfredsstillende beskrevet, til tross for at friksjonstapet er viktig for virkningsgraden og stabiliteten til systemet, og optimalisering av kjøreplanen for kraftverket. Forsøk med massesvingninger mellom et lite reservoar og en svingesjakt har blitt gjort. Volumstrøm og trykk ble målt med henholdsvis en elektromagnetisk volumstrømmåler og trykktransdusere. Massesvingningene ble indusert av at en ventil nedstrøms svingesjakten ble stengt. Før ventilen ble stengt, var strømningen gjennom systemet stasjonær med Reynolds tall mellom 26 000 og 52 200 for de ulike forsøkene.

Forsøksresultatene ble sammenliknet med simuleringer fra MATLAB. Likningene for transient strømning ble løst med to ulike metoder, en der det ble antatt stivt vann og rør, og en der karakteristikkmetoden ble brukt. For begge løsningsmetodene ble ulike friksjonsmodeller testet. Blant disse var en kvasi-stasjonær friksjonsmodell og en "one-term" modell. Noen modifiseringer av modellene ble også undersøkt.

Når den kvasi-stasjonære friksjonsmodellen ble brukt i løsningen med karakteristikkmetoden, resulterte det i at svingningene ikke ble dempet godt nok ut. Den gjennomsnittlige relative feilen for de lokale ekstremalpunktene var mellom 4.4% og 6.3% for de ulike volumstrømmene. Med "one-term" modellen ga simuleringene for mye demping av svingningene for de første fem toppene, og for lite demping for de etterfølgende toppene. Når den kvasi-stasjonære modellen ble brukt i simuleringer der vannet var antatt å være stivt, var resultatene nærmere de målte verdiene enn når karakteristikkmetoden ble brukt. Den gjennomsnittlige relative feilen mellom simuleringene og forsøket var i dette tilfellet mellom 1.45% og 1.70%. Dette var også svært likt de resultatene som ble oppnådd når "one-term" modellen ble brukt i simuleringene der vannet var antatt å være stivt. En modifikasjon der den kvasi-stasjonære modellen ble kombinert med "one-term" modellen reduserte de relative feilene ytterligere.

Ulike måleteknikker som kan gi mer detaljerte måleresultater ble også diskutert. "Particle image velocimetry" er foreslått som den beste metoden å gå videre med for nærmere undersøkelser av strømningen ved massesvingninger.

Preface

This master thesis was written as a part of a five-year degree in Energy and Environmental Engineering at the Norwegian University of Science and Technology. The thesis was written during the spring semester of 2019. The work has been challenging, educational and enjoyable.

Thanks are extended to my supervisor, Pål-Tore Storli, for help and guidance throughout the semester, and the other employees at the Waterpower Laboratory, especially to Trygve Opland for help with installing the pressure transducer on the rig, and to Joar Grilstad for general help in the laboratory.

Trondheim, 17.06.2019

Kathrine Albjerk Hamran

Contents

Abstract iii

Sammendrag iv

Preface v

List of Figures xi

List of Tables xii

Notation xiii

1 Introduction 1

1.1 Background . . . 1

1.2 Problems to be addressed . . . 1

1.3 Structure of the thesis . . . 2

2 Literature review 3

2.1 Empirically based models . . . 5

2.2 Physically based models . . . 6

2.3 Previous work . . . 6

3 Theory 7

3.1 Fluid transients . . . 7

3.2 Governing equations . . . 8

3.3 Methods of Solutions . . . 9

3.3.1 Method of Characteristics . . . 9

3.3.2 Rigid liquid column theory . . . 13

3.4 Energy loss . . . 14

3.5 Friction models . . . 15

3.6 Measuring principles . . . 16

3.6.1 Pressure Transducer . . . 16

3.6.2 Electromagnetic flowmeter . . . 17

3.7 Measuring frequency 18

3.8 Uncertainty 18

4 Discussion of available techniques for more detailed investigations 20

5 Method 23

5.1 Experimental rig 23

5.2 Risk assessment 25

6 Results and discussion 26

6.1 Experimental results 26

6.1.1 Calibration 26

6.1.2 Signal treatment 27

6.1.3 Uncertainty 29

6.1.4 Pressure measurements 32

6.1.5 Flow rate measurements 33

6.1.6 Water hammer 35

6.1.7 Level in the reservoir 37

6.1.8 Minor losses 38

6.2 Simulations 39

6.2.1 Method of Characteristics 39

6.2.2 Rigid Liquid Column Theory 46

6.2.3 Comparison 50

6.2.4 Modifications 54

7 Conclusion 59

8 Further work 60

Bibliography 61

Appendix A Derivation of the governing equations for fluid transients 65

Appendix B Derivation of the speed of sound 69

Appendix C Method of Characteristics **71**

C.1 Boundary conditions 73

C.1.1 Reservoir 73

C.1.2 Valve 74

C.1.3 Surge shaft 74

Appendix D Simplification of the governing equations with rigid liquid column theory **76**

Appendix E Calibration **78**

E.1 Calibration of the electromagnetic flowmeter 78

E.2 Calibration of the pressure transducers 78

Appendix F Experimental results **81**

Appendix G MATLAB code: Uncertainty calculations **84**

Appendix H MATLAB code: Method of Characteristics **95**

Appendix I MATLAB code: Rigid Liquid Column Theory **104**

Appendix J Risk assessment **119**

Appendix K Article for the CRHT-IX conference **143**

List of Figures

1 Dynamic response of the water level in the surge shaft of a hydropower plant. 8

2 Double characteristic grid. 10

3 Surge shaft. 13

4 Electromagnetic flowmeter. 17

5 Simplified drawing of the dynamic test rig in the Waterpower Laboratory 23

6 Raw data measurements from PT3 for the second valve closure with $Q = 0.007\text{m}^3/\text{s}$. 27

7 Measurements from PT3 after averaging. 28

8 Measurements from PT3. 28

9 Measurements from the EMF. 29

10 PT1 with error bounds. 30

11 PT2 with error bounds. 30

12 PT3 with error bounds. 31

13 PT4 with error bounds. 31

14 EMF with error bounds. 32

15 Pressure measurements from the four pressure transducers. Flow at steady state with $Q = 0.007$ m^3/s for the first 150 s, followed by a valve closure. 33

16 EMF measurements 34

17 Pressure measurements from PT3 with a zoomed view of the water hammer. 35

18 Water hammer. 35

19 The first pressure peak. 36

20 Pressure measurements from the transducer at the bottom of the reservoir. 38

21 Pressure measurement from all the pressure transducers. 38

22 Zoomed in view of all the pressure measurements. 38

23 Dimensionless valve opening, τ. 40

24 Simulation with MOC and the quasi-steady friction model compared with the pressure measurement. . 41

25 Simulation with MOC and the quasi-steady friction model compared with measurements for the first 100 s following the valve closure. 42

26 Relative error between the simulation and the measurement plotted at each extrema. 43

27 Simulations with MOC and the one-term friction model. 44

28 Simulations with MOC and the one-term friction model for the first 100 s after valve closure. 45

29 Relative error between the simulation with MOC and the measurements plotted at each extrema. . . . 45

30 Simulations with RLCT and quasi-steady friction model compared with measurements. 47

31 Simulations with RLCT and quasi-steady friction model compared with measurements for the first 150 s. 48

32 Relative error between the simulation with RLCT and the measurements plotted at each extrema. . . . 48

33 Results obtained with the one-term model in the RLCT simulations. 49

34 Results obtained with Vítkovský's model in the RLCT simulations. 49

35 Total head loss, friction loss and minor loss in the quasi-steady model in RLCT simulations. 51

36 Friction and minor loss in the quasi-steady model in RLCT simulations. 51

37 Total head loss, friction loss and minor loss in the quasi-steady model in MOC simulations. 52

38 Friction and minor loss in the quasi-steady model in MOC simulations. 52

39 Flow profile when the flow turns. 53

40 Simulations with modified one-term model with RLCT compared with measurements. 55

41 Simulations with modified one-term model with RLCT compared with measurements for the first 100 s. 55

42 Relative error in the simulations with the modified one-term model compared with the relative error in the original version of the one-term model. 56

43 Simulations with modified quasi-steady model with RLCT compared with measurements. 57

44 Relative error in the simulations with the modified quasi-steady model compared with the relative error in the original version of the quasi-steady model. 58

45 The shear, gravity and pressure forces acting on a fluid element with constant cross section A. 65

46 Control volume analysis for conservation of mass 66

47 Stoppage of frictionless liquid in horizontal pipe. 69

48 Control volume analysis for conservation of momentum. 69

49 Continuity relations in pipe. 70

50 Flow at the surge shaft junction. 76

51 Linear regression graph for the calibration of the electromagnetic flowmeter. 78

52 Linear regression graph for the calibration of the PT1. 79

53 Linear regression graph for the calibration of the PT2. 79

54 Linear regression graph for the calibration of the PT3. 80

55 Linear regression graphs from the calibration of the PT4. 80

56 Raw measurement data and averaged data from PT1. 81

57 Raw measurement data and averaged data from PT2. 81

58 Raw measurement data and averaged data from PT3. 82

59 Raw measurement data and averaged data from PT4. 82

60 Raw measurement data and averaged data from the EMF. 83

List of Tables

1 Minor loss coefficients. 15

2 The valves used in the rig. 24

3 Calibration coefficients for the electromagnetic flowmeter and the pressure transducers. 26

4 Maximum errors for the measurements, and percentage of maximum error that are due to systematic errors. 29

5 Maximum and mean random error, and the systematic error in the measurements. 29

6 Comparison of MOC simulations with the measurements. 46

7 Comparison of RLCT simulations with measurements. 50

8 Comparisons of the modified one-term model with the measurements. 56

9 Points used for the calibration of the electromagnetic flowmeter. 78

10 Points used for the calibration of the PT1. 79

11 Points used for the calibration of the PT2. 79

12 Points used for the calibration of the PT3. 80

13 The points used for the calibration of the PT4. 80

Notation

Symbols

ϵ	Roughness	[m]
μ	Dynamic viscosity	[kg/(m·s)]
ν	Kinematic viscosity	[m^2/s]
ω	Frequency	[Hz]
ρ	Density	[kg/m^3]
τ	Shear stress	[Pa]
A	Cross sectional area	[m^2]
a	Speed of sound	[m/s]
D	Internal pipe diameter	[m]
f	Friction factor	[-]
g	Gravitational acceleration	[m/s^2]
H	Piezometric head	[m]
h_f	Friction loss	[m]
h_L	Total head loss	[m]
h_m	Minor loss	[m]
K	Bulk modulus of elasticity	[Pa]
K_L	Minor loss coefficient	[-]
L	Length	[m]
p	Pressure	[Pa]
Q	Volumetric flow rate	[m^3/s]
Re	Reynolds number	[-]
t	Time	[s]
u	Velocity of pipe wall	[m/s]

V	Fluid velocity	[m/s]
x	Axial direction variable	[m]

Subscripts

t	Derivative with respect to time	[1/s]
x	Derivative with respect to x	[1/m]
ht	Headrace tunnel	
s	Surge shaft	
tur	Turbine	

Abbreviations

CTA	Constant Thermal Anemometry, Constant Thermal Anemometer
DAQ	Data acquisition
DPI	Digital Pressure Indicator
EMF	Electromagnetic flowmeter
LDA	Laser Doppler anemometry, Laser Doppler anemometer
MOC	Method of characteristics
NGU	Geological Survey of Norway
NI	National Instruments
PIV	Particle image velocimetry
PT	Pressure transducer
RLCT	Rigid liquid column theory

1 Introduction

1.1 Background

With increased focus on global warming, a shift towards a greener energy system is needed. The energy production from renewable sources is expected to increase in the coming years [1]. Many renewable sources, such as wind and solar energy, are unreliable because they are highly dependent on the weather. When a large portion of the electricity production comes from unreliable sources, there will be an increased need for a stable and reliable source that can complement the other sources. Due to its storage capacity and regulation abilities, hydropower is able to provide stability to the grid.

The increase of unreliable sources in the energy mix will also imply that a more dynamic operation of hydropower plants is required. The power output has to be adjusted often, and this will cause transients in the hydraulic system. When there are rapid changes in the water flow, a high pressure wave, often called a water hammer, will occur. Surge shafts are sometimes implemented between the reservoir and the turbine, because this reduces the potentially damaging high pressures of the water hammer. However, it will also cause the flow to oscillate between the reservoir and the surge shaft, when the flow rate through the turbine is regulated [2, Chapter 4].

The friction in unsteady, transient flow will be different than the friction in steady state flow [3]. Flow reversal will occur in transient flow, and this results in larger friction losses [4]. Existing friction models do not describe this friction very well. The friction damps out the oscillations and is thus important for system stability. Since the friction for oscillating flow is larger than the friction in steady state flow, the energy loss will also be larger. Using a friction model that accounts for this additional loss rather than a steady state friction model may therefore lead to a different optimal operational schedule for the hydropower companies. If a steady friction model is used, frequent regulation of the operating point may appear more optimal than it is in reality. A good description of the friction is therefore important for the efficiency of the power plant.

Thus, finding a good model for the friction in slow transient oscillations is important. The model should also be easy to use and efficient.

1.2 Problems to be addressed

This thesis investigates different models for friction in oscillating flow. The equations for transient flow are solved with two different solution schemes, one using rigid liquid column theory where the water is considered incompressible and the elasticity of the pipe is neglected, and the other using the method of characteristics which takes the compressibility of the water into account. Within each solution scheme, several different friction models are tested, and modifications of some models are investigated. The simulations with the different models are compared with experimental results from the test rig in the Waterpower Laboratory. Tests were carried out for different flow rates, and measurements of pressure and the flow rate were done. An experimental technique which will enable more detailed experimental results

from the test rig is also proposed.

1.3 Structure of the thesis

The thesis starts with a literature review of frictional losses in fluid flows. Different existing friction models and methods of solving the governing equations for transient flow are presented in the theory section. Experimental techniques enabling more detailed investigations of transient flow in the test rig are then presented and discussed. In the method chapter, the test rig and other things related to the experiments are presented. Following the method chapter, the results from the experiments and the simulations are presented and discussed. The conclusion summarizes the most important results from this thesis, before suggestions of further work are presented. There are several appendices attached to this thesis. The first few appendices contain derivations of the governing equations for transient flow, and more information on the solution methods that has been used, than what is presented in the theory section. The subsequent appendices contain additional data from the experiments. The MATLAB codes for the simulations and the uncertainty calculations are also included, as is the risk assessment for the experimental work. A part of this master thesis was to write and present a paper at a hydropower conference. The article that was written for the *9th International symposium on Current Research in Hydropower Technologies* at Kathmandu University, is therefore included in Appendix K.

2 Literature review

Mariotte is considered the first to directly study fluid friction [5, Chapter 1]. In the 17th century, he studied the drag of a stationary object in a moving stream [5, Chapter 1]. A more famed scientist who did studies related to fluid friction is Newton. In 1687 he proposed the law of linear viscosity, which states that the shear stress between fluid layers is proportional to the velocity gradient [5, Chapter 1]. This is valid for one-dimensional flow, i.e. flow that varies primarily in one dimension, of Newtonian fluids [6, Chapter 2]. Both air and water are examples of Newtonian fluids [5, Chapter 1]. The proportionality constant is the dynamic viscosity, μ, as seen in equation 1 [6, Chapter 2].

$$\tau = \mu \frac{du}{dy} \tag{1}$$

The viscosity causes a friction loss in flowing fluids. Different expressions for the energy or head loss caused by friction in pipe flows have been proposed throughout history. The following expression which relates the friction loss, h_f, to the velocity head, $V^2/(2g)$, was developed by Weisbach in the middle of the 19th century [7, Chapter 6].

$$h_f = f \frac{L}{D} \frac{V^2}{2g} \tag{2}$$

This is still the most widely used expression for the head loss caused by friction. The loss is related to the wall shear stress, and is caused by viscosity [6, Chapter 8]. Equation 2 is valid for both turbulent and laminar flows in pipes with smooth or rough surfaces [6, Chapter 8]. f is the Darcy friction factor. Darcy did experiments in 1857 which related pipe roughness to frictional resistance [7, Chapter 6]. Previously, Coulomb had done experiments in which it was discovered that the surface roughness had an effect on the friction, and after Darcy, several more experiments were done to establish the relation between pipe roughness, Reynolds number and the Darcy friction factor [7, Chapter 6]. Many of these experiments were done by Nikuradse in 1933 [6, Chapter 8]. Based on these experiments, different relations and charts have been made in order to relate f to these other parameters. Colebrook found an implicit relation for the friction factor in 1939, and Rouse and Moody made diagrams of the friction factor in 1942 and 1944, respectively [6, Chapter 8]. Moody's diagram, which plots f as a function of the relative roughness and the Reynolds number, is the most used today [6, Chapter 8]. Haaland proposed an explicit relation for the friction factor, which performs within 2% of Colebrook's equation [6, Chapter 8]. But even Colebrook's equation and Moody's diagram involve uncertainties, such as experimental error, the roughness size and curve fitting of the data, so the friction factor obtained with these methods should not be treated as exact either [6, Chapter 8]. Also, commercial pipes may differ from those in the experiments, in that the roughness may not be uniform, and the roughness may also change with time [6, Chapter 8].

For laminar flow, the effect of surface roughness on the friction is negligible [7, Chapter 8]. The friction factor is given by $f = 64/Re$ [6, Chapter 8].

The Darcy-Weisbach equation, equation 2, is commonly used as this is the most exact equation for the friction loss in steady state flow [8, Chapter 1]. Yet, many engineers in certain fields use other equations such as Manning's or Hazen-William's equations [9, Chapter 12].

When planning hydropower plants, it has been common to use Manning's formula for unlined tunnels [10, Chapter 3]. The formula is often used for open channel flow [9, Chapter 12]. It is not recommended for use in pipelines, except for in cases where the roughness dominates [9, Chapter 12]. Manning derived the formula in 1889, but a version of it was originally proposed by Gauckler in 1868 [11]. With Manning's formula, the friction loss may be expressed as

$$h_f = \frac{LV^2}{M^2 R^{4/3}}$$

where M is the Manning friction coefficient [10, Chapter 3].

Hazen-Williams formula is also much used, especially in water supply and sanitary engineering [12], despite that its range of applicability is limited and that errors may exceed 40% [13]. The formula is only applicable in the intermediate zone when flow is between laminar and turbulent flow [9, Chapter 12]. The equation is as follows, and was introduced in 1902 [12].

$$V = 0.849 C R_h^{0.63} S^{0.54}$$

Manning's and Hazen-William's equations have been much used in the past and is still used in some engineering fields, even though they no longer offer any significant advantage over the Darcy-Weisbach equation with friction factor from for example Colebrook's equation, since this is now easily found with the use of computers or advanced calculators [9, Chapter 12]. Use of the Darcy-Weisbach equation with Colebrook's formula or approximations of it is therefore recommended [9, Chapter 12].

In analysis of transient flow, steady friction relations in which the friction is related to the cross-sectionally averaged velocity have conventionally been expected to hold at every instant during the transient [4]. However, in a typical velocity profile for transient flow, there will be flow reversal near the wall, thus the cross-sectionally averaged velocity may be zero [4]. When traditional steady friction relations are used, this will give zero friction loss [4]. However, flow reversal will lead to higher shear stresses and thus larger frictional losses [4].

Despite this, most software programs for water hammer analysis use a constant friction factor [14]. Another common approach is to use a quasi-steady friction factor, where a steady friction expression, for example the Darcy-Weisbach equation, is updated at every instant during the transient [4].

But even with a quasi-steady friction model, discrepancies has been found between experiments and the numerical model. Vardy and Hwang [15] found that during the period when the mean flow is approximately zero, there is flow reversal close to the wall. This results in a large wall shear stress, which is not accounted for when a quasi-steady friction model is used [15]. Silva-Araya and Chaudhry [16] found that the relative error between experiments and computations of the pressure peaks with the quasi-steady model was 50% [16]. Pezzinga [17] solved the governing equations with an implicit finite difference scheme, and when a quasi-steady approach was used, he found that the relative error between the pressure peaks in the experiments and the simulations were around 19%.

Instead of using a steady or quasi-steady friction factor, a common approach in friction modelling is to express the friction factor as a sum of a quasi-steady part and an unsteady part [14].

Unsteady friction during a water hammer has been investigated for a long time [18], but friction during mass oscillations in hydropower plants has not been investigated quite as extensively, is the impression of this author. This could be because water hammers are a problem in many areas, including water distribution systems, irrigation systems and hydropower, whereas mass oscillations are mainly a problem in hydropower plants. Some of the friction models for water hammers, may be relevant for oscillating flow since many of the same flow phenomena such as flow reversal occur.

Gromeka was the first to include friction losses in the analysis of water hammers [3, Chapter 1]. In 1883, he assumed that the fluid was incompressible and that the friction losses were proportional to the velocity [3, Chapter 1]. Many more models for friction in water hammers have followed since, and different expressions for the unsteady friction term have been proposed. The models are often based on either empirical observations or physical considerations [4].

2.1 Empirically based models

Most of the empirically based models are based on the instantaneous acceleration [4]. Experiments conducted by Daily et al. in the 1950s showed that $\tau_{wu}(t)$ is positive for flow that accelerates and negative for decelerating flows [4]. This led them to propose the following model for the unsteady wall shear stress which includes the instantaneous local acceleration, $\partial V/\partial t$, of the flow, [4]

$$\tau_w = \tau_{ws} + \frac{k\rho D}{4}\frac{\partial V}{\partial t}.$$

The coefficient k says something about the deviations due to unsteadiness of the wall shear stress and momentum flux [4]. Daily et al. found the coefficient to be equal to 0.01 for accelerating flows and 0.62 for decelerating flows [4]. However, simulations have shown that the model yields poor agreements with experimental data when constant values of k are used [4].

Brunone et al. [19] modified Daily's model by incorporating the instantaneous convective acceleration, $\partial V/\partial x$ [14]. This modification yields good matches between experimental and computed results, when the coefficient k is found empirically by trial and error [14]. Because the model by Brunone agrees reasonably well with experimental results, and due to the simplicity of the model, it is the most used modification [4]. The equation for the unsteady friction f_u in Brunone's model is

$$f_u = \frac{kD}{V|V|}\left(\frac{\partial V}{\partial t} - a\frac{\partial V}{\partial x}\right).$$

Vítkovský found that Brunone's model gave the wrong sign for certain flow cases, such as for closure of a valve upstream in a simple pipeline [14]. He therefore proposed the following unsteady friction term, which gives the correct sign of the convective term for all flow cases [14]

$$f_u = \frac{kD}{V|V|}\left(\frac{\partial V}{\partial t} - a\mathrm{sign}(V)\left|\frac{\partial V}{\partial x}\right|\right).$$

2.2 Physically based models

The physically based models are almost all of the type called convolution based models, since they utilize the past history of the bulk acceleration in a convolution integral [18]. Most of these models are based on the model by Zielke [20]. By using Laplace transformations, Zielke derived an expression for wall shear for unsteady laminar flow [4]. The local acceleration and the history of local accelerations of the mean flow is included in the expression and linked to the wall shear stress by means of a weighting function and a convolution integral [18]. Zielke's model has turned out to be quite accurate for water hammers [4]. However, the model is very computationally demanding since all the previously calculated velocities must be stored [4]. Therefore efforts have been made to reduce the required memory storage and the computational times. Trikha approximated the weighting function by using three exponential terms, in such a way that only the velocities at the previous time step needs to be stored [4]. Others who have further developed and investigated the model by Zielke, include Suzuki et al. [21], Vardy et al. [22], and Vardy and Brown [23] among others [4].

2.3 Previous work

The work done in this thesis is a continuation of the project work done by the author in the fall of 2018. In the project work, the MATLAB code for solving the transient equations using rigid liquid column theory with Euler's method was established. Some experiments were also done in the rig, although at the time, the calibration coefficients used for the flowmeter were not correct. Thus, the other results and conclusions were probably not entirely correct either. Three different friction models and one model for oscillating flow in a U-tube were applied and compared with the experimental results nonetheless. The friction models, called the quasi-steady friction model, Vítkovský's friction model and the one-term friction model, did not provide enough damping compared with the measurements, while Ogawa's model for oscillating flow gave too much damping of the oscillations.

Previous work done by master students on this project has involved establishing the test rig in the Waterpower Laboratory and investigating some friction models, including developing the one-term friction model. This has been done by Rikstad [24] and Bergset [25].

3 Theory

3.1 Fluid transients

Flow can be split into steady and unsteady flow. In steady flow, the flow conditions in a point do not change with time, while in unsteady flow, the flow conditions vary with time [26, Chapter 1]. When the flow changes from one steady state to another, the flow is called transient flow [3, Chapter 1]. Examples of transient flow can be the flow after a pump has been started or stopped, flow after a change of valve opening, or flow in a hydropower plant after a change in power demand of the hydraulic turbine. The focus in this thesis is on the transient flow caused by the closing of a valve in a hydraulic system.

Transients can be split into fast and slow transients depending on how fast the flow changes occur [8, Chapter 8]. The size of the transient pressure which occurs after a velocity change is dependent on the size of the velocity change and how fast the change takes place [8, Chapter 8]. The water hammer is a fast transient, since the changes in velocity, and consequently pressure, occur rapidly. Whereas an example of a slow transient, in which the flow changes slowly, is the mass oscillations occurring between the surge shaft and the reservoir in a hydropower plant.

In order to reduce the effect of a water hammer in hydraulic systems, different measures can be taken. The valve can be closed more slowly or a surge shaft can be constructed [2, Chapter 4]. In hydropower plants, a surge shaft is a common way to reduce the pressure rise that occurs after the flow through the turbine has been stopped. A surge shaft introduces a free water surface closer to the turbine. Since the pressure rise in a water hammer is proportional to the length from the nearest free water surface upstream to the nearest free water surface downstream of the turbine, this reduces the effect of the water hammer [2, Chapter 4]. However, it introduces a new problem, namely mass oscillations. Due to the inertia of the water, the water masses will oscillate between the surge shaft and the reservoir, until the oscillations are damped out by the friction [10, Chapter 4].

During steady state operation of a hydropower plant, the friction and minor losses will cause a head loss, so that the water level in the surge shaft is lower than the reservoir level, as depicted in Figure 1a. When a valve downstream of the surge shaft is closed, the water in front of the valve will be decelerated. The water in the headrace tunnel, between the reservoir and the surge shaft, will move into the surge shaft causing a rise in water level there. Before the water masses in the headrace tunnel has stopped, the level in the surge shaft will be higher than the reservoir level, due to the inertia. Therefore, water will move from the surge shaft towards the reservoir, causing a decrease in the water level in the surge shaft. The flow will oscillate back and forth between the surge shaft and the reservoir, as seen in figure 1b. [2, Chapter 4]

Figure 1c shows the dynamic response of the water level when the valve is opened again. In this case, the water from the surge shaft will move through the valve first, since it takes time to accelerate the water in the headrace tunnel. Thus, the level of the free water surface in the surge shaft will reduce. After a while the flow in the headrace tunnel will gain a higher flow rate than that of the flow through the valve, due to inertia. The excess water will therefore move into the

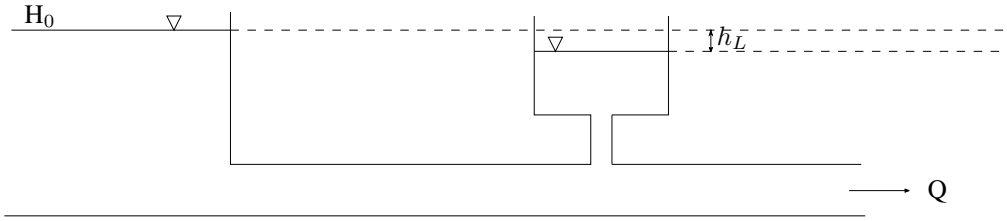

(a) Head loss, h_L, during steady state operation of a hydropower plant. The reservoir is to the left, and the surge shaft in the middle.

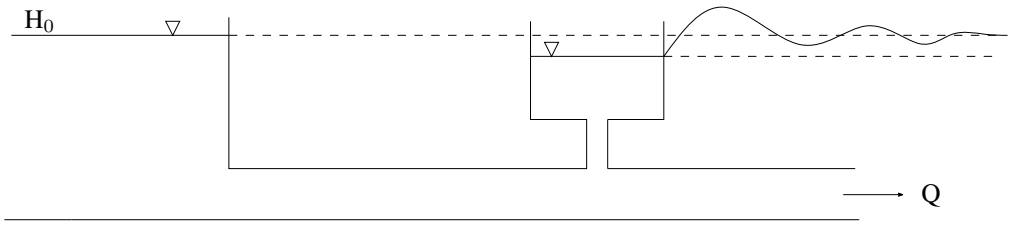

(b) Change in water level in the surge shaft after a valve is closed downstream. Based on figure in [2, Chapter 4].

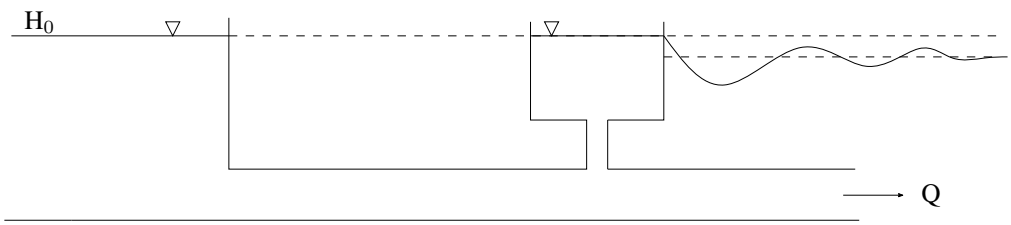

(c) Change in water level in the surge shaft after a valve is opened downstream. Based on figure in [2, Chapter 4].

Figure 1: Dynamic response of the water level in the surge shaft for (a) steady state, (b) after valve closure, and (c) after valve opening. Based on figures in [2].

surge shaft, causing the level to rise again. These mass oscillations will, for both the case of valve opening and closing, oscillate until they are damped out by the friction. [2, Chapter 4]

3.2 Governing equations

The equations governing transient flow in pipes can be derived from conservation of mass and continuity. This is shown in renowned books such as Wylie and Streeter's Fluid Transients in Systems [26, Chapter 2]. Derivation of the equations was also done as a part of the preliminary project work leading up to this master thesis [27], and an extract of the derivations is included in Appendix A.

Assuming that a slightly compressible fluid flows in a prismatic tube at low Mach number, the continuity and momentum equation for transient flow, expressed in terms of the piezometric head, H, are equation 3 and equation 4, respectively [26, Chapter 2].

$$H_t + \frac{a^2}{g} V_x = 0 \tag{3}$$

$$H_x + \frac{1}{g}V_t + h'_f = 0 \tag{4}$$

These equations are often referred to as Allievi's equations [28]. In equation 4, h'_f is the head loss per unit length. The a in equation 3 is the speed of sound, which for a thick-walled or rigid pipe is given by the bulk modulus of elasticity, K, and the density of the fluid, ρ, as follows [26, Chapter 1]

$$a = \sqrt{K/\rho} \tag{5}$$

The speed of sound may be around 1200 m/s in pure liquid in a pipe, however regular water normally contains small amounts of air, so that the speed of sound is usually around 900-600 m/s [9, Chapter 13].

3.3 Methods of Solutions

Equation 3 and 4 are partial differential equations, which generally must be solved by numerical methods. Solution by the characteristics method and solution with rigid liquid column theory are two common methods. Historically, the graphical method has been used [26, Chapter 5]. And an implicit finite difference method and a finite element method have also been used [26, Chapter 5]. In this thesis, the governing equations were solved with the method of characteristics and with rigid liquid column theory. These two methods are therefore described more in detail below, while the other methods are not discussed.

3.3.1 Method of Characteristics

The most popular method to solve the transient equations 3 and 4 is the method of characteristics due to its accuracy, simplicity and numerical efficiency [4]. Analysis with this method uses elastic theory where the elasticity of the pipe and the compressibility of the fluid are included [8, Chapter 9]. The method is most often applied to water hammer problems, but it can also be used for surge calculations, however computing times would be longer due to the small time step required for the method [8, Chapter 9].

The method and the equations involved in the characteristics method are described in brief in the following paragraphs, and a slightly more thorough description of the method is included in Appendix C. The method transforms the partial differential equations 3 and 4 into ordinary differential equations. Equation 3 and equation 4 are combined linearly by multiplying equation 3 with an unknown multiplier, τ, and adding it to equation 4 [26, Chapter 3]. The values of the multiplier can then be chosen in such a way that the equations correspond to the total derivative of H and V. By doing this, the following ordinary differential equations are developed.

$$\frac{g}{a}\frac{dH}{dt} + \frac{dV}{dt} + gh'_f = 0 \tag{6}$$

$$-\frac{g}{a}\frac{dH}{dt} + \frac{dV}{dt} + gh'_f = 0 \tag{7}$$

These equations are called the C^+ and C^- equations, and are only valid along the characteristic lines defined by $\frac{dx}{dt} = +a$, and $\frac{dx}{dt} = -a$, respectively. The characteristic lines define a grid in the space-time plane as seen in Figure 2. Solution of equation 6 and 7 can be found at the nodes of the grid made up by the characteristic lines by using finite differences. When the initial conditions and the boundary conditions are known, the solution at the newest time step can be found from the solution at the previous time step. In that way information travels forward along the characteristic lines [18].

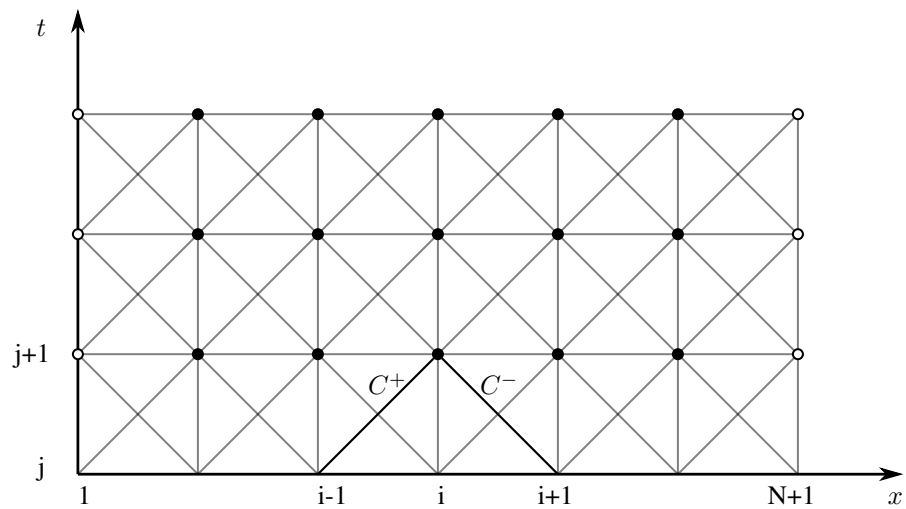

Figure 2: Double characteristic grid. Based on figure in [3, Chapter 3].

Different grids can be chosen. Figure 2 shows a double grid where numerical solutions of H and Q are found at every node. Another common type of grid is a diamond-shaped grid where solutions are found at alternate grid intersection points [26, Chapter 3]. The diamond-shaped staggered grid is less computationally demanding than the double grid for the same required accuracy, but it requires that the pipe is divided into an even number of reaches [26, Chapter 3].

A pipe of length L is divided into N sections of length Δx. With a double characteristic grid solution is found at N+1 grid points, or nodes. The time step for the iteration is given by

$$dt = dx/a. \tag{8}$$

Solving the characteristic equations with finite differences leads to the following equations

$$H_{i,j+1} = H_{i-1,j} - B(Q_{i,j+1} - Q_{i-1,j}) - RQ_{i,j+1}|Q_{i-1,j}|$$

for the positive characteristic, and

$$H_{i,j+1} = H_{i+1,j} + B(Q_{i,j+1} - Q_{i+1,j}) + RQ_{i,j+1}|Q_{i+1,j}|$$

for the negative characteristic, with B as the pipeline characteristic impedance,

$$B = \frac{a}{gA} \tag{9}$$

and R as the pipeline resistance coefficient, $R = \frac{f\Delta x}{2gDA^2}$ [26, Chapter 3]. Derivation of this can also be seen in Appendix C. The i indices denote grid points along the x-axis, and j indicate the time level.

The C^+ and C^- equations may be rewritten as

$$H_{i,j+1} = C_P - B_P Q_{i,j+1} \tag{10}$$

and

$$H_{i,j+1} = C_M + B_M Q_{i,j+1} \tag{11}$$

with the constants

$$C_P = H_{i-1,j} + BQ_{i-1,j} \tag{12}$$

$$C_M = H_{i+1,j} - BQ_{i+1,j} \tag{13}$$

$$B_P = B + R|Q_{i-1,j}| \tag{14}$$

$$B_M = B + R|Q_{i+1,j}| \tag{15}$$

From equations 10 and 11 one can get the following expression for $H_{i,j+1}$

$$H_{i,j+1} = \frac{C_P B_M + C_M B_P}{B_P + B_M}$$

and $Q_{i,j+1}$ can then be found from the equation 10 or 11 or from $Q_{i,j+1} = \frac{C_P - C_M}{B_P + B_M}$ [26, Chapter 3].

At the interior points of the pipe, i.e. for $i = 2 : N$ for a single straight pipe, the head and flow rate may be found with the equations above when the initial state is known. Solutions to transient problems usually begins with steady state conditions at time zero, so that the initial head and flow rate are known [26, Chapter 3]. But in order to find solutions at new time steps for all nodes along the pipe, the boundary conditions must also be known. For a hydraulic system consisting of a reservoir, a pipe, a surge shaft and a valve at the downstream end, boundary conditions must be prescribed at the reservoir, the junction between the pipe and the surge shaft, and at the valve.

The initial head in the pipe is found by computing the friction and minor losses along the length of the pipe when the flow through the pipe is equal to the initial flow rate. The initial flow rate through the valve is found with the discharge coefficients, if available, or if the initial flow rate is known, the initial Q may be set equal to the initial flow rate in the system.

At a large reservoir, the head is constant during a transient, so at the first node, $H_{1,j+1} = H_{res}$ when entrance losses are ignored [26, Chapter 3]. The flow rate is found with the C^+ equation, equation 10. When entrance losses are included, the equation for the head at the first node is

$$H_{1,j+1} = H_{res} - (1 + k)\frac{Q_{1,j+1}^2}{2gA^2}$$

where k is the loss coefficient [26, Chapter 3]. Combining this with equation 11 yields the following expression for the flow rate

$$Q_{1,j+1} = \frac{-B_M + \sqrt{B_M^2 - 4k_1(C_M - H_{res})}}{2k_1}$$

with $k_1 = \frac{1+k}{2gA^2}$. The head at the first node, $H_{1,j+1}$ can then be found from equation 11.

At the downstream end of the pipeline, the closure of the valve is expressed in terms of a dimensionless valve opening, τ, relating the discharge coefficient, C_d, times the area of valve opening, A_G, to the same steady quantities, $\tau = \frac{C_d A_G}{(C_d A_G)_0}$ [26, Chapter 3]. For zero flow, $\tau = 0$, and for steady flow of Q_0, $\tau = 1$ [26, Chapter 3]. The flow rate at the valve is given by

$$Q_{N+1} = -B_P C_v + \sqrt{(B_P C_v)^2 + 2C_v C_P}$$

where B_P is as in equation 14, C_P as in equation 12 and $C_v = (Q_0\tau)^2/(2H_0)$ [26, Chapter 3]. Derivation of this equation is also shown in Appendix C. The dimensionless valve opening, τ, is often given as a function of time, t. One expression for τ is the following

$$\tau = \tau_i - (\tau_i - \tau_f)\left(\frac{t}{t_c}\right)^{E_m} \tag{16}$$

where τ_i is the initial value of the valve opening, τ_f is the final value, t_c is the time of operation, and E_m is 0.75 [26, Chapter 3]. When a valve goes from fully open to fully closed, $\tau_i = 1$ and $\tau_f = 0$. τ_c is the time it takes before the valve is fully closed. And for t larger than t_c, the value of τ is equal to zero. The head at the valve is found from equation 10 [26, Chapter 3].

At the junction between the horizontal pipe and the surge shaft, the flow into the surge shaft is defined as positive into the tank as seen in Figure 3. In order to find the head and flow rate at the surge shaft, the continuity equation and the energy equation is used at the intersection between the pipe and the surge shaft, in addition to the C^+ and C^- equations [8, Chapter 9]. Head loss at the junction is neglected, and the water level in the surge shaft is assumed to change relatively little during one time interval, Δt [8, Chapter 9]. The water level in the surge shaft can then be found either with a first or second order approximation [8, Chapter 9]. The equations for the surge shaft, when the second order approximation is used, is presented here. More information of how these equations are found, is included in Appendix C. The first order approximation is also described in the appendix, but the following second order approximation is recommended [8, Chapter 9].

$$H_{i,j+1} = H_{i,j} + \frac{\Delta t(Qs_{j+1} + Qs_j)}{2A}$$

When this approximation is used, the flow at the surge shaft, $Q_{i,j+1}$, is

$$Q_{i,j+1} = \frac{C1 + C3}{2 + C2}$$

with $C1 = 2A\frac{C_P - H_{i,j}}{\Delta t} - Qs_j$, $C2 = 2\frac{AB}{\Delta t}$ and $C3 = \frac{C_P - C_M}{B}$ [8, Chapter 9]. $H_{i,j+1}$ can then be found from the C^+ equation, and $Q_{i+1,j+1}$ from the C^- equation. The flow into the surge shaft, Qs, can be found from the continuity equation at the junction, $Q_{i,j+1} = Qs_{j+1} + Q_{i+1,j+1}$ [8, Chapter 9]. The head at the first node downstream of the surge shaft, $H_{i+1,j+1}$ is equal to the head at the surge shaft, when losses at the junction are neglected.

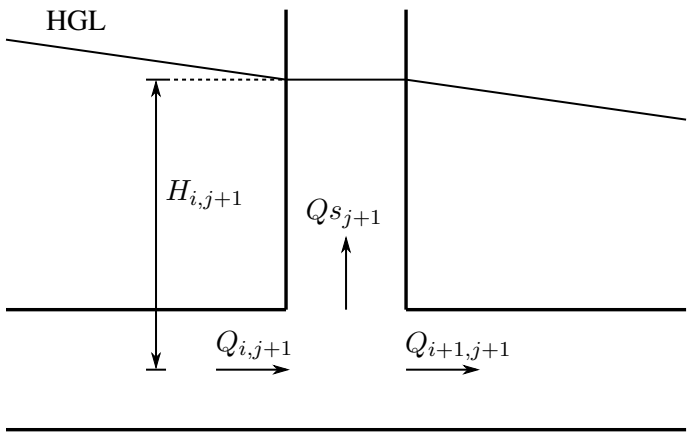

Figure 3: Surge shaft. Based on figure in [8, Chapter 9].

3.3.2 Rigid liquid column theory

For mass oscillations, rigid liquid column theory is often applied. This means that the tunnel walls are considered rigid and the water is considered incompressible [26, Chapter 5]. Consequently, the bulk modulus of elasticity of the fluid, $K = \frac{\Delta p}{\Delta \rho / \rho}$, will go to infinity, since the mass density remains constant [26, Chapter 5]. Thus, the speed of sound, a, as given by equation 5 will go to infinity, and one effectively assumes that there is a common fluid particle velocity along the pipe and that all flow changes is transmitted instantly throughout the system [26, Chapter 5].

With rigid liquid column theory, the continuity equation 3 becomes

$$Q = -A\frac{dz}{dt} \tag{17}$$

and the momentum equation 4 is reduced to

$$\frac{L}{gA}\frac{dQ}{dt} = z - h_f \tag{18}$$

where L is the length of the pipe, A is the cross-sectional area of the pipe, Q is the flow rate, z is the height of the free surface in the surge shaft, and h_f is the head loss [29]. Details on how the governing transient equations are transformed into the ordinary differential equations above, equation 17 and 18, are shown in Appendix D.

These ordinary differential equations can be solved with different numerical methods such as the Euler method, or higher order methods such as the fourth order Runge-Kutta method [29].

The Euler method is a first-order method for solving initial value problems, i.e. ordinary differential equations where the initial conditions are known [30, Chapter 7]. For an initial value problem of the following form, $y' = f(x, y)$, with initial condition, $y(x_0) = y_0$, the explicit Euler method yields the following approximations of the exact solution $y(x)$

$$y_{j+1} = y_j + hf(x_j, y_j)$$

where h is the step length [30, Chapter 7], and

$$x_{j+1} = x_j + h.$$

For equation 17 and equation 18, the step length, h, corresponds to the time step, Δt. For equation 17, solution with an explicit Euler method yields

$$z_{j+1} = z_j - \Delta t \frac{Q}{A}$$

with

$$t_{j+1} = t_j + \Delta t$$

Similarly, for equation 18, the Euler method yields

$$Q_{j+1} = Q_j + \Delta t \frac{gA}{L}(z - h_f)$$

also with equation 3.3.2. Since this method is first order accurate in time, the time step should be quite small in order to ensure that the solution is sufficiently accurate.

When rigid column theory is used, an approximate formula for the frequency of the mass oscillation can be found by considering a system without losses. This is shown in Appendix D. The frequency, ω, is

$$\omega = \sqrt{\frac{gA_t}{LA_s}}, \tag{19}$$

where A_t is the cross-sectional area of the pipe, A_s is the cross-sectional area of the surge shaft, and L is the length of the water column [2, Chapter 4].

The time period of the oscillations will thus be [2, Chapter 4]

$$T = \frac{2\pi}{\omega}. \tag{20}$$

3.4 Energy loss

The energy loss in pipe flows consists of the friction loss, h_f, and the minor loss, h_m. The friction loss arise due to the viscosity of the fluid [6, Chapter 8]. While the minor loss is due to changes in geometry of the pipe and other obstructions in the flow, such as valves, bends, tees, and inlets. Obstructions like these induce flow separation and mixing, and this cause additional losses [6, Chapter 8]. The energy loss is often expressed in terms of the equivalent fluid column height, and is then termed the head loss [6, Chapter 8].

The minor loss is given by the following expression

$$h_m = \frac{K_L * Q^2}{2gA^2} \tag{21}$$

where K_L is the loss coefficient [6, Chapter 8]. Estimates of loss coefficients for different geometries can be found in various tables in fluid mechanics books. But the flow pattern past obstructions is dependent on the specific design of the component, and the loss coefficients may therefore vary greatly depending on the exact details of the design from each manufacturer [7, Chapter 6]. Values listed in general tables are usually average values of different designs, and may have errors as high as 50% [7, Chapter 6]. So if available, loss coefficients for the specific components, provided by the manufacturer, should be used for increased accuracy. Some select coefficients are shown in Table 1.

Table 1: Minor loss coefficients from [7, Chapter 6].

Component	Minor loss coefficient [-]
Inlet	0.35
Flanged tee, branch flow	0.61
Fully open gate valve	0.12

Accurate expressions for friction loss in steady flow are well known, while expressions for friction loss in unsteady, transient flow are still disputed. Some friction models are described below, starting with the established model for steady flow, before moving on to models that have been proposed for unsteady flow.

3.5 Friction models

The most common expression for friction loss in steady state flow is the Darcy-Weisbach equation. It relates the Darcy friction factor, f, to the head loss in the following way.

$$h_{\mathrm{f}} = f \frac{L}{D} \frac{Q^2}{2gA^2} \tag{22}$$

The friction factor can be found from Moody's diagram or a formula approximating Moody's diagram. The friction factor is a function of the Reynolds number, $Re = \frac{\rho V D}{\mu}$, and the relative roughness of the pipe walls, ϵ/D. For laminar flow, i.e. flow where the Reynolds number is smaller than 2300, the friction factor is independent of ϵ/D [31]. In this case, f may be found with the following formula [31]

$$f = 64/Re \tag{23}$$

For turbulent flow, $Re > 2300$, several formulas are in use to find Darcy's friction factor. One of these is the explicit Haaland equation [31].

$$\frac{1}{\sqrt{f}} = -1.8 \log \left[\left(\frac{\epsilon/D}{3.7} \right)^{1.11} + \frac{6.9}{Re} \right] \tag{24}$$

For unsteady, transient flow, experiments have shown that the friction is different from that in steady flow [3, Chapter 2].

Different models for this unsteady friction have been proposed. One such model is the quasi-steady friction model [4]. The Darcy-Weisbach equation is used, but the friction term is updated at each instant in time, with the instantaneous flow values [18].

Many friction models add an unsteady term to the quasi-steady friction term. Vítkovský's friction model is one of them. As mentioned, Vítkovský's model is a formulation of Brunone's friction model for fast transients [14]. The unsteady part of the friction term is, in this model, dependent on the instantaneous local acceleration, $\partial V/\partial t$, and the instantaneous convective acceleration, $\partial V/\partial x$ [14]. With Vítkovskýs formulation, the unsteady friction term, $h_{f,u}$, can be found in the following way [14].

$$h_{f,u} = \frac{kD}{V|V|} \left(\frac{dV}{dt} + a \cdot sign(V) |\frac{dV}{dx}| \right) \frac{L}{D} \frac{Q^2}{2gA^2} \tag{25}$$

k is the Brunone friction coefficient which can be found empirically or with Vardy's shear decay coefficient, C [14]. When Vardy's coefficient is used, k can be found from $k = \frac{\sqrt{C}}{2}$ with $C = 0.00476$ for laminar flow and $C = \frac{7.41}{Re^{\log\left(\frac{14.3}{Re^{0.05}}\right)}}$ for turbulent flow [14].

Jonsson, Ramdal and Cervantes [32] found that the convective acceleration term is negligible compared to the quasi-steady parts and the time dependent parts in Vítkovský model. Thus, the model can be further simplified to [33]

$$h_{f,u} = \frac{kD}{V|V|}\frac{dV}{dt}\frac{L}{D}\frac{Q^2}{2gA^2}. \tag{26}$$

Bergset [25] proposed a one-term friction model which was based on multiplying the quasi-steady model with a correction factor. He suggested the following expression for the head loss,

$$h_f = B^{\frac{1}{g}\left(\frac{\partial V}{\partial t} + V\frac{\partial V}{\partial x}\right)} \cdot f \cdot \frac{L}{D}\frac{V|V|}{2g} \tag{27}$$

where B is a constant that can be found by looking at the friction loss of a pipe with two sections of different diameters [25]. Thus, the suggested expression for B was

$$B = \left(\frac{f_1}{f_2} \cdot \left(\frac{D_1}{D_2}\right)^5\right)^{g\Delta x/(V_1(V_2 - V_1))} \tag{28}$$

where the subscripts denote the two different sections of the pipe [25].

3.6 Measuring principles

Good experimental measurements are important in order to verify the accuracy of theoretical models. For friction losses in oscillating flow, measurements of the pressure and flow rate are important. Pressure and flow rate can be measured in different ways. Pressure can be measured with for example manometers, Bourdon tubes or pressure transducers [6, Chapter 3]. Flow rate can be measured with different types of flowmeters. Some examples are Coriolis flowmeters, obstruction-type flowmeters, ultrasonic flowmeters, and electromagnetic flowmeters [34, Chapter 16]. In this thesis, four pressure transducers and one electromagnetic flowmeter was used to obtain pressure and flow rate measurements. The principle behind these two measurement methods will be briefly described below.

3.6.1 Pressure Transducer

Pressure transducers convert changes in pressure into changes in an electrical signal, for example a voltage signal [6, Chapter 3]. Pressure transducers of different types can measure gage, absolute and differential pressure. Gage pressure transducers use the atmospheric pressure as reference [34, Chapter 15]. Absolute pressure transducers measure pressure referenced to vacuum [34, Chapter 15]. The sum of the atmospheric pressure and gauge pressures equals the absolute pressure [34, Chapter 15]. The atmospheric pressure is dependent on the altitude and the weather conditions [6, Chapter 3].

Modern pressure transducers work on the principle that a diaphragm between two chambers stretches when there is a change in pressure across it [6, Chapter 3]. For gauge pressure transducers one chamber is open to the atmosphere [34, Chapter 15]. The movement of the diaphragm is measured by a displacement transducer, and converted to a voltage signal [34, Chapter 15].

3.6.2 Electromagnetic flowmeter

The measuring principle for an electromagnetic flowmeter is based on Faraday's law of induction [35]. According to Faraday's law a varying magnetic field induces a voltage in a conductor. The induced voltage is proportional to the mean flow as given by the following equation,

$$\vec{U} = (\vec{V} \times \vec{B}) \cdot D$$

where $\vec{U}$ is the voltage, $\vec{V}$ is the mean flow velocity, $\vec{B}$ is the magnetic field strength and D is the inner diameter of the flowmeter.

In a typical electromagnetic flowmeter the magnetic field, $\vec{B}$, is induced by a current flowing through coils as seen in Figure 4 [36]. When an electrically conductive fluid is moving through the pipe, a voltage will be induced. Electrodes placed on either side of the pipe will then record the size of the induced voltage in the fluid. Since the induced voltage is proportional to the velocity, the corresponding velocity can be found. The flow rate is then found by multiplying the velocity by the cross-sectional area of the pipe.

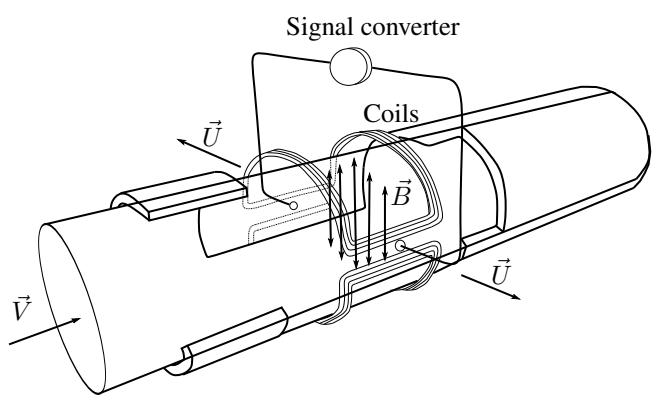

Figure 4: Electromagnetic flowmeter. Figure based on [37].

For an electromagnetic flowmeter to work, the fluid in the pipe must be electrically conductive. Pure distilled water is not electrically conductive, but regular tap water, and water such as used in this experiment, contains enough ions so that it is electrically conductive [6, Chapter 8].

A signal converter is used to amplify the signal from the electrodes, filter it and process it for output [35]. The signal converter also supplies the field coils with current [35].

Full-flow electromagnetic flowmeters (EMFs) are non-intrusive and do not cause head loss [6, Chapter 8]. EMFs can measure in both directions of flow [35]. The accuracy of EMFs are unaffected by changes in temperature, density, pressure and viscosity [38, Chapter 6]. In addition, they are minimally influenced by asymmetrically distorted flow profiles and swirls [35]. EMFs are robust and largely maintenance free since they have no mechanically moving parts [35].

3.7 Measuring frequency

When measuring oscillations one must use a sufficiently high sampling frequency in order to avoid signal aliasing. The Nyquist frequency is often used to find an adequate sampling frequency. It states that the sampling frequency, $\omega_{sampling}$, should be at least twice as big as the frequency in the system to be measured, ω_{system}, as seen in equation 29 [39, Chapter 4].

$$\omega_{sampling} \geq 2 \cdot \omega_{system} \tag{29}$$

3.8 Uncertainty

A measurement is only an estimate of the value of the measurand, the quantity one wishes to measure [40]. The uncertainty related to the estimate should therefore be included, whenever measurements are done [40]. Errors in the measurement can be divided into two categories; systematic errors, and random errors [34, Chapter 3].

Systematic errors may be due to system disturbances, environmental changes, use of uncalibrated instruments, and drift in instrument characteristics, among other things [34, Chapter 3]. Some systematic errors are due to the level of accuracy inherent in the measuring instruments, and are quantified by the value of the accuracy given by the manufacturer [34, Chapter 3]. When the overall systematic error is to be calculated, the errors are not combined by addition of each separate systematic error [34, Chapter 3]. This would give a worst-case prediction of the maximum error, however it is considered very unlikely that the errors are at their maximum or minimum values at the same time [34, Chapter 3]. Instead, the root-sum-square method is usually applied when combining the errors [34, Chapter 3].

Random errors, also called precision errors, are caused by random and unpredictable effects, that yield perturbations of the measurement, with positive and negative errors occurring in approximately equal numbers [34, Chapter 3]. Random errors can for example be due to electrical noise [34, Chapter 3]. Random errors also often arise when measurements are done by human observation [34, Chapter 3]. The random errors can be reduced by taking the average of several measurements of the same quantity [34, Chapter 3]. However, the random error cannot be reduced to zero, as this would require an infinite number of measurements [34, Chapter 3]. Instead, one may assign a certain confidence level where the measurement is expected to lie within some error bounds [34, Chapter 3]. The random error can be found by statistical analysis [34, Chapter 3]. When the number of measurements of a quantity is small, the student-t distribution should be used instead of the normal distribution, to find the possible deviation of the mean measurements from the

true measurement value [34, Chapter 3]. Upper and lower bounds for the expected true value of x can be expressed as

$$\bar{x} - \frac{\mathrm{t}_{\alpha/2}\sigma}{\sqrt{n}} \leq \hat{x} \leq \bar{x} + \frac{\mathrm{t}_{\alpha/2}\sigma}{\sqrt{n}}$$

where $\bar{x}$ is the mean value found from the n measurements, and $\hat{x}$ is the true value of x [34, Chapter 3]. $\mathrm{t}_{\alpha/2}$ is the t-value for a student-t distribution with a confidence level of $1-\alpha$, and σ is the standard deviation [34, Chapter 3]. The mean is given by [41, Chapter 8].

$$\bar{x} = \sum_{i=1}^{n} \frac{x_i}{n}$$

The standard deviation is given by [41, Chapter 8]

$$\sigma = \sqrt{\sum_{i=1}^{n} \frac{(x_i - \bar{x})^2}{n-1}}$$

where n is the number of measurements.

4 Discussion of available techniques for more detailed investigations

In order to gain a better understanding of the friction in mass oscillations, more detailed knowledge of the flow is wanted. This should be obtained by more detailed measurements in the experiments. Since the friction is related to the shear stresses in the flow, which again is related to the velocity profile, measurements of the velocity profile is desirable. Velocity measurements can be obtained in several ways. Thermal anemometry, PIV and LDA are the most commonly used techniques for velocity measurements [42].

Thermal anemometry uses small sensors or probes to measure the velocity [42]. The most common type of thermal anemometry is called constant thermal anemometry (CTA), where the sensor is electrically heated and kept at a constant temperature [42]. The velocity is found by measuring the convective heat loss from the sensor to the surrounding. By keeping the sensor at a constant temperature, a voltage drop across the sensor corresponds to the power dissipated by the sensor [42]. When the flow conditions are constant, the heat generated by the current in the resistance wire is balanced by the heat loss to the surrounding fluid [42]. When the velocity of the fluid changes, the heat loss from the sensor, and thus the measured voltage across the sensor, also changes [43]. Two different types of sensors are common. Cylindrical hot-wire or hot-film sensors are most often used to measure the velocity, while flush hot-film sensors are used to measure wall shear stress [43]. The hot-wire sensors consist of a circular resistance wire, and interferes with the flow slightly [43]. Hot-film sensors are made up of a film with a coating of an electrically conductive material and may be mounted flush to the wall, so as not to disturb the flow [43].

CTA has been successfully used for measurements of air flows and measurements of turbulence in air flows [42]. For measurements in water flows, the sensors do not have the same accuracy as in air flows and they may become unstable [44]. Hot-film sensors are more suitable for water flows since they are more robust than hot-wire sensors [45]. One example has been found where CTA was used for measurements in transient flow. Sundstrom and Cervantes [33] used hot-film sensors to find the wall shear stress in the flow in a pipe after a valve was closed. The initial flow was with Reynolds number $1.7{\cdot}10^6$ and $0.7{\cdot}10^6$ [33]. In order to obtain reliable results, the sensors had to be calibrated before and after each measurement set by using an approximate calibration approach [33]. They included an error bound of $\pm 40\%$, and attributed any difference smaller than this to turbulent fluctuations. They studied the wall shear stress for the first nine seconds after valve closure, and they concluded that the shear stress seemed to change sign during the transient, even though the CTA was not able to measure the direction of the shear stress.

Upon contact with Dantec Dynamics, it was made clear that hot-wire sensors that measure the velocity cannot be used for measurements in flow where flow reversal occurs because the sensor is too fragile. However, hot-film sensors for wall shear measurements can be used for measurements in flow with flow reversal. But, as Sundstrom and Cervantes experienced, they are not able to measure the direction. The calibration of CTA shear probes is another drawback of the measuring method according to Dantec Dynamics. The output voltage has to be calibrated against known shear stresses in steady flows. And because the sensors are so sensitive, they have to be calibrated frequently.

Miller [46] investigated the sensitivity in position of hot-film shear probes when they are used for wall shear stress

measurements. He found that a change in position of the sensor of 0.3 mm could result in errors of 50% in the computed shear stress [46].

Lodahl, Sumer and Fredsøe [47] used flush mounted hot-film probes to measure the wall shear stress in a combined oscillatory flow. To avoid uncertainties related to the direction of the measured shear stress, they measured the velocity just above the shear stress probe with a two-component laser Doppler anemometer [47].

Laser Doppler Anemometry (LDA) can be used to measure the instantaneous particle velocities by utilizing the Doppler effect [42]. By seeding the flow with small particles that follow the flow, one can study the movement of these particles and use that to find the fluid velocity [42]. By illuminating the flow with a laser beam, the particles will reflect this light [42]. Since the particles are moving, the frequency of the light will shift as it is refracted from the particles [42]. The difference in frequency between the incident beam and the refracted light from the moving particles is proportional to the particle velocity [42].

He and Jackson [48] used LDA to measure the local velocity in pipe flow. They studied the velocity during increase and decrease of the flow rate. They found that the mean velocity measurements had a total combined uncertainty of less than 10%. This was mostly due to limitations in the repeatability of the experiment, the uncertainty in the LDA frequency-velocity coefficient and the accuracy of the frequency tracker [48].

Vennatrø [28] successfully measured the longitudinal and tangential component of the velocity in oscillatory flow with LDA.

Brunone et al. [49] used an ultrasonic Doppler velocimeter to find the velocity field during transient conditions. Thus, instead of measuring the frequency shift between emitted and refracted light beams, the frequency shift between emitted and reflected ultrasonic pulses is used to find the velocity of the particles in the flow [49]. Brunone et al. [49] obtain velocity profiles at several instants during a transient water hammer. One drawback they experienced with the velocity measurements is that it may be difficult to separate the measurement errors from the turbulent fluctuations since it is difficult to repeat the experiments in detail [49].

Hughes and How [50] measured the velocity distribution in pulsatile flow with an ultrasonic Doppler velocimeter. The average error in a velocity measurement was found to be $7.9 \pm 0.9\%$.

Particle image velocimetry is another measuring technique which can be used to obtain measurements of the velocity components. When PIV measurements are used, the flow must be seeded with particles that can be used to trace the flow, but they should not alter the flow [42]. Pictures are taken of the flow, and the local velocity can be found by measuring the displacement of the particles from different images and dividing by the time between the exposures [42].

Doorne and Westerweel [51] measured all three components of the velocity field in a cross section for both laminar and turbulent pipe flows with PIV. They found that the dominant error in the measurements were so-called registration errors from the calibration [51]. When they compared the measurements to direct numerical simulations, they found that the accuracy of the measurements were within 1% of the mean axial velocity.

Sundstrom and Cervantes [52] successfully used PIV to measure the axial and radial velocity components in pulsating and accelerating flow.

PIV and Doppler measuring techniques are both non-intrusive. The hot-film anemometer must be placed inside the pipe, and may therefore interfere with the flow, unless it is mounted flush to the pipe wall. The hot-film sensors do not measure the direction, whereas with PIV or LDA measurements, the direction of the velocity is measured. A drawback of both PIV and LDA is that optical aberrations may be a problem, but there exists methods to minimize this, such as using a water jacket, where the circular pipe is placed inside a rectangular water tank with plane walls [53].

Based on the things discussed here, and in line with the recommendations from the representative from Dantec Dynamics, PIV measurements are recommended to obtain measurements of the flow profile.

The Waterpower Laboratory has a PIV system of the type FlowSense 2M which could be used for the measurements.

5 Method

5.1 Experimental rig

The experiments were done in a rig which consists of a water tank, a horizontal pipe and a surge shaft and siphon system. A simplified drawing of the test rig is shown in Figure 5. Water is pumped up from the sump and supplied to the water tank. The water tank is 1.15 m in diameter and 2.775 m tall, with an internal morning glory spillway which ensures that the level in the tank does not exceed approximately 2.4 m. A 21 m long horizontal pipe connects the reservoir to the surge tank and siphon system. The pipe has an internal diameter of 0.15 m, and is made of steel except for a small section which is made of Plexiglas. The surge shaft also has a diameter of 0.15 m, and the height of the surge shaft is 2.7 m from the middle of the horizontal pipe. The rig can also be run as a siphon system, by making use of the bend at top. As seen in Figure 5, there are four valves on the rig, two gate valves (1 and 4) and two butterfly valves (2 and 3). Valve 4 is used to control the flow rate. Valve 1 is kept fully open. When the rig is run with a traditional surge shaft, valve 2 is fully open as well, and valve 3 is used to initiate the transient. So valve 3 is fully open initially and then it is closed to generate the mass oscillations. The specification for each valve is summarized in Table 2.

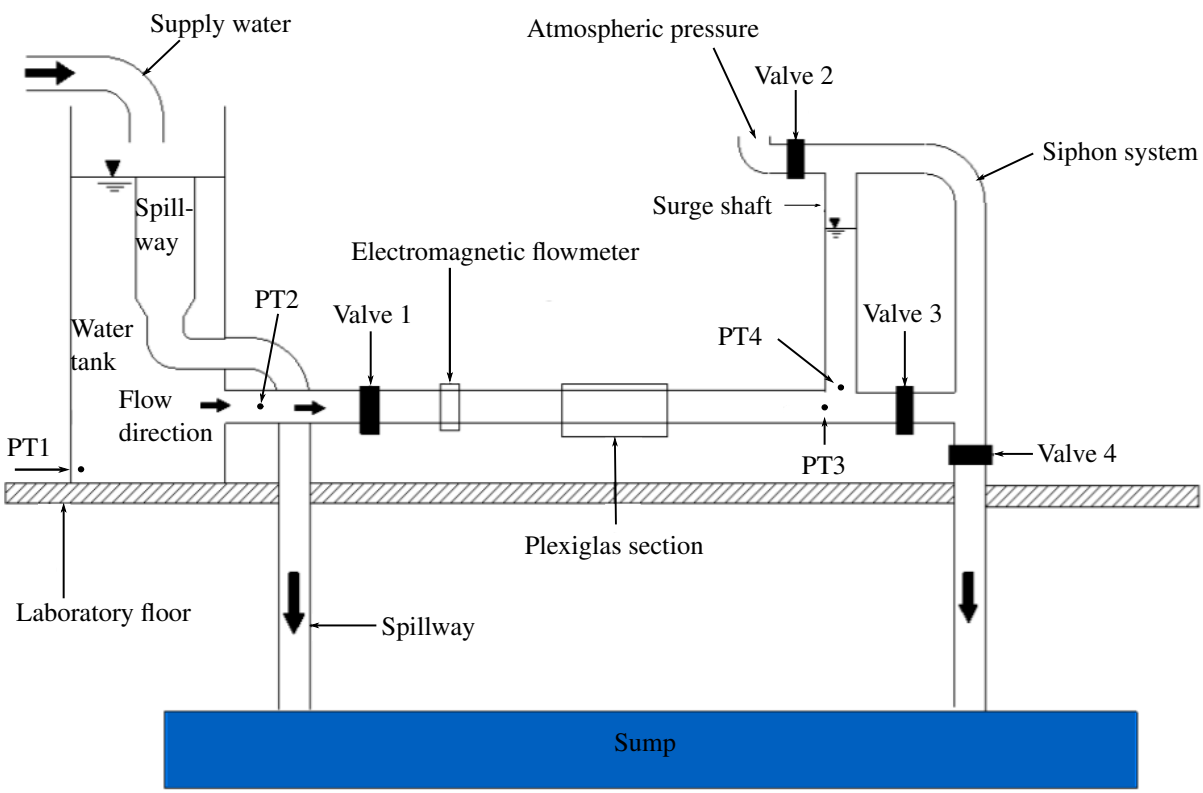

Figure 5: Simplified drawing of the dynamic test rig in the Waterpower Laboratory. Figure from [25], not drawn to scale.

Table 2: The valves used in the rig [25].

Name	Type	Function in surge shaft set-up
Valve 1	VAG BETA 300-EKOplus gate valve	Dry the pipe system
Valve 2	EBRO butterfly valve	Air control into the surge shaft
Valve 3	EBRO butterfly valve	Initiate the transient
Valve 4	VAG BETA 300-EKOplus gate valve	Control the flow rate

The flow rate is measured with an electromagnetic flowmeter from Krohne. The flowmeter, OPTIFLUX 2000, is used in combination with an IFC 300 signal converter, and the combination is called OPTIFLUX 2300C [36]. The maximum measuring error for the flowmeter is given by the manufacturer as 0.2% of the measured value [36].

Pressure is measured on four different places on the rig. A PTX1400 pressure transducer from GE Druck has been installed near the bottom of the water tank, in order to monitor the water level in the tank. The other three pressure transducers are of the type UNIK 5000 from GE Druck. The pressure transducers are labelled as shown in Figure 5, PT1, PT2, PT3, and PT4. All the pressure transducers in the rig are referenced to gauge. The PT1, which was the PTX1400, has a measuring range from 0 to 2.5 bar gauge, and an accuracy of $\pm 0.15\%$ of the full-scale value [54]. The other three pressure transducers have a range from 0 to 5 bar gauge, and the accuracy is given as $\pm 0.04\%$ of the full-scale value [55].

The pressure transducers give an output signal between 4 and 20 mA. Data acquisition from the measuring instruments was done with a NI USB-6211 device which converts the current signals into voltages. A logging program made in LabVIEW was used to log the measurements from the flowmeter and the pressure transducers. The logging frequency was 200 Hz. Post-processing was done in MATLAB.

Calibration of the flowmeter and the pressure transducers was done. The calibration constants, c_1 and c_2 in equation 30, were found by linear regression in Excel.

$$y = c_1 \cdot x + c_0 \tag{30}$$

In equation 30, x is the value in Volt, and y is the measured value in the desired unit.

The pressure transducers were calibrated by the use of a digital pressure indicator (DPI) from Druck which exerted a known pressure on the transducers. The DPI 601 has an accuracy of $\pm 0.05\%$ of the full-scale value [56].

The flowmeter was calibrated using another electromagnetic flowmeter from Krohne, which is situated in the rig after the pump, and had recently been calibrated by another student, and by using the pressure measurements in the tank to make sure that the level in the tank was constant without any flow going into the spillway. The recorded values in LabVIEW in Volt was also compared with the values stated on the flowmeter-display in m^3/h.

Measurements were done for different flow rates. Five valve closures were done for each flow rate. Flow rate and pressure was measured, including measurements of the level in the water tank, which had not been done before on this rig. PIV measurements were not done, as this equipment was used by other students at the time. Measurements were

also only done on the existing pipe length, as the area beyond the surge shaft was occupied by other projects, so that experiments on additional pipe lengths could not be tested.

5.2 Risk assessment

The risk assessment for the work in this master thesis is included in Appendix J. A risk assessment was performed before the execution of the experiments in the fall semester. Since the same rig was used with no new measuring methods, the same risk assessment was found satisfactory for the experimental work this semester as well.

6 Results and discussion

Experiments on the transient flow following valve closures were done for flow with initial Reynolds number in the range from 26 000 to approximately 52 200. Initial flow rates equal to 0.0035 m^3/s, 0.006 m^3/s and 0.007 m^3/s, were tested and analyzed. The plots presented in this section are from the experiment where the initial flow rate was 0.007 m^3/s. This corresponded to flow with Reynolds number, Re=52 166. Flow is considered fully turbulent for $Re \geq 4000$, thus the flow before valve closure is turbulent in all the test cases [6].

6.1 Experimental results

6.1.1 Calibration

The flowmeter was calibrated against another flowmeter located in the pipe after the pump. This master meter had known calibration constants. By monitoring the level in the water tank, to ensure that the level stayed constant and no flow went through the spillway, a comparison was made and new calibration coefficients were found. The voltage output from the flowmeter was also compared with the values in m^3/h on the digital display on the IEC 300 converter of the flowmeter, and the values on the display also seemed to be correct. The new calibration constants that were found for the flowmeter are shown in Table 3. These coefficients transforms the voltage signal into m^3/h. The flow rate was therefore divided by 3600 to yield the flow rate in m^3/s.

Calibration of the pressure transducers were done with a pressure indicator which excerted a known pressure on the pressure transducers. As for the flowmeter calibration, linear regression was done in Excel. The points that were used for the calibration of the pressure transducers and the flowmeter are included in Appendix E. The resulting calibration coefficients for the pressure transducers, which are used to convert the logged voltage signal to bar, are presented in Table 3. The pressure was then converted to meter water column by dividing by the gravitational acceleration and the density of the water.

Table 3: Calibration coefficients for the electromagnetic flowmeter and the pressure transducers.

Instrument	c_1	c_0
EMF	24.933	-49.83
PT1	0.3140	-0.6427
PT2	0.6254	-1.2558
PT3	0.6234	-1.2484
PT4	0.6240	-1.2532

After the experiments, the pressure transducers were calibrated once more to check the drift of the output signals from the transducers. The drift was found to be minimal, and error from drift of the signal was therefore neglected in the uncertainty analysis. The flowmeter was not recalibrated after the experiments, due to lack of time.

6.1.2 Signal treatment

The measurements were done with a frequency of 200 Hz. This resulted in raw data with some noise. An example of the raw data signal from one pressure measurement after a valve closure is shown in Figure 6. The signal is quite messy, and it was found that it was difficult to compare this signal with the simulations. Therefore the data was averaged every 20th sampling point. Thus, instead of having measuring points every 0.0050 s, an average is taken and plotted every 0.1 s. This reduces the frequency to 10 Hz, but as the frequency of the mass oscillations is 0.6838 Hz according to equation 19, a frequency of 10 Hz is more than sufficient according to Nyquist's sampling theorem, seen in equation 29. Doing this averaging introduce additional uncertainty in the system which is accounted for in the uncertainty calculations below. The averaging reduces a lot of the random noise in the signal, which after averaging becomes the signal shown in Figure 7.

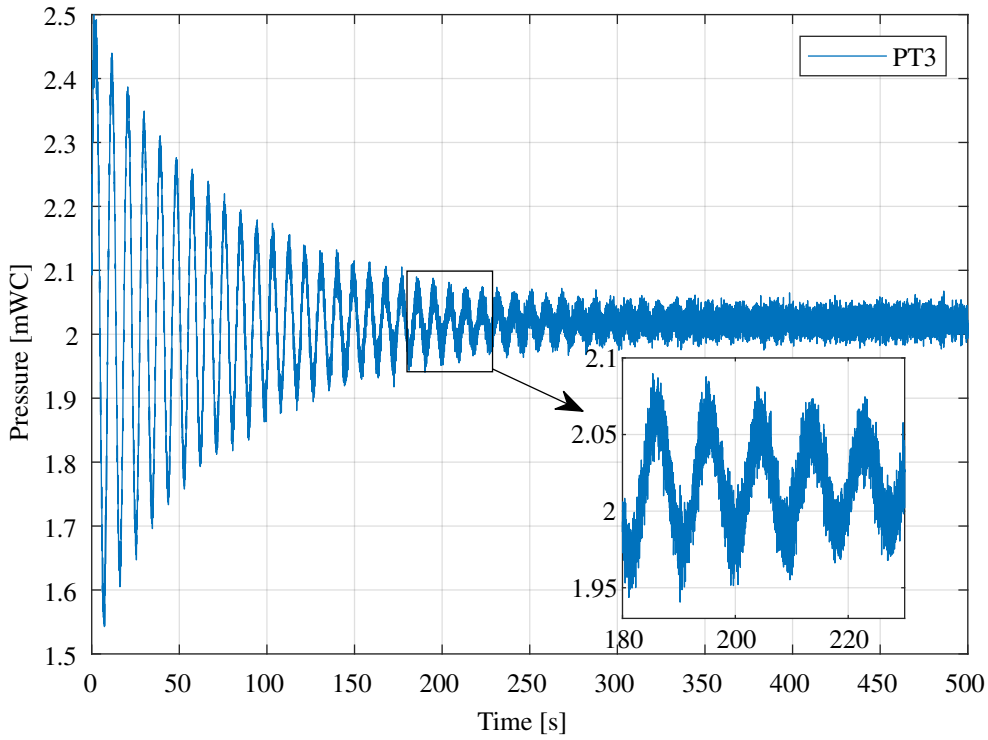

Figure 6: Raw data measurements from PT3 for the second valve closure with $Q = 0.007\text{m}^3/\text{s}$.

For each flow rate, the valve closure was repeated five times to check the consistency of the results. For the experiments with flow rate equal to 0.007 m^3/s the pressure measurements from PT3 for each closure is plotted together in Figure 8a. The results showed good consistency, with no extreme outliers. The average of the five runs is shown in Figure 8b. Similar plots for the flow rate is shown in Figure 9, while the plots for PT1, PT2 and PT4 are included in Appendix F. The average of the five runs is used for the comparisons with the simulations, and the uncertainty connected to the averaging is included in the uncertainty analysis below.

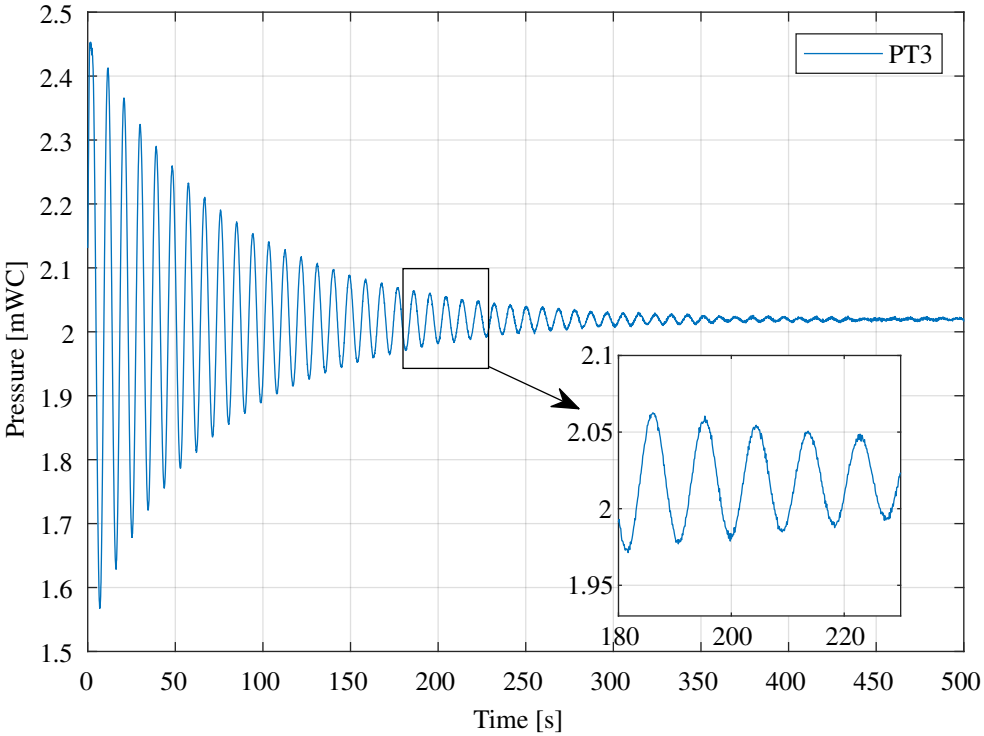

Figure 7: Measurements from PT3 after averaging.

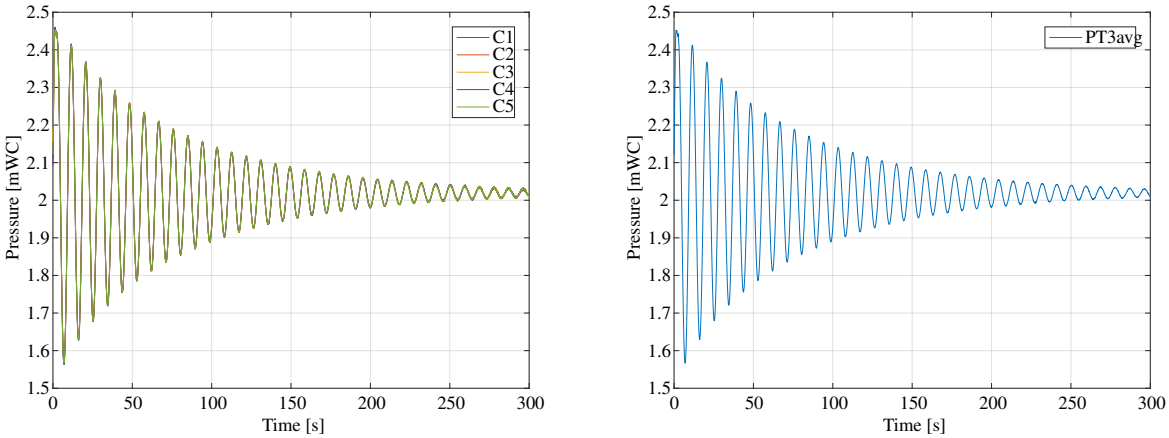

(a) All PT3 measurements for the five closures plotted together.

(b) Average of the five PT3 measurements.

Figure 8: Measurements from PT3.

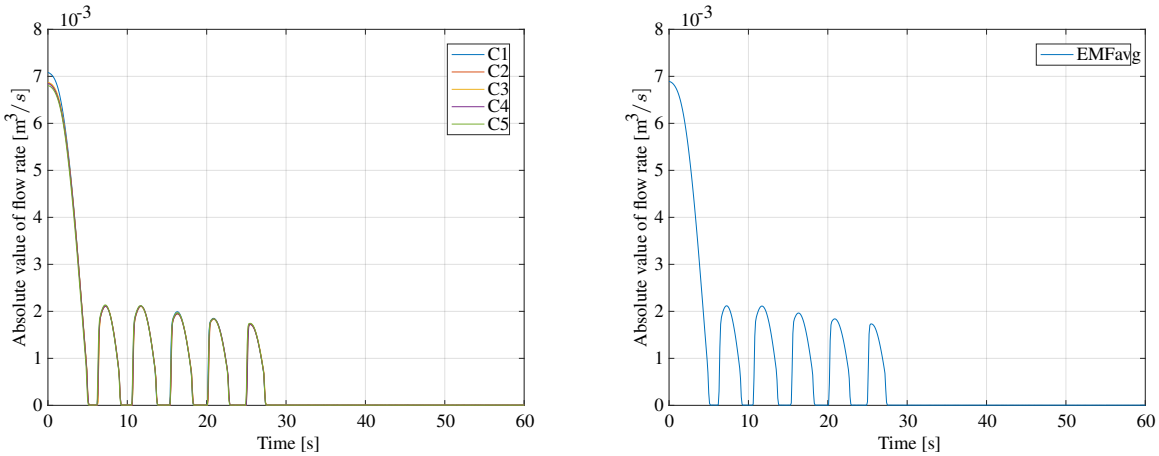

(a) All EMF measurements for the five closures plotted together.

(b) Average of the five EMF measurements.

Figure 9: Measurements from the EMF.

6.1.3 Uncertainty

The maximum deviation between the measurements and the error limits is shown in Table 4. The error is relatively large for most of the measurements. The systematic error contributes the most to the total error. Over 80% of the maximum error is due to systematic error for all measurement instruments, and as much as 99.8% of the maximum error is from the systematic error for one of the pressure transducers.

Table 4: Maximum errors for the measurements, and percentage of maximum error that are due to systematic errors.

Instrument	Maximum measurement error	Systematic error in percentage of maximum error
EMF	0.0013 m^3/s	84.6 %
PT1	0.0638 mWC	99.8%
PT2	0.0551 mWC	99.6%
PT3	0.0569 mWC	96.5%
PT4	0.0574 mWC	95.6%

The random error is low compared to the systematic error. Table 5 shows the maximum and mean random errors and the systematic error of the measurements.

Table 5: Maximum and mean random error, and the systematic error in the measurements.

Instrument	Max random error	Mean random error	Systematic error
EMF	7.11e-04 m^3/s	8.29e-06 m^3/s	0.011 m^3/s
PT1	0.0026 mWC	9.54e-04 mWC	0.0637 mWC
PT2	0.0054 mWC	0.0013 mWC	0.0549 mWC
PT3	0.0149 mWC	0.0025 mWC	0.0549 mWC
PT4	0.0167 mWC	0.0024 mWC	0.0549 mWC

The measurements from each measuring instrument is plotted together with the error bounds in Figures 10 to Figure 14.

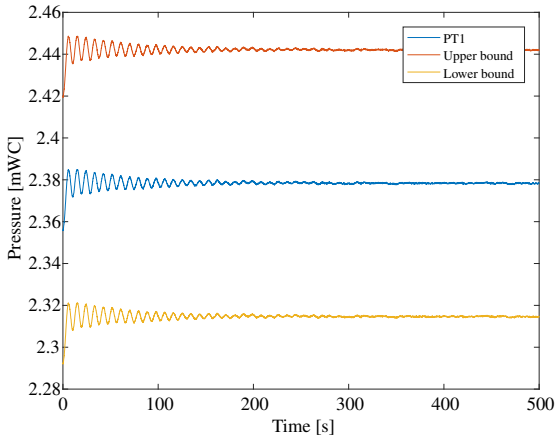

(a) PT1 measurement with error bounds.

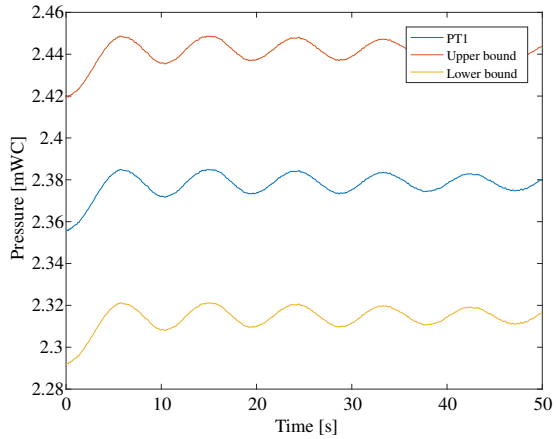

(b) Closer view of PT1 measurement with error bounds.

Figure 10: PT1 with error bounds.

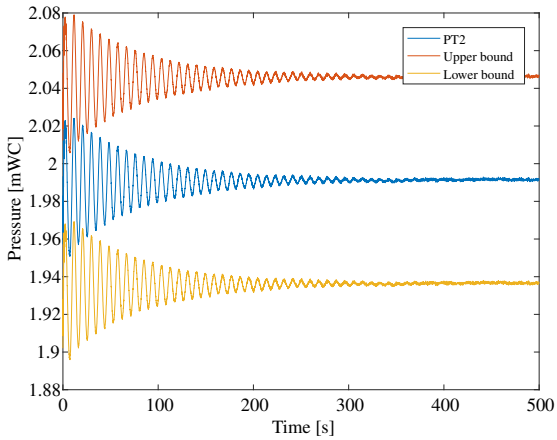

(a) PT2 measurement with error bounds.

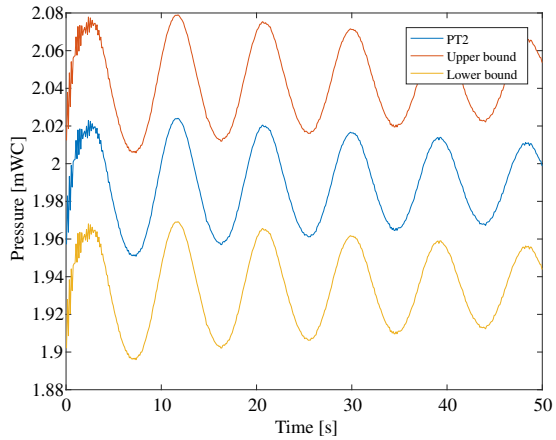

(b) Closer view of PT2 measurement with error bounds.

Figure 11: PT2 with error bounds.

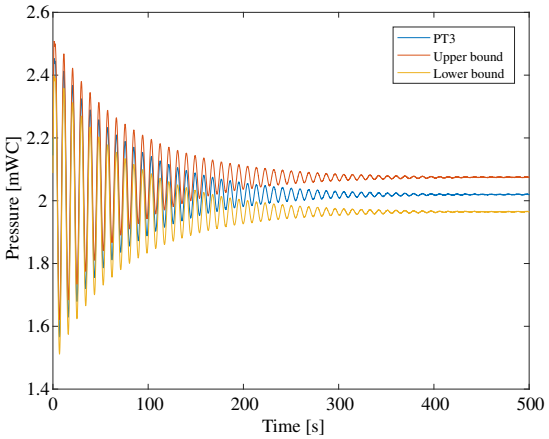

(a) PT3 measurement with error bounds.

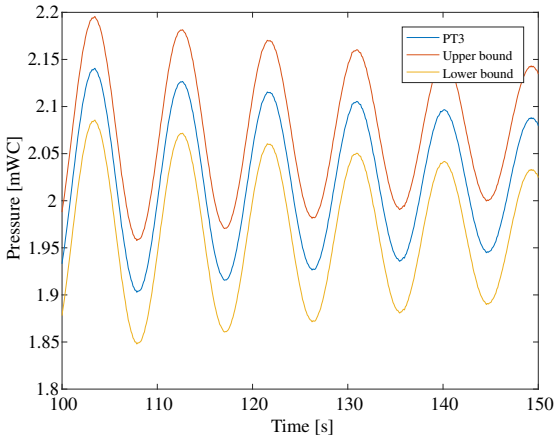

(b) Closer view of PT3 measurement with error bounds.

Figure 12: PT3 with error bounds.

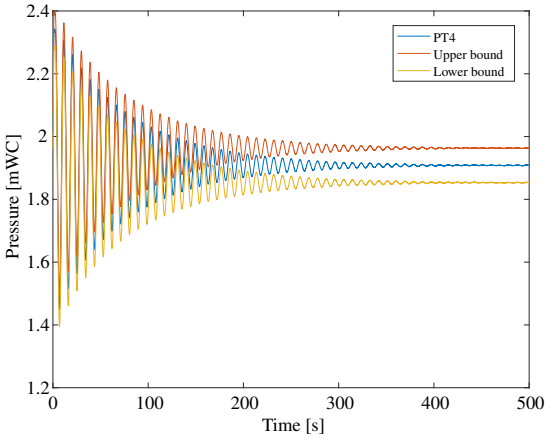

(a) PT4 measurement with error bounds.

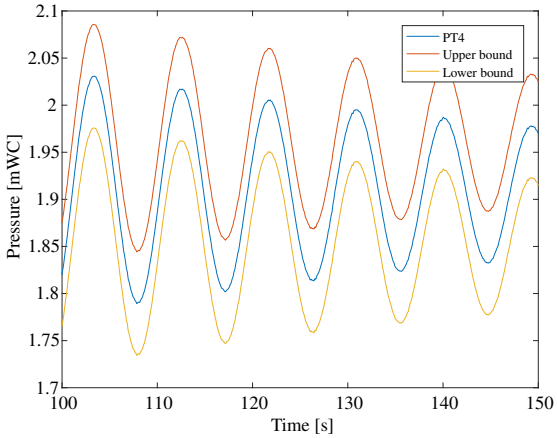

(b) Closer view of PT4 measurement with error bounds.

Figure 13: PT4 with error bounds.

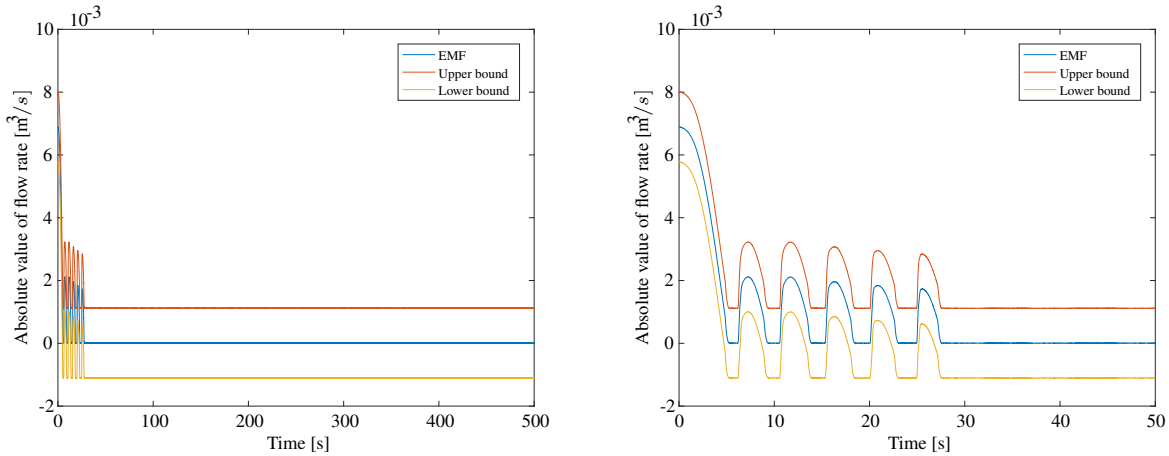

(a) EMF measurement with error bounds.

(b) Closer view of EMF measurement with error bounds.

Figure 14: EMF with error bounds.

The pressure transducers have a very wide measuring range, compared to the values of the pressures that are measured in the experiments. The UNIK 5000 transducers have a range from 0 to 5 bar gauge, while the highest pressures that are measured in the experiments are around 0.245 bar, or 2.5 mWC. This means that the maximum measuring error in the instrument will be quite a large percentage of the measured value [34, Chapter 2]. In order to reduce the systematic error, a transducer with good accuracy and a smaller measuring range could be chosen.

The accuracies stated by the manufacturers are often the best estimate they can give for the instrument when it is new and used according to the specifications [34, Chapter 3]. The uncertainties for older instruments like the ones used in this experiment, could therefore be even higher.

6.1.4 Pressure measurements

In Figure 15 the measurements from all four pressure transducers are plotted together. The figure shows the pressure oscillations after valve closure, but includes measurements of the steady state flow immediately before the valve is closed. In this plot, the valve is closed when the time is approximately 150 s. The measurements from PT3 and PT4 are quite similar in shape, but since they are located at different heights on the rig, the pressures are offset with a difference equal to the height difference. PT4 is placed approximately 0.12 m above PT3. This matches well with the measured difference between the steady states that are reached after valve closure. PT4 reaches 1.906 mWC, and PT3 approaches 2.023 mWC. As shown in Figure 5 in section 5.1, PT4 is located in the surge shaft, and PT3 is located very near to the surge shaft, in the horizontal pipe. Thus, the pressure measurements from the two transducers are very similar. The PT2 is located in the horizontal pipe between the reservoir and the surge shaft. The oscillations measured by the PT2 is much smaller than those measured by PT3 and PT4. This could be because the transducer is placed too far away from the surge shaft. The PT1 is located in the water tank, approximately 11 cm above the bottom of the tank. The horizontal pipe is located approximately 45 cm above the bottom of the tank. This matches well with the measured

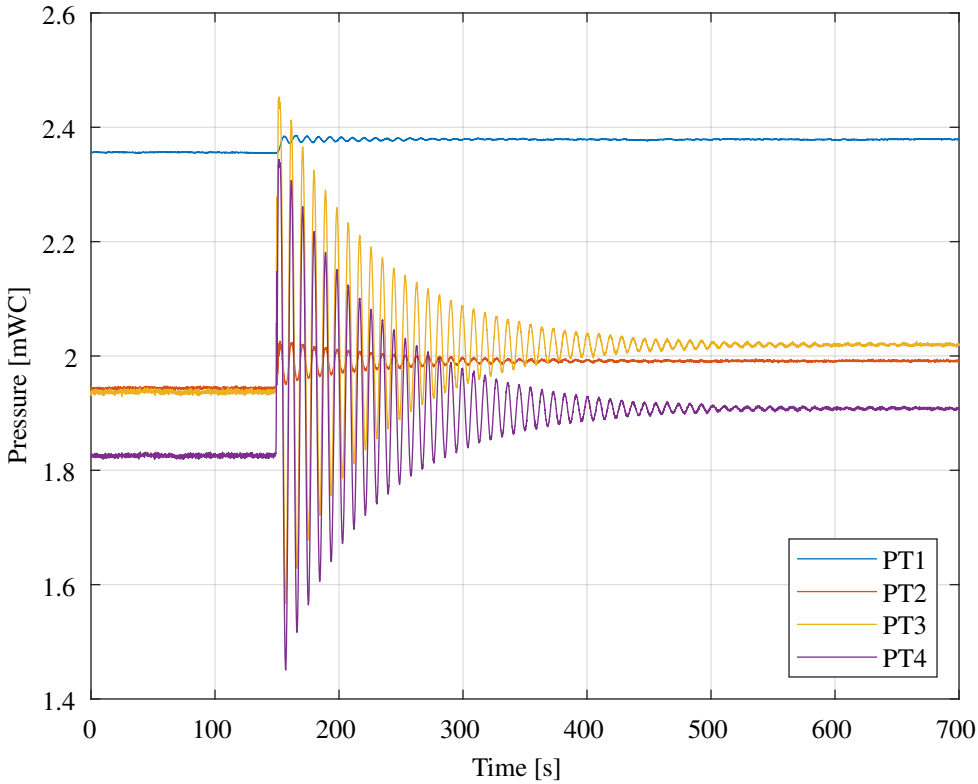

Figure 15: Pressure measurements from the four pressure transducers. Flow at steady state with $Q = 0.007$ m^3/s for the first 150 s, followed by a valve closure.

difference in pressures between the PT1 and the PT2 when the valve is closed. One can also notice that the pressure measured by PT1 also increases slightly when the valve is closed. This will be discussed more in detail later.

The time period for the oscillations is found from the plots to be approximately 9.2 s. This corresponds well with the theoretical formula from liquid column theory, equation 20, which yields $T = 9.18$ s for a water column of length 21 m.

6.1.5 Flow rate measurements

The average of the measurements of the flow rates for the case of initial flow rate equal to 0.007 m^3/s, is shown in Figure 16. The flowmeter is located approximately 4.5 m downstream of the water tank. One may note that the EMF measures the flow to be zero after approximately 30 s. While the pressure fluctuations measured by the PT2 lasts for about 200 s. The PT2 is located upstream of the flowmeter. The pressure oscillations measured at the PT2 suggest that there are also changes in the flow past the flowmeter beyond the first 30 s. The changes could be too small for the flowmeter to pick up on. The full-scale flow of this particular meter is 0.5556 m^3/s [25], which is much higher than the highest flow rate in these experiments. So due to the already low initial flow rates, the oscillations in the flow rate beyond the first 30 s could be too small. The flow profile will most likely be slightly distorted during the transient.

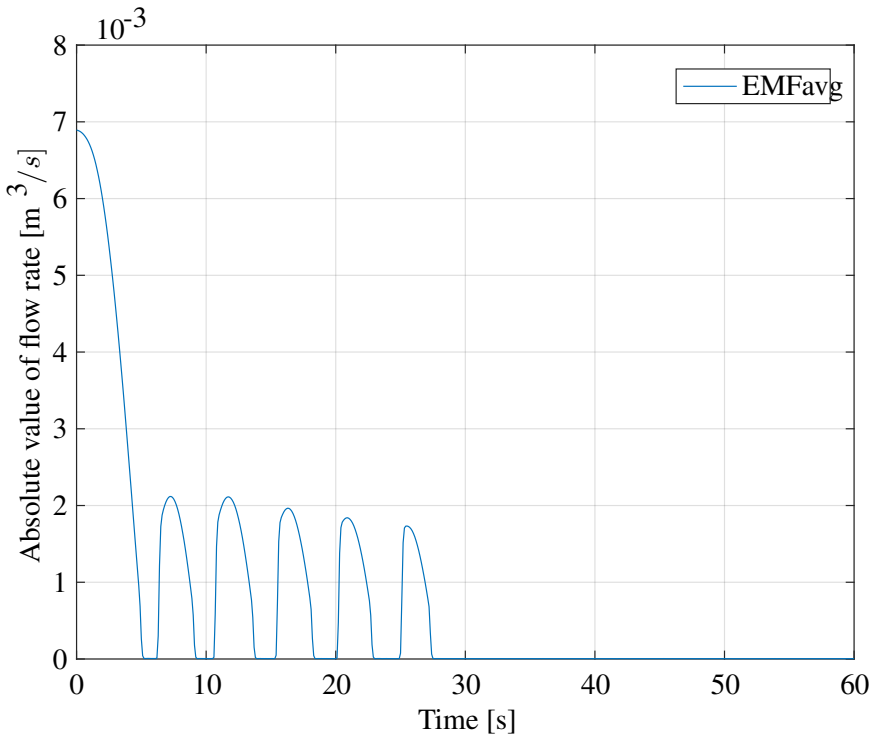

Figure 16: EMF measurements

Other researchers have reported asymmetry of the velocity profile during water hammers [49], and some of the same phenomena are thought likely to occur during mass oscillations. This could also impact the flow rate measurements, although the manufacturer of the flowmeter states that the measuring accuracy of EMFs is only minimally affected by asymmetrically distorted flow profiles [35].

EMFs work, as mentioned, only for electrically conductive fluids. The water in these experiments is not distilled and contains sufficient ions so low conductivity is not a problem. Another requirement for the EMF is that the pipe is full. It does not work for partially full pipes. The pipe was full, however some air bubbles were present. A few bubbles were seen through the Plexiglas section of the pipe. But the bubbles were not so big and not numerous, so they were not thought to affect the measurements greatly.

The electromagnetic flowmeter that was used, is able to measure direction. But with the logging program in LabVIEW, the direction was not recorded. The display on the flowmeter, however, shows the sign of the flow. By manually inspecting the display, it was seen that after the transient had been initiated, the flow rate changed sign several times before it became 0. Thus, the value shown in Figure 16 is considered an absolute value of the flow rate. It seems likely that, if the direction had been logged as well, the flow rate would be negative for every other peak seen in Figure 16.

The main objective of the flow measurements with this flowmeter is to find the initial flow rate before the transient is initiated. In order to study the flow during the transient, measurements with for example PIV should be done as suggested earlier.

6.1.6 Water hammer

A closer look at the beginning of the oscillations show a peak approximately 0.5 s after the valve was closed, as seen in Figure 17. In the figure the valve was closed when t=9.2 s. This peak is due to the water hammer.

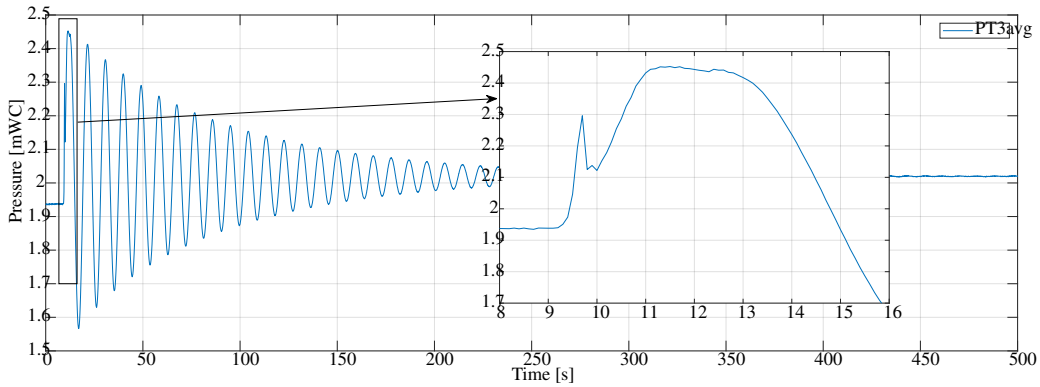

Figure 17: Pressure measurements from PT3 with a zoomed view of the water hammer.

Going back to the experimental results for each valve closure, it can be seen that the difference between the measurement results is larger right after valve closure, when the water hammer is present, than after a little while, when the mass oscillations dominate. The water hammer in each of the five closures is plotted in Figure 18a. The pressure peak is clearly highest for the first valve closure. The time of the highest occurring peak is also different for the different closures. The logging frequency was the same for all cases. In Figure 18a, the raw data has been averaged for every 20th measuring point, as described in section 6.1.2. While in Figure 18b, the raw data is plotted.

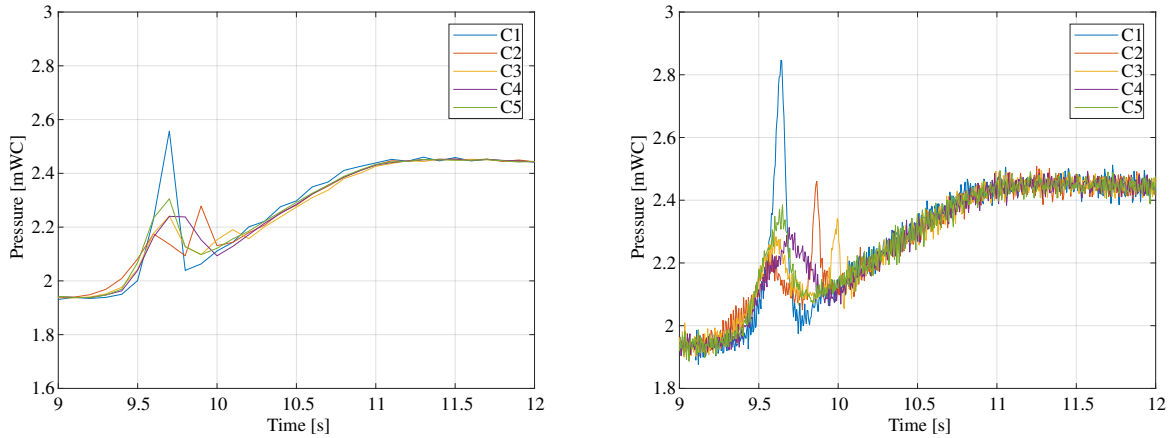

(a) Averaged measurements.

(b) Raw data.

Figure 18: Water hammer.

The differences in the water hammer peaks, can be due to the closure of the valve. The valve was closed manually. The time it took to close the valve would therefore have varied slightly for each closure. The time of closure was not

recorded in any way, other than counting very roughly. From this it seemed that around 2 s were used for the closures, but some may have been quicker.

The differences could also be due to reflections of the water hammer. The pressure wave is reflected at the free surfaces in the test rig, and at the valve. So a complicated pressure pattern could occur, and pressure waves could meet and increase or cancel each other out.

The time periods for the water hammer and mass oscillations are very different. The water hammer is damped out before the mass oscillations really begins, as can be seen in for example Figure 17. The two phenomena can therefore be analyzed separately [10, Chapter 4]. The remainder of this thesis focuses on the mass oscillations, and the first part containing the water hammer is ignored.

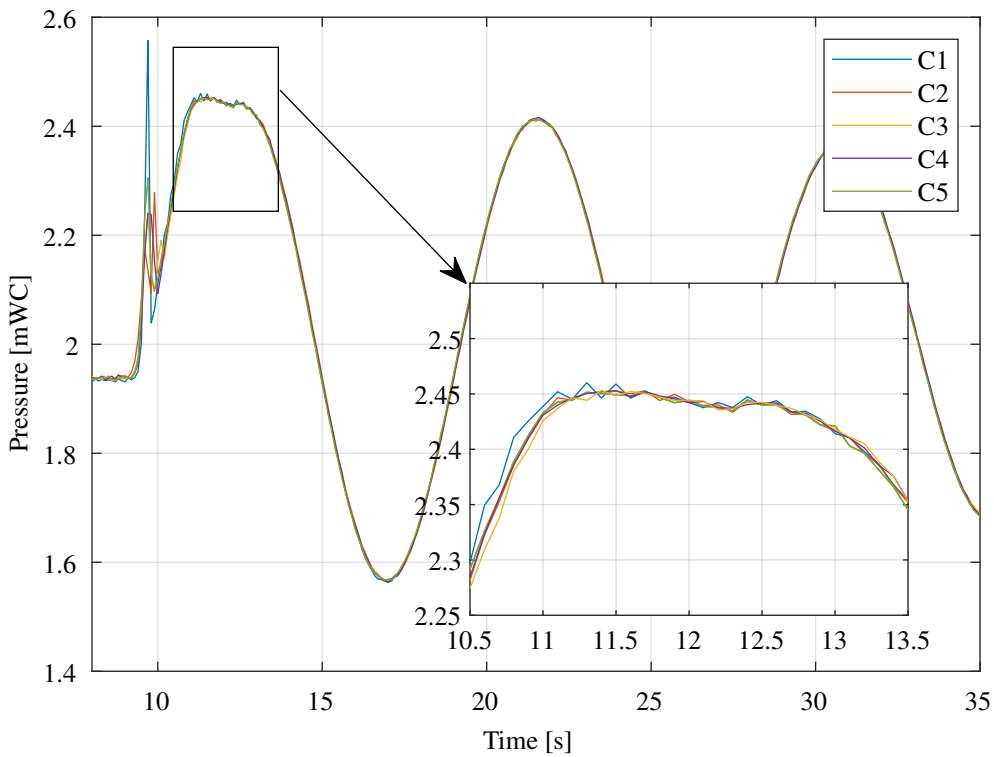

Figure 19: The first pressure peak.

The first pressure peak following the water hammer can be viewed more closely in Figure 19. Compared to the following peaks, this peak is flatter at the top than the other peaks. It also has a slight dip in pressure at the top. Why this happens, is not fully understood. But the measurements done for the cases with lower initial flow rates than presented here, does not have this flat first peak. Nor do they have such a prominent water hammer as the measurements for $Q_{\text{initial}} = 0.007$ m^3/s. Because of this, the first pressure peak was ignored when the measurements were compared to the simulations.

6.1.7 Level in the reservoir

A fourth pressure transducer was installed approximately 10 cm from the bottom of the reservoir tank. The purpose of this pressure transducer, PT1, was to monitor the level in the reservoir. The spillway in the reservoir tank has previously been designed by Bergset [25] in such a way that excess water is removed, with the hope that the level in the tank stays constant also during transients.

Level measurements with pressure transducers are quite accurate compared to many other level measurement systems [34, Chapter 17]. Inaccuracies can arise from the density that is used when calculating the level from the equation for the hydrostatic pressure. Ideally temperature measurements should be done, to find a better estimate of the density, when very accurate level measurements are needed. For example, during steady flow through the pipe, the level in the reservoir is measured to be 0.231 bar. In this experiment, the temperature of the water was assumed to be 15° C. This corresponds to a density of 999.1 kg/m^3 [6, Appendix 1]. The gravitational acceleration at the test location has been measured by NGU to be 9.82 m/s^2. With this, the level during steady state flow in the test rig, is 2.355 m. If instead the temperature was assumed to be 20° C, the density would be 999.7 kg/m^3, and the level would be 2.353 m. Similarly, if the water temperature was assumed to be 10° C, the density would be 998.0 kg/m^3, and the water level would be 2.357. The inaccuracy related to the density, also concerns the other pressure measurements in the experiment. However, these differences in water level amounts to differences in water level of just a few millimeters, so the choice of density is not considered to have a significant impact on the results. If a greater level of accuracy were required, temperature measurements of the water should be done.

The results from this pressure transducer show that the level changes slightly during transients. After the valve is closed, the water level increases by approximately 0.03 m as seen in Figure 20. Following this increase, the level in the tank oscillates slightly with the same frequency as the oscillations measured by the other pressure transducers in the pipe and surge shaft. However, the peaks in reservoir level occurs at a later time than the pressure peaks measured by the other transducers. This can be seen in Figure 21 and Figure 22. The reason for this shift could be the inertia of the water in the tank, or the level measurement could also be affected by swirls and movements in the water.

Since the variations in the level are so small, they are not thought to affect the results in any major way. And in the simulations, the level in the reservoir is considered constant.

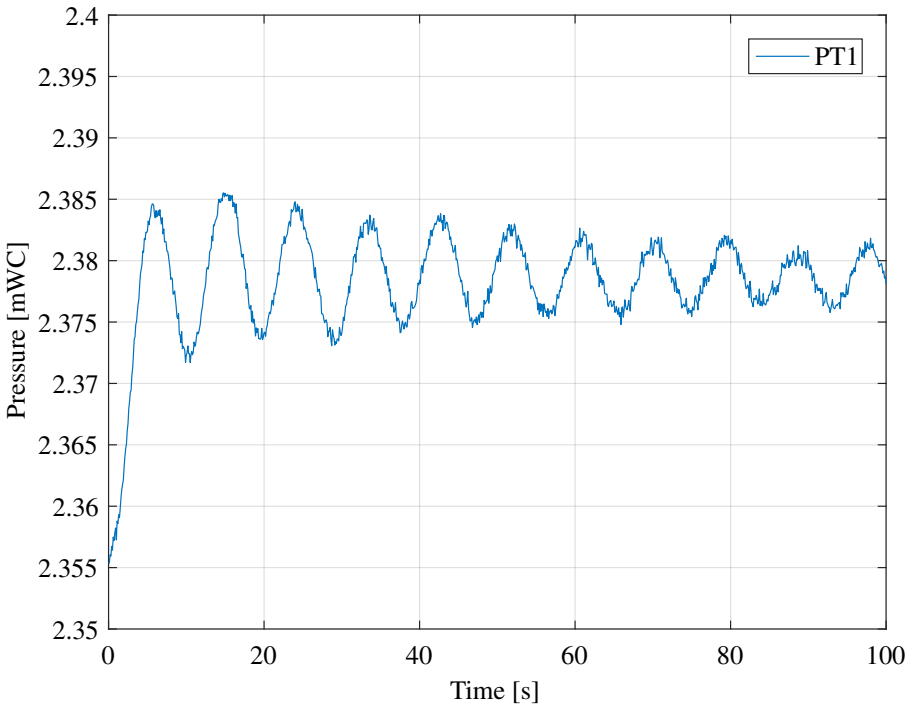

Figure 20: Pressure measurements from the transducer at the bottom of the reservoir.

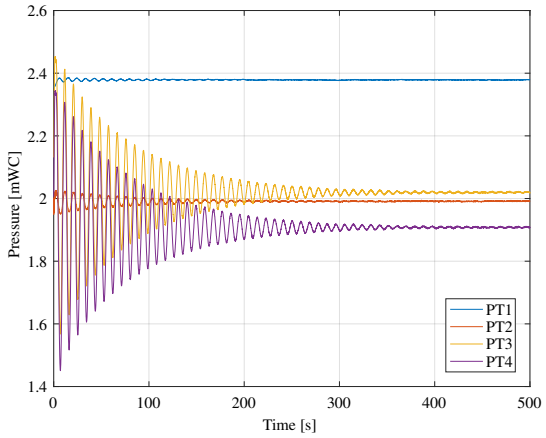

Figure 21: Pressure measurement from all the pressure transducers.

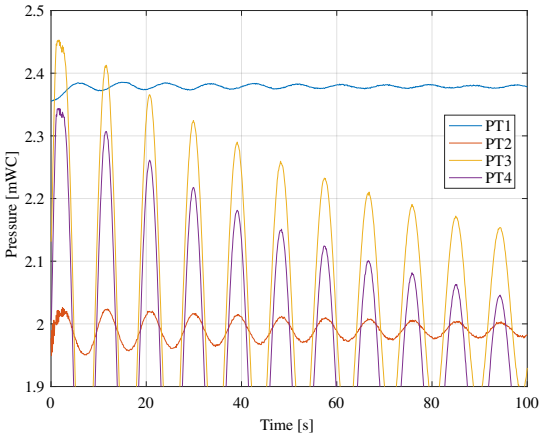

Figure 22: Zoomed in view of all the pressure measurements.

6.1.8 Minor losses

In the rig, there are several components which cause minor losses. There will be minor loss at the entrance to the pipe, at the valves, and at the junction of the surge shaft and the horizontal pipe. Summation of the general minor loss coefficients from Table 1, yield a total minor loss coefficient of $K_L = 1.08$. Of the four valves in the rig, only the first valve, upstream of the PT3 and PT4 is taken into account. There were no exact loss coefficients from the

manufacturers available for the different components in the rig, so this value is just an approximation and should be used as a guideline only. There are also 12 flanges in the rig which may cause additional minor loss. No minor loss coefficients were found for flanges, so this was not included in the calculation of the total minor loss coefficient. A study of the head loss during steady state operation of the rig, lead to the conclusion that the minor loss coefficient in the rig might in reality be quite a lot higher than 1.08.

A value of around $K_L = 3.5$ seems to fit better with the steady state losses. The friction loss was in this case found with the Darcy-Weisbach equation, and the Darcy friction factor was found from equation 23 and 24 with the roughness coefficient for the pipe equal to 0.002 mm. There is also some uncertainties connected to the roughness coefficient of the pipe. The value for the average roughness was found from Table 6.1 in [7, Chapter 6], which states recommended average roughness values for different commercial materials. The roughness for the stainless steel pipe in this experiment could therefore differ slightly from this value. Also, the small part of the pipe which is made of Plexiglas, a type of thermoplastic, will have a slightly different roughness coefficient than the steel pipe. Table 6.1 in [7, Chapter 6] states that the roughness coefficient for plastic is 0.0015 mm with an uncertainty of $\pm 60\%$. Since this value does not differ greatly from that of the steel pipe, and the length of the Plexiglas section is short, the Plexiglas section was ignored, and instead considered to have the same roughness as the steel pipe.

So there are uncertainties related to the minor loss coefficient, and the roughness coefficient. Nevertheless, the minor loss coefficient found from the steady state loss was chosen for further use in the simulations rather than the value from general tables.

6.2 Simulations

6.2.1 Method of Characteristics

A MATLAB code which calculates the head and flow rate along the test rig with the method of characteristics was developed. Some simplifications which were done in the code is discussed below, and then results from the simulations are presented by comparing the calculated head in the surge shaft to the measured pressure head from the experiments.

The minor loss should be spread across the pipe at the positions where the components causing the minor loss are placed, but as a simplification in the code, all the minor losses were lumped together at the beginning of the pipe and considered an entrance loss. Since the focus in this case is on the change in head at the surge shaft, this simplification is not considered to have a significant impact on the results compared with if the minor losses had been spread along the pipe at their respective places, since the minor losses in the rig mostly occurs upstream of the surge shaft.

In MOC, an expression for the valve closure must be given. A linear expression was tried, as well as the exponential expression stated in [26, Chapter 3]. The difference in the results obtained with the two expressions was negligible when the time before the valve was closed, t_c, was the same. The expression from [26] was used for further investigations. Since no exact measurements of the time of closure was done, the rough estimate of around 2 s was used. The expression for τ with $t_c = 2$ s is shown in Figure 23. When a t_c larger or smaller than 2 s was chosen, the time of

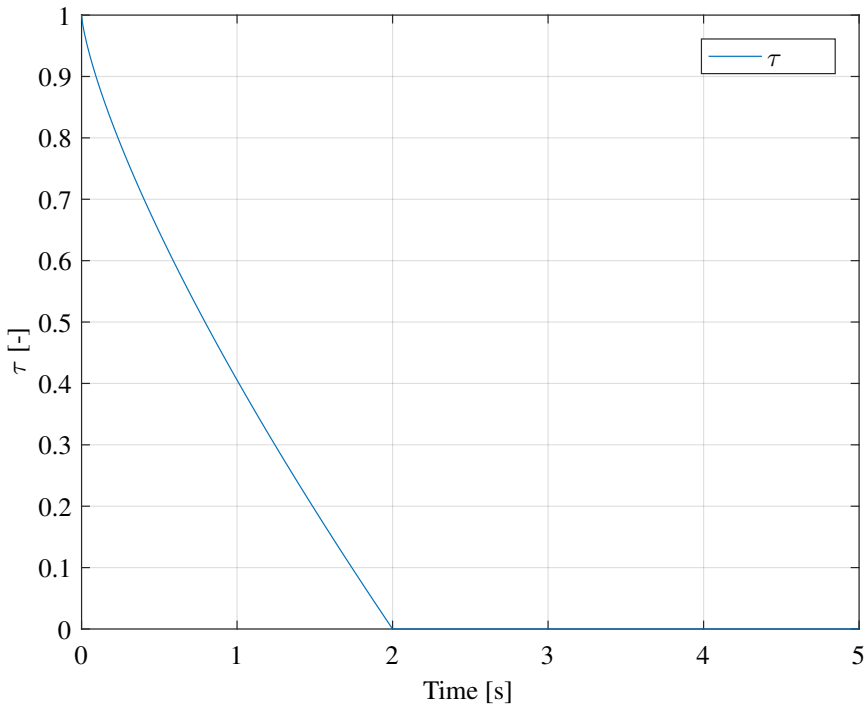

Figure 23: Dimensionless valve opening, τ.

occurrence of the extrema in the simulations did not match the measurements. When t_c was taken as 1 s, rather than 2 s, the peaks occured at an earlier time than in the measurements. Conversely, when t_c was taken as 3 s, the peaks in the simulations occured at a later time than the peaks in the measurements. So this confirms that a t_c around 2 s is a good estimate for the closing time in the experiments.

The speed of sound, a, is often somewhere between 1200 m/s and 600 m/s [9, Chapter 13]. Since some water bubbles were observed in the pipe during the experiments, the speed of sound in the MOC code was chosen to be $a = 900$ m/s. The presence of small quantities of air in the water will reduce the bulk modulus of elasticity and thus, the speed of sound [10, Chapter 4]. The speed of sound affects the pipeline characteristic impedance, the B in equation 9. And it is also related to the time step in the method. When dx is chosen and held constant, the time step will increase with decreasing a, as seen from equation 8.

The length of the pipe was divided into $N = 140$ sections, yielding $dx = 0.15$ m. This was considered adequate for the accuracy desired in the simulations, while still keeping the computations from taking too long time.

A double grid was used in the simulations as described in section 3.3.1. This means that essentially everything is calculated twice. Thus, use of a diamond grid would probably have been preferable since this would have reduced the computational time of the simulations.

Results for the simulations of the head in the surge shaft are shown in Figure 24 and Figure 25. The simulation results are compared with the measurements from the PT3, because this is placed in the middle of the horizontal pipe at

the location of the surge shaft. In the simulations in Figure 24 and Figure 25 the friction was found from the quasi-steady model. Figure 24 shows the simulations from the beginning of the transient, until the measured oscillations are completely damped out after 500 s. As seen in the figure, the simulated oscillations are not damped out at this time, but continues to oscillate. MOC with the quasi-steady model underestimates the damping of the oscillations.

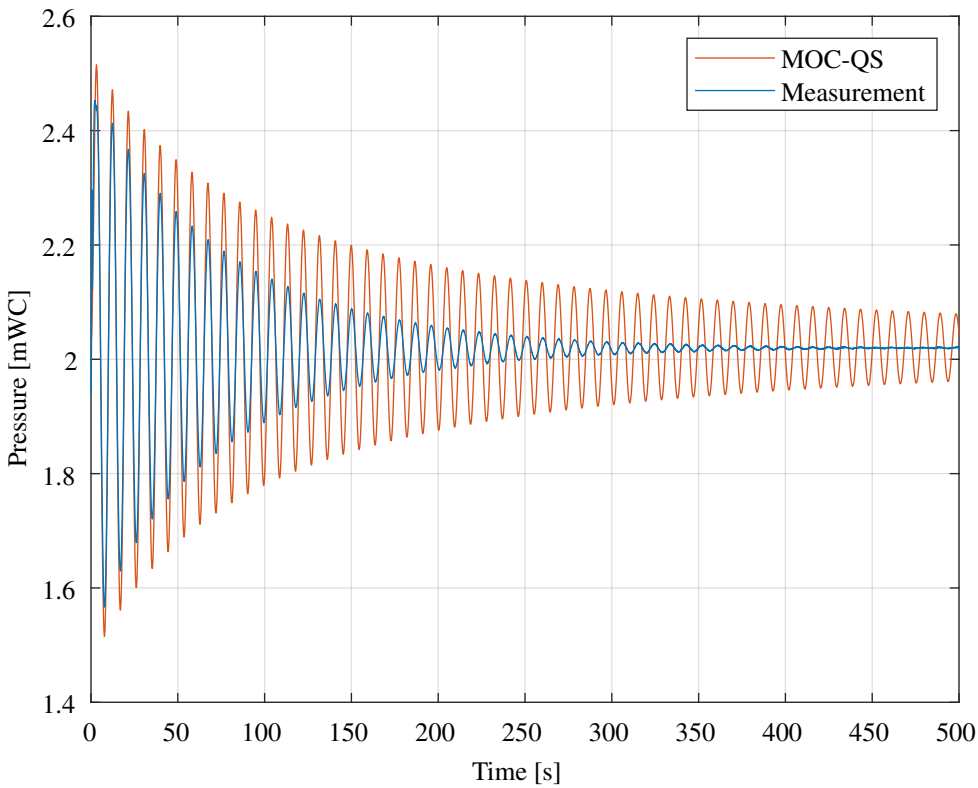

Figure 24: Simulation with MOC and the quasi-steady friction model compared with the pressure measurement.

Figure 25 is a plot of the same simulations, but shows the oscillations during the first 100 s only. From this plot, one can see more clearly that the pressure peaks are higher in the simulations than in the measurements. The difference is smaller for the first peaks, and then the difference increases.

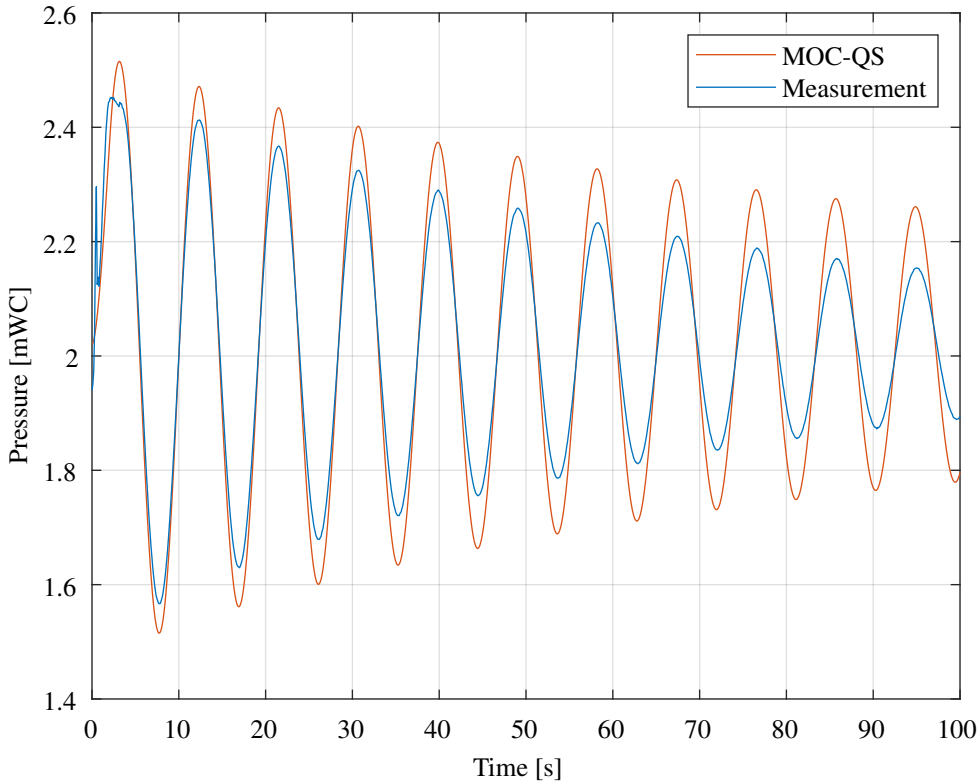

Figure 25: Simulation with MOC and the quasi-steady friction model compared with measurements for the first 100 s following the valve closure.

The relative error between the simulations and the measurements calculated at the extrema, is plotted in Figure 26. This shows more clearly that the difference is smaller at the beginning of the simulation, and then the difference between the simulation and calculation increases, before it is reduced again. The plot also shows that for the first 250 s, the difference between the simulations is larger for the local minimum points than for the local maximum points.

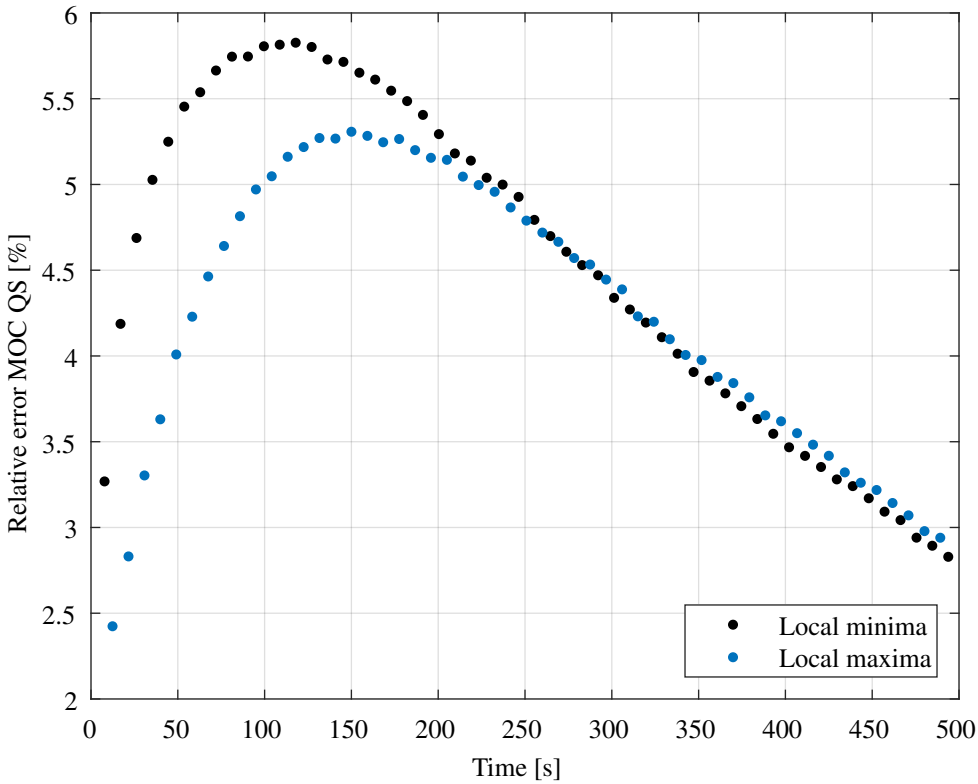

Figure 26: Relative error between the simulation and the measurement plotted at each extrema.

The one-term model was also implemented in a method of characteristics scheme. For the implementation, the time derivative of the velocity was approximated with a backward finite difference. Otherwise, the method was as described in the theory section. The B coefficient was found by using $D_1 = 0.15$ m and $D_2 = 0.325$ m in equation 28.

Results with this method are shown in Figure 27 and Figure 28. In Figure 27, the simulation time was 500 s. For the first 45 s, the model underpredicts the amplitude of the pressure peaks. And after this, the model does not yield enough damping of the peaks. As the measurement tends towards a steady pressure, the model continues to oscillate.

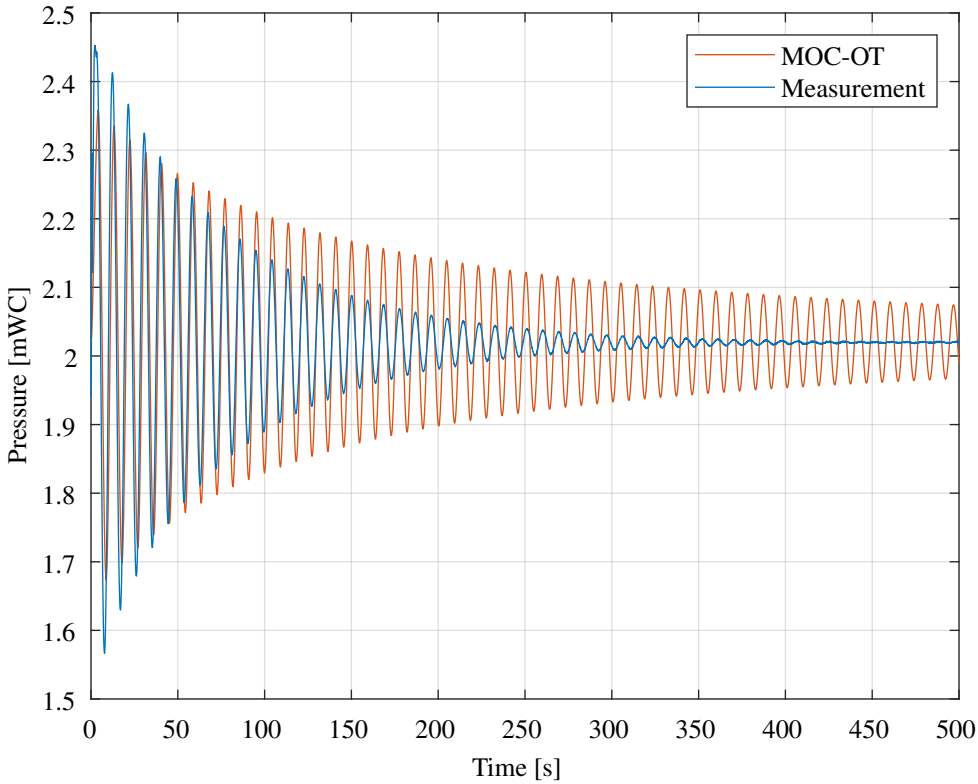

Figure 27: Simulations with MOC and the one-term friction model.

Figure 28 shows the simulation with the one-term model for the first 100 s following the valve closure. For the first five local maxima and the first four local minima, the measured pressures are larger than those predicted by the model. Generally, one prefers to have a model that predicts slightly higher pressures rather than one that predicts slightly lower pressures than actually occur, due to safety margins when designing the system. Thus, even though the absolute and relative errors are smaller for the one-term model than for the quasi-steady model, the one-term model is not preferable to the quasi-steady model in this case. In addition, Figure 28 shows that the increased damping has affected the frequency of the oscillations, so that the peaks in the simulations no longer happens at the same time as in the experiment.

Figure 29 shows the relative error at each extrema. At the time when the model shifts from underpredicting the pressure amplitudes to overpredicting them, the relative error is very small. It is 0.037% at the smallest. This occurs at the fifth local minimum. But for the rest of the extrema, the relative error is quite large. The same tendency that the relative error for the local minima is larger than the relative error for the local maxima in the first half, and then smaller, is the same for this model as for the quasi-steady model, although the difference between the relative errors is smaller.

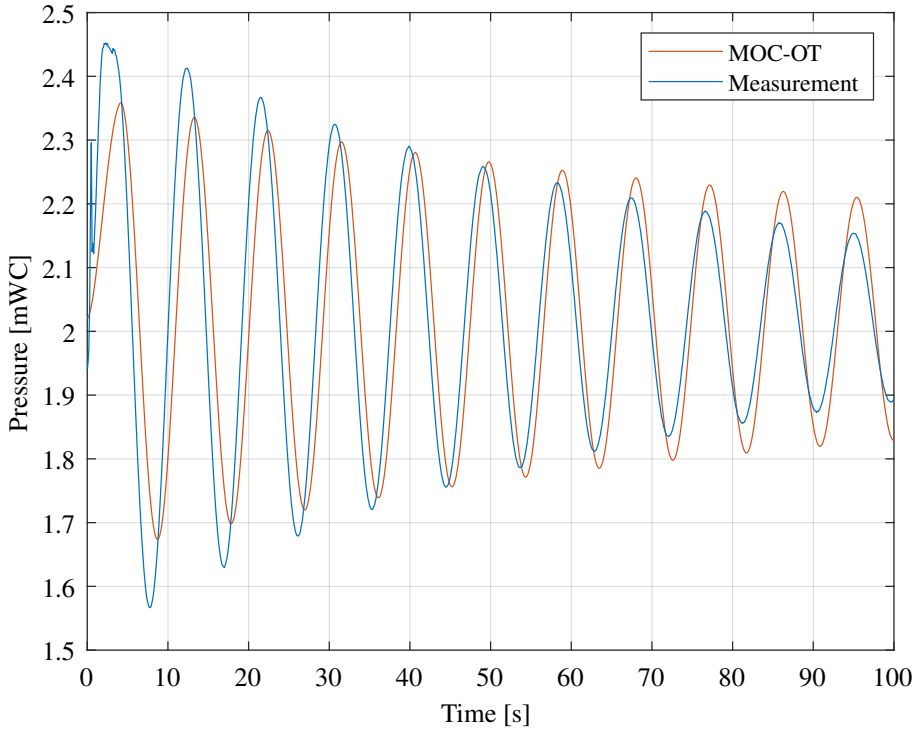

Figure 28: Simulations with MOC and the one-term friction model for the first 100 s after valve closure.

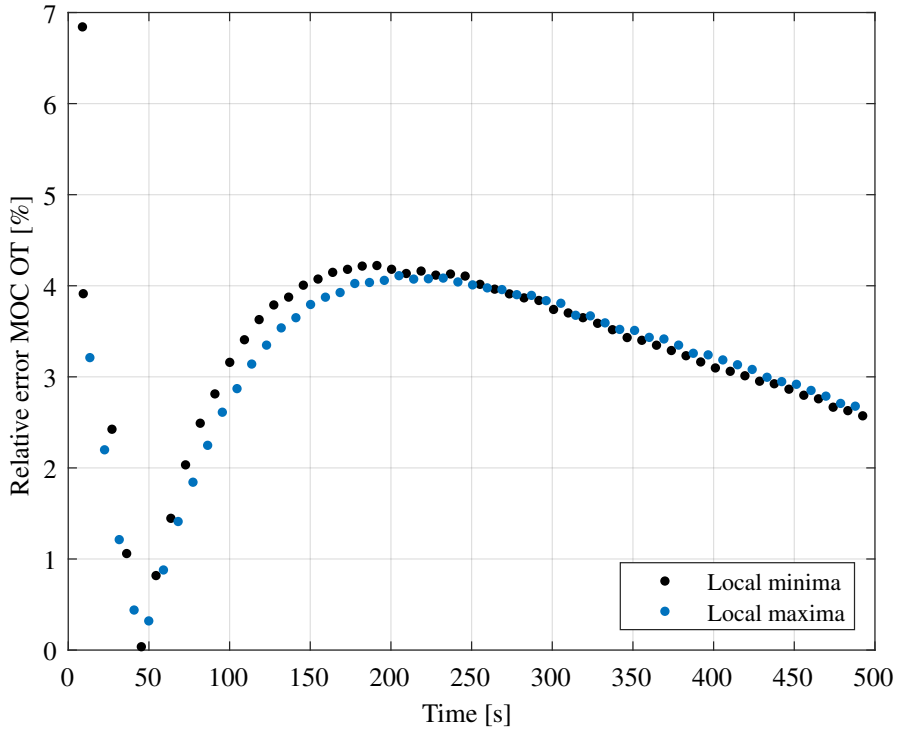

Figure 29: Relative error between the simulation with MOC and the measurements plotted at each extrema.

The plots with the other flow rates looked very similar to the ones for 0.007 m^3/s for the different models. For the other flow rates, the quasi-steady model did not yield enough damping of the oscillations, while with the one-term model, the oscillations were too damped in the beginning, and then not enough damped compared with the experiments. So in order to save space, the plots of the results obtained with the other flow rates are not shown. Instead, the errors at the extrema between the simulations and the measurements have been computed, and are presented. Table 6 contains the mean absolute error in mWC and the mean relative error in % of the simulations with MOC for the different flow rates.

Table 6: Comparison of MOC simulations with the measurements.

Model	Initial flow rate [m^3/s]	Mean absolute error [mWC]	Mean relative error [%]
Quasi-steady	0.0070	0.0882	4.39
	0.0060	0.0770	3.82
	0.0035	0.0419	2.97
One-term	0.0070	0.0655	3.26
	0.0060	0.0616	3.07
	0.0035	0.0336	2.40

Table 6 shows that for both the quasi-steady model and the one-term model, the mean absolute error is largest for the case with flow rate equal to 0.007 m^3/s, and smallest for the case with flow rate equal to 0.0035 m^3/s. The mean relative error also decreases with decreasing flow rate.

6.2.2 Rigid Liquid Column Theory

For the simulations with rigid liquid column theory, the code that was made during the project work leading up to this thesis was used.

A time step of 0.01 s was used, as this was found to solve the equations accurately enough. The maximum time for the simulations were set to 500 s.

With the quasi-steady friction model, the simulations did not yield enough damping of the oscillations, especially in the beginning and towards the end of the simulation time, as seen in Figure 30. However, this simulation is closer to the measured results than the MOC simulation with the quasi-steady friction model.

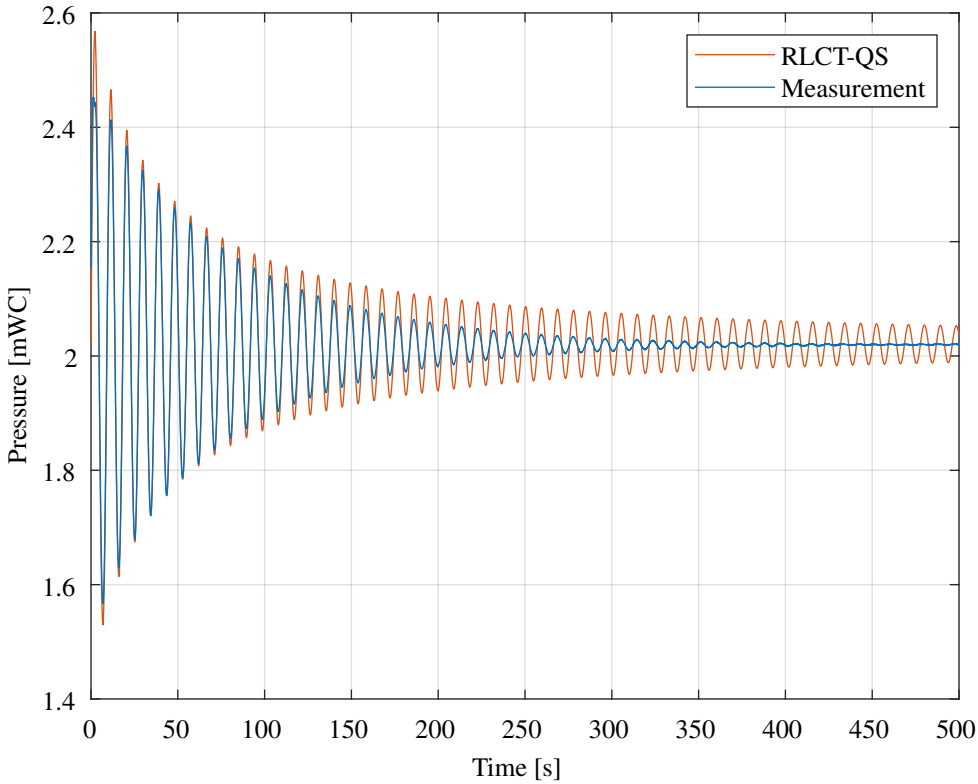

Figure 30: Simulations with RLCT and quasi-steady friction model compared with measurements.

From about 40 s to 100 s after the valve was closed, the simulations match the experiment quite well. This is seen in Figure 31.

Figure 32 shows the relative error of the local extrema. The period around 50 s after valve closure has a very low relative error since the simulations match the extrema well around this point. Compared to the relative error of the quasi-steady model in MOC, as seen in Figure 26, the relative errors for the RLCT simulation are much smaller.

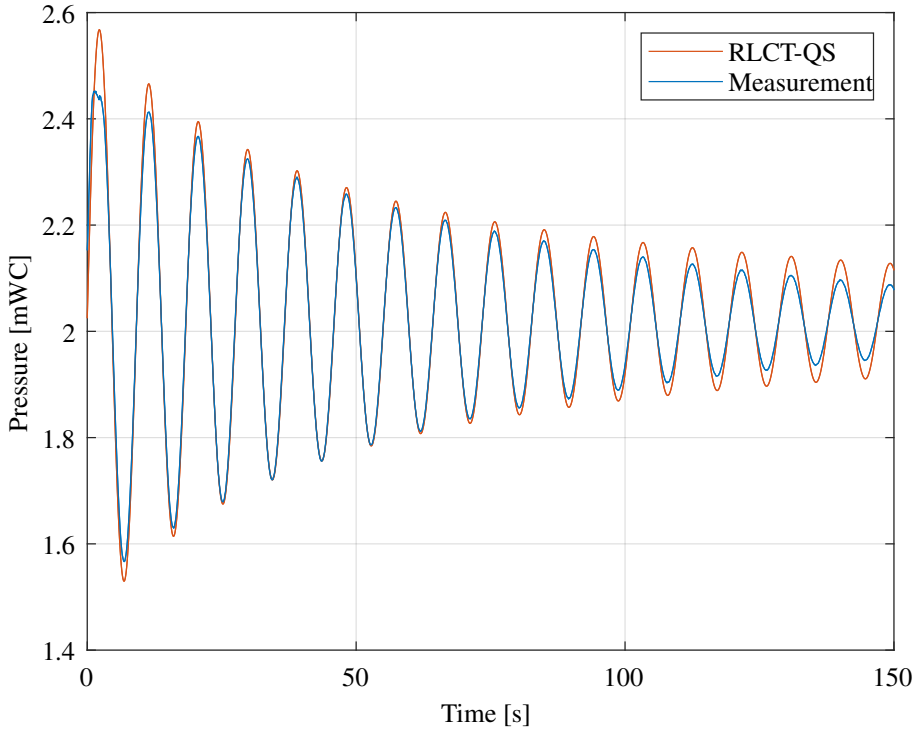

Figure 31: Simulations with RLCT and quasi-steady friction model compared with measurements for the first 150 s.

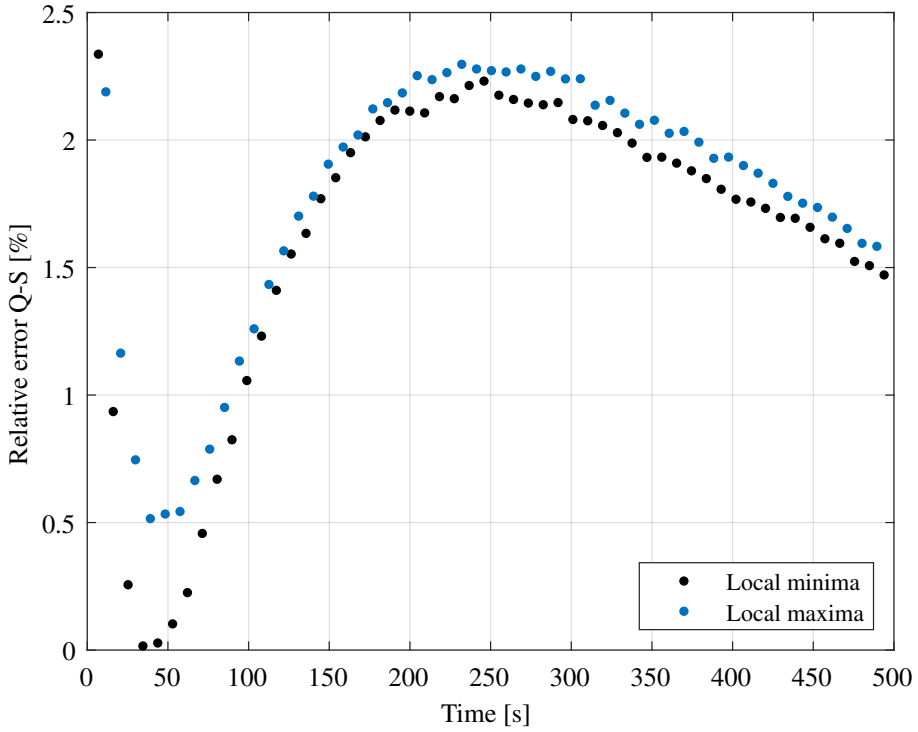

Figure 32: Relative error between the simulation with RLCT and the measurements plotted at each extrema.

Results with the one-term model in the RLCT simulations are shown in Figure 33. The simulation is plotted together with the measured result in Figure 33a, and the relative error is plotted in Figure 33b. The results with the one-term model in RLCT are quite similar to the results obtained with the quasi-steady model.

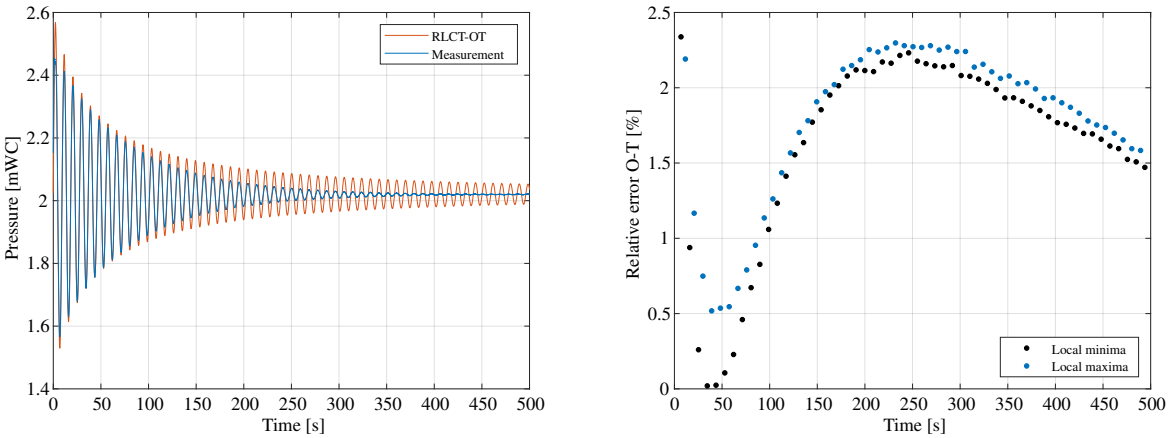

(a) Simulations compared with measurements.

(b) Relative error.

Figure 33: Results obtained with the one-term model in the RLCT simulations.

For the RLCT simulations, a third friction model, the instantaneous acceleration based Vítkovský model, was tested. This model is compared with the measurements in Figure 34a, and the relative error for this model is shown in Figure 34b. The results obtained with Vítkovský's friction model looks very similar to the results obtained with the quasi-steady friction model and the one-term friction model in RLCT. The difference is only seen in the calculations of the errors. Both the mean absolute error and the mean relative error is smaller with Vítkovský's model compared to the other two methods. The results from the calculations of the errors are shown in Table 7 for the three different flow rates.

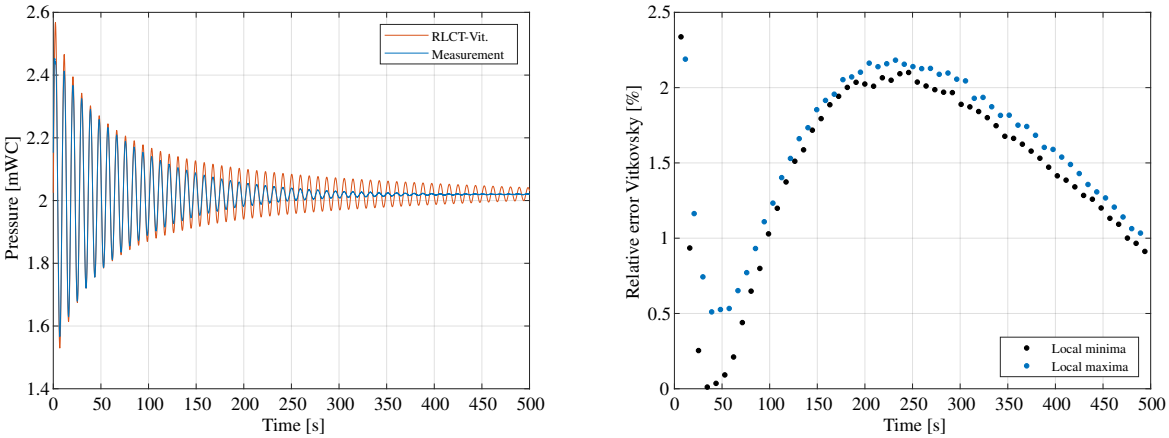

(a) Simulations compared with measurements.

(b) Relative error.

Figure 34: Results obtained with Vítkovský's model in the RLCT simulations.

Table 7: Comparison of RLCT simulations with measurements.

Model	Initial flow rate [m^3/s]	Mean absolute error [mWC]	Mean relative error [%]
Quasi-steady	0.0070	0.0344	1.70
	0.0060	0.0334	1.65
	0.0035	0.0204	1.45
One-term	0.0070	0.0345	1.70
	0.0060	0.0334	1.65
	0.0035	0.0212	1.50
Vítkovský	0.0070	0.0307	1.52
	0.0060	0.0295	1.46
	0.0035	0.0195	1.39

Table 7 shows that Vítkovský's model has the smallest errors, followed by the quasi-steady model. The one-term model has only marginally larger errors than the quasi-steady model, and this is most pronounced for the measurement with the smallest initial flow rate. Once again, for all the models, the errors decrease with decreasing flow rates. A comparison of Table 7 with Table 6 confirms that the results obtained with RLCT had smaller absolute and relative errors than the results obtained with MOC.

6.2.3 Comparison

Figure 35 shows the total head loss, the friction loss and the minor loss, during the first 100 s in the simulations with RLCT. The minor loss is larger than the friction loss for the first 50 s. After this and until the end of the simulation, the friction loss is bigger than the minor loss. This can also be seen in Figure 36 which shows a plot of the minor loss and the friction loss from 100 s to 150 s.

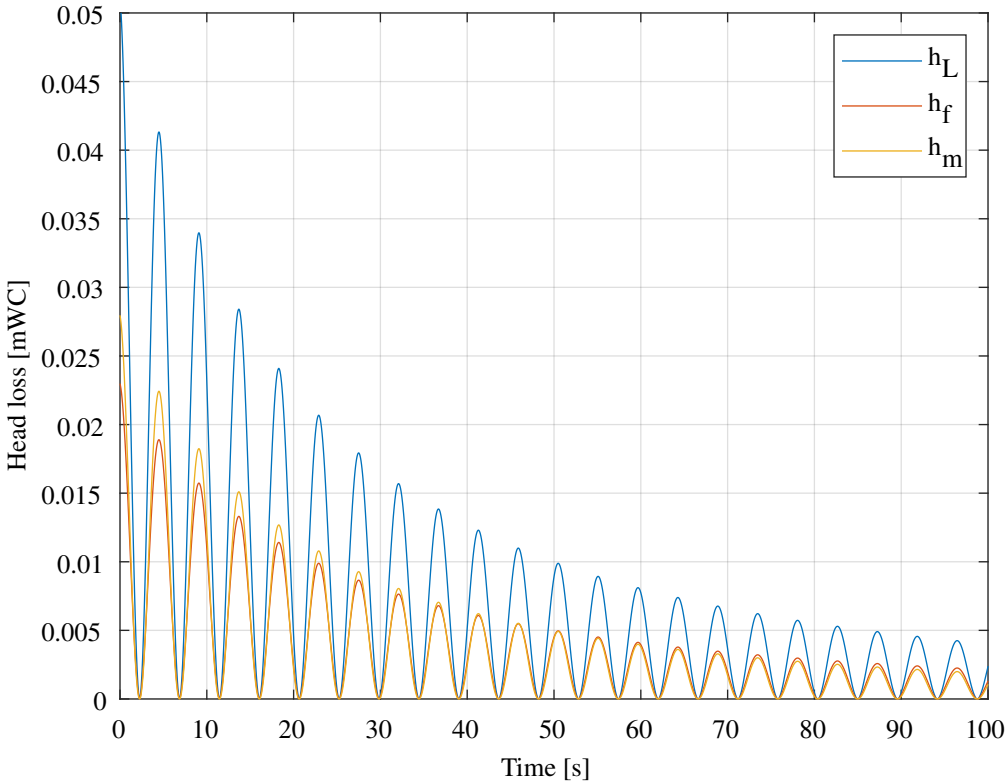

Figure 35: Total head loss, friction loss and minor loss in the quasi-steady model in RLCT simulations.

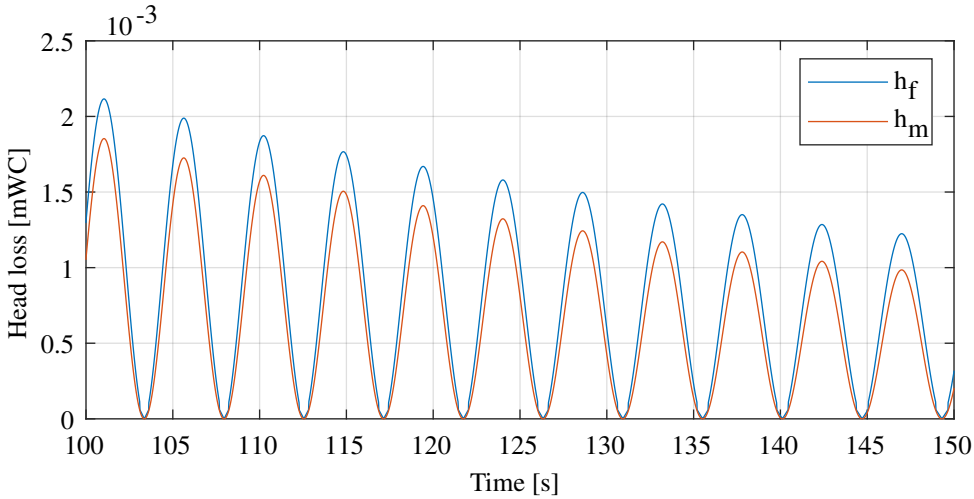

Figure 36: Friction and minor loss in the quasi-steady model in RLCT simulations.

Similar plots were made for the quasi-steady simulations with MOC. The plot containing the total head loss and the minor and friction loss, Figure 37, shows that also in the MOC simulations, the minor loss is bigger than the friction loss in the beginning. But after a while, the friction loss becomes bigger than the minor loss, as seen in Figure 38. The

total head loss is smaller than in the simulation with RLCT. For example, in the RLCT simulations, the head loss is more than 0.04 m at the time of the second peak, while in the MOC simulations, the head loss is around 0.035 m at the same peak, as seen in Figure 37.

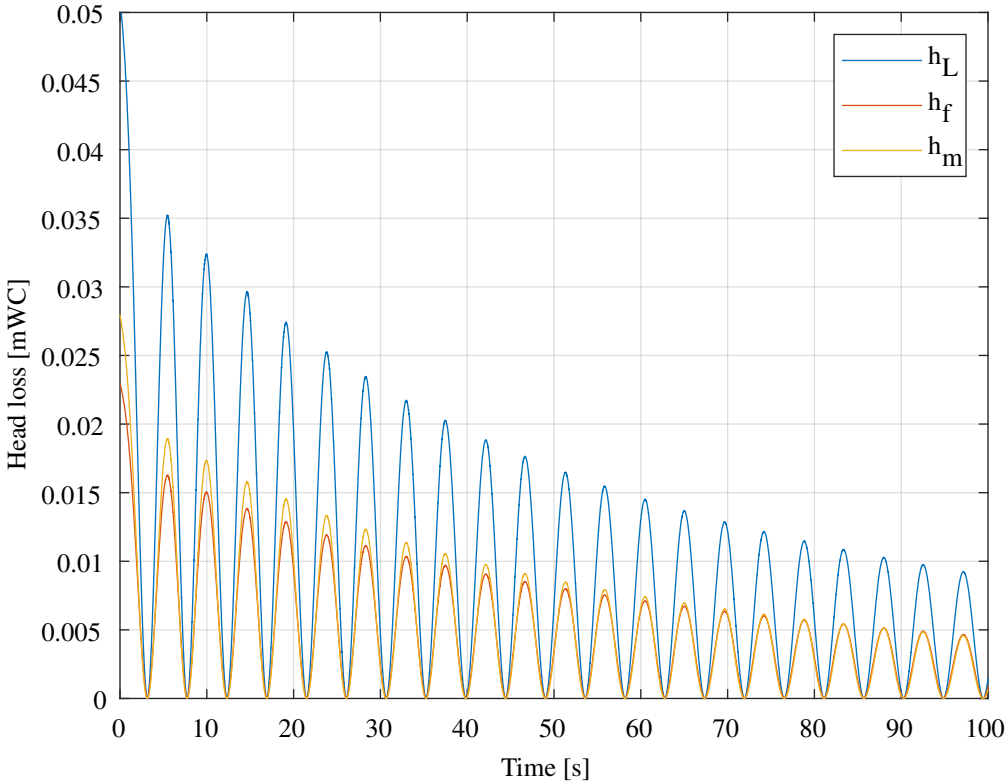

Figure 37: Total head loss, friction loss and minor loss in the quasi-steady model in MOC simulations.

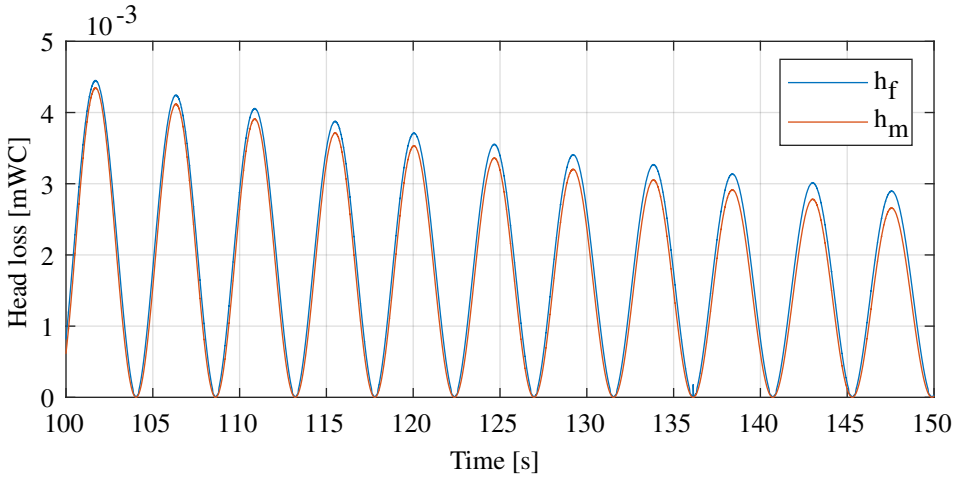

Figure 38: Friction and minor loss in the quasi-steady model in MOC simulations.

Comparing the head loss to the simulations of the flow rate, one can see that the head loss is zero when the flow rate is zero. This is because all the friction models that are tested involves multiplication with the flow rate. Thus, when the flow rate is zero in the simulations, when the flow reverses, the head loss is also zero. In reality, the velocity is not expected to be the same in the entire cross section of the pipe, so that even though the mean velocity is zero as the flow changes direction, the velocity profile is not thought to be uniform [2, Chapter 2]. The flow is expected to have a similar flow profile to the one shown in Figure 39.

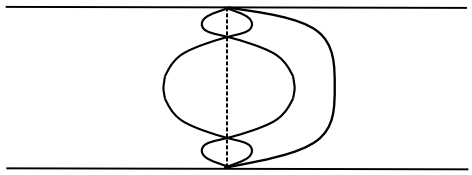

Figure 39: Flow profile when the flow turns. Based on figure in [2, Chapter 2].

This suggests that there will be a friction loss even when the mean velocity is zero. In order to take this effect into account, two dimensional models should be used. The RLCT and MOC simulations in this thesis are in one dimension. In each cross section of the pipe, there is only one value for the flow rate. Thus, variations in flow profile across one cross section is not taken into account.

The simulations with MOC and RLCT yield slightly different results, even when the same friction models are used. This could be due to the fact that different assumptions and simplifications form the basis for the two solution methods. The RLCT simulations, which are simplified the most since both the elasticity and compressibility are neglected, was found to yield the best fit with the experimental results. Even when a constant friction factor was used throughout the simulations, there were large differences between the results computed with the MOC and with RLCT. Changing the minor loss coefficient had a much bigger effect on the results with RLCT than in MOC. This could be due to the assumption that was made in the implementation of the method of charcteristics, where all minor losses were placed at the entrance to the pipe.

Another possible explanation for the difference between the two solution methods could be errors in the codes, even though the codes were thoroughly checked for errors. The MOC code was tested for steady state conditions as well, and yielded reasonable results in those cases.

Even though there were discrepancies between the two solution schemes, both solution methods were able to simulate the oscillations in the rig.

The method of characteristic is slightly more complicated to implement than the simulations with rigid liquid column theory. Use of the method of characteristics requires information about more parameters, such as the speed of sound and the duration of the valve closure. These parameters were only estimated in this thesis, and may therefore also contribute to uncertainties in the MOC simulations. Simulations using RLCT and the Euler method are easy to implement, and requires no knowledge of the speed of sound or the time of closure.

The computational times were much longer for the simulations with MOC, than for the simulations with RLCT.

When the transient equations are solved with the method of characteristics, calculations of the head and flow rate are obtained for several points along the pipe. In the simulations which used RLCT with the Euler method, one obtains just the oscillations of head in the surge shaft and an expression for the flow rate at the surge shaft. Thus, with the method of characteristics, one gets more information about the head and flow rate in the hydraulic system.

So there are advantages and disadvantages to both of the solution methods. This renders them suitable for use in different cases. When a simple model for the oscillations in the surge shaft is required, the solution with RLCT may be adequate. If more details are required, or if computations of the flow and pressure at different locations are wanted, the method of characteristics should be used.

6.2.4 Modifications

A few modifications for some of the friction models were investigated, in an attempt to find models that could yield a better fit with the experimental results.

One of the modifications that was tried for the friction models was to combine the one-term model and the quasi-steady model. The expression from the one-term model was added to the quasi-steady friction term. The resulting modification was called the modified one-term model (MOT), despite the fact that the modified model no longer consists of just one term. The results with this modified model are shown in Figure 40 and Figure 41. The relative error of the modified model is plotted together with the relative error of the original one-term model in Figure 42.

The modified version does not fit the first peak. The first peak is higher in the measurements than in the experiments, like it was for the original quasi-steady and one-term model. But the modified one-term model fits the first local minima and the second local maxima very well. After this, the oscillations in the model are more damped out than the measurements, which again is unwanted. For the peaks around 140 s, the model fits the extrema quite well. The modification improves the results towards the end of the simulations, since it provides additional damping. But the oscillations in the model are still not fully damped out at the same time as the oscillations in the measurement.

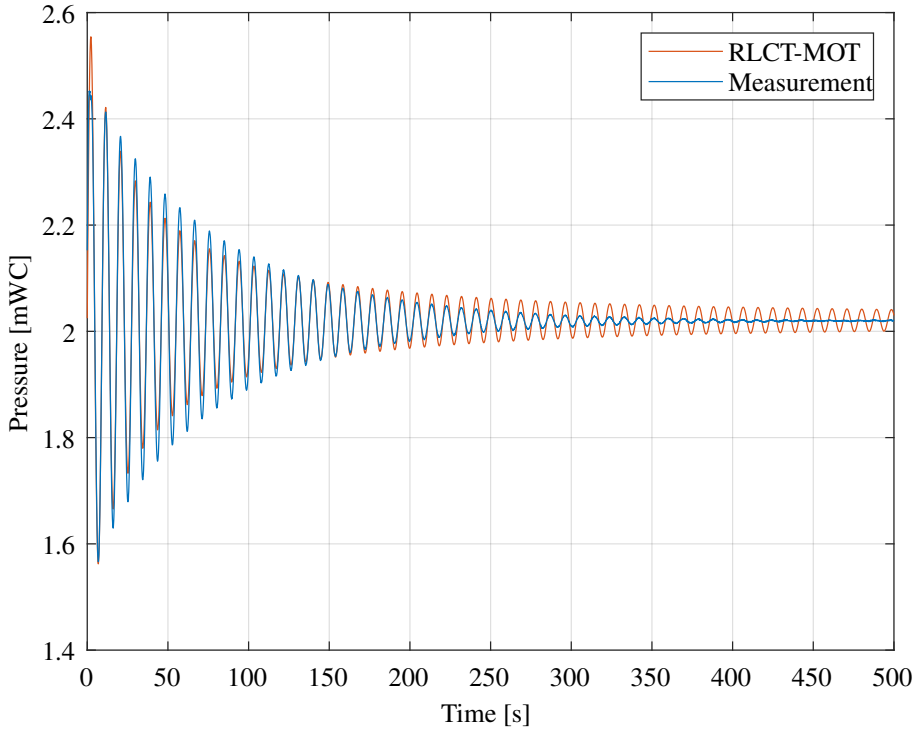

Figure 40: Simulations with modified one-term model with RLCT compared with measurements.

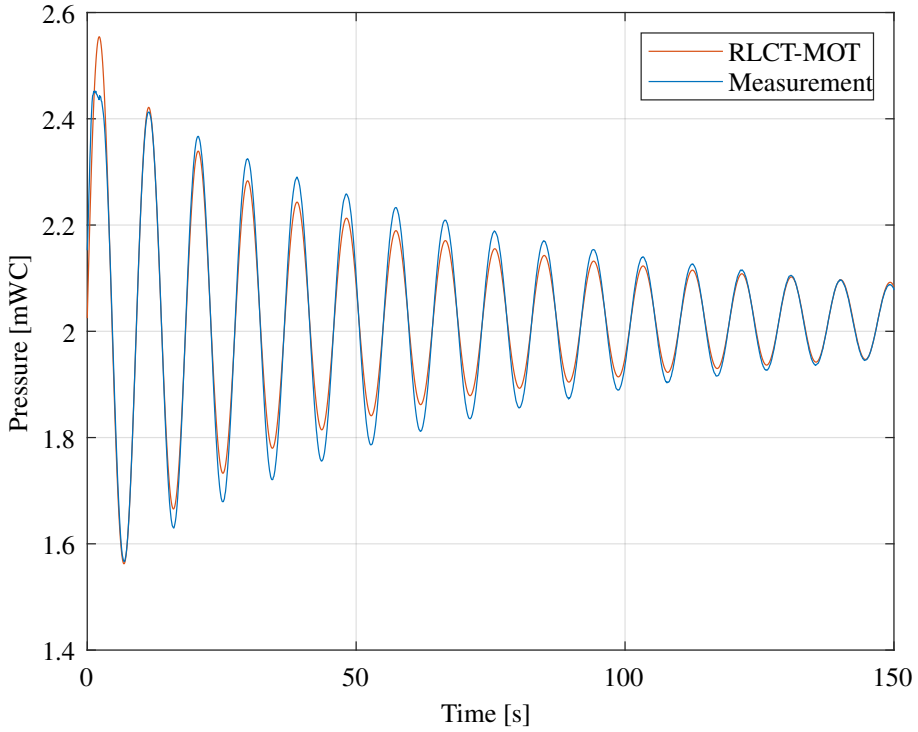

Figure 41: Simulations with modified one-term model with RLCT compared with measurements for the first 100 s.

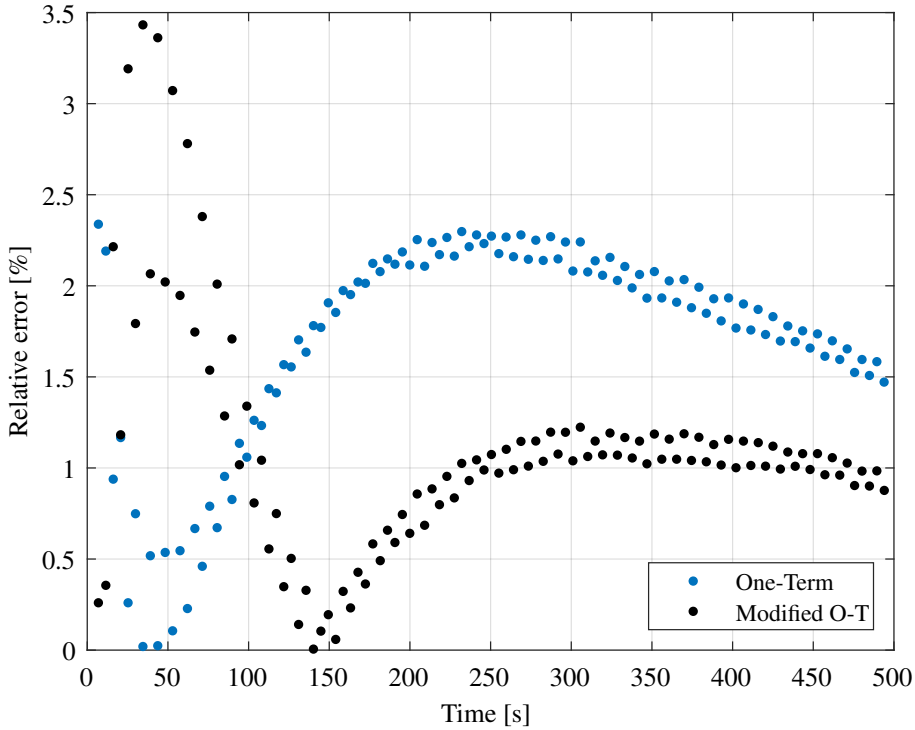

Figure 42: Relative error in the simulations with the modified one-term model compared with the relative error in the original version of the one-term model.

Table 8: Comparisons of the modified one-term model with the measurements.

Initial flow rate [m^3/s]	Mean absolute error [mWC]	Mean relative error [%]
0.007	0.0218	1.10
0.006	0.0222	1.11
0.0035	0.0129	0.92

Table 8 shows the mean absolute and mean relative errors for the modified one-term model. For all flow rates, the errors are smaller for the modified version than for the original model. The mean relative error is 0.60, 0.54 and 0.58 percentage points smaller for the modified version, for flow rates 0.007 m^3/s, 0.006 m^3/s and 0.0035 m^3/s, respectively.

Other modifications that were tested were found by dimensional analysis, in order to create a dimensionless correction term. The dimensionless correction term could then be implemented in any of the existing friction models, by multiplying it with the expression for the friction loss. One of the terms that was tested for this correction factor, CF, was

$$CF = \frac{k_1 Q/A}{(gVD)^{1/3}} \tag{31}$$

where k_1 is a dimensionless constant. For other versions of the correction factor the gravitational acceleration, g, was replaced by the time derivative of the velocity, and the diameter, D, was replaced by the length, L. None of the versions of the correction factor improved the results significantly, when implemented in any of the friction models.

The results obtained with the correction factor CF from equation 31, is nevertheless included for the initial flow rate 0.007 m^3/s. The results shown in Figure 43 and 44 are from modification of the quasi-steady friction model in the RLCT simulations, when the quasi-steady friction expression was multiplied by CF. The constant, k_1, for the results plotted here, was equal to 3.

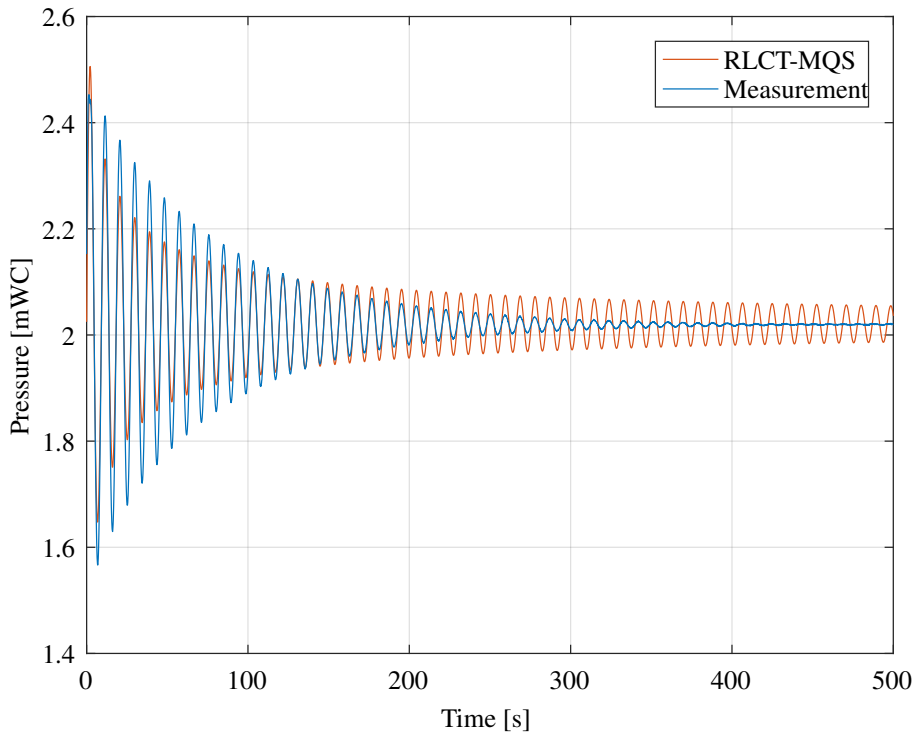

Figure 43: Simulations with modified quasi-steady model with RLCT compared with measurements.

In Figure 43 the results obtained with this modified version of the quasi-steady friction model are plotted together with the measurement result. The result is similar to that obtained with the modified one-term model, in that the model does not yield enough damping for the first peak, followed by several peaks that are too heavily damped, and as the measured oscillations are damped out, the model predicts that the pressure continues to oscillate.

Figure 44 shows the relative error at each extrema for the quasi-steady model multiplied with the CF, and for the original quasi-steady model. The relative error for the modified version is smaller than the relative error in the original version in the part of the simulation from around 100 s after valve closure to around 300 s after valve closure. Towards the end of the simulation, the relative error in the two models is quite similar. But for the beginning of the simulations, the relative error is much larger for the modified version. The mean relative error is also larger for the modified version. For the modified version the mean relative error was 1.97%, while in the original version it was 1.70% for the highest initial flow rate. The absolute error in the modified version was 0.0393 mWC, and in the original version it was 0.0344 mWC. So this modification does not improve the results.

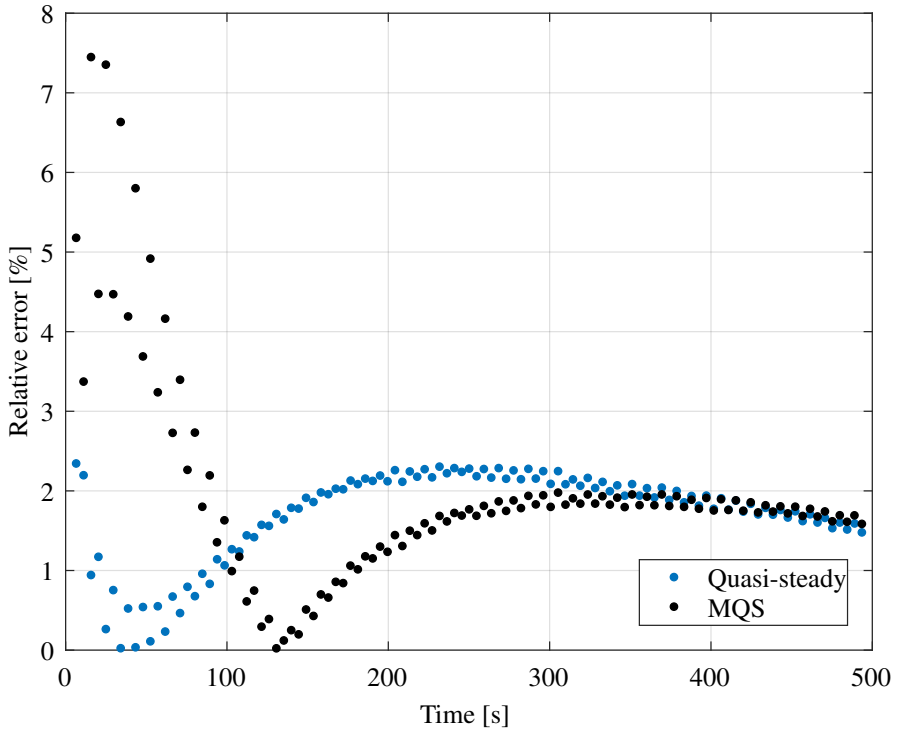

Figure 44: Relative error in the simulations with the modified quasi-steady model compared with the relative error in the original version of the quasi-steady model.

None of the friction models match the measured results completely. The modifications investigated in this thesis do not improve the results greatly. Further investigations of the friction models should therefore be done.

7 Conclusion

The friction in mass oscillations between a reservoir and a surge shaft has been investigated in this thesis. Experiments were conducted in the Waterpower Laboratory for flow with Reynolds numbers between 26 000 and 52 200. A valve was closed rapidly in order to initiate the transient flow, and the pressure and flow rate in the pipe were measured. The uncertainty in the measurements was mostly due to the systematic errors in the measuring instruments.

Simulations of flow oscillations have been performed with different models of friction and different solution schemes. The simulations were compared with the experimental results. Simulations with the method of characteristics were done with the quasi-steady model for the friction and the one-term model for the friction. The quasi-steady friction model did not give enough damping of the oscillations compared with the measurements, while the one-term model gave too much damping in the beginning of the oscillations, and not enough damping towards the end.

Simulations were also done by assuming that the water in the pipe acts as a rigid liquid column. The quasi-steady friction model and the one-term friction model was tested within this solution scheme, and gave better results than with the method of characteristics. The mean relative errors between the simulations and experiments were between 1.45% and 1.7% for the simulations using rigid liquid column theory, and between 2.4% and 4.4% when the method of characteristics was used. The differences between the results were in part attributed to the different assumptions and simplifications that are done within the two different solution methods.

Vítkovský's friction model was also tested in simulations with rigid liquid column theory, and yielded slightly better results than the quasi steady friction model and the one-term model.

A few modifications of the friction models were also tested. A model which was a combination of the quasi-steady model and the one-term model, reduced the relative error between the simulation and the experiment. However, it was still not considered a good modification, since it provided too much damping of the oscillations for parts of the simulation, and not enough towards the end.

None of the friction models yielded oscillations that were damped out at the same time as the measurements. The pressure in the simulations continue to oscillate even after the measurements have reached steady state. Further investigations of friction models should therefore be done in order to find models that can be used to accurately predict the damping of the mass oscillations in a hydraulic system.

8 Further work

A lot of interesting work still remains to increase the accuracy in models of friction during transient mass oscillations.

Further investigations of different friction models and modifications of different friction models should be done in order to find models that match the experimental results better.

More extensive measurements of mass oscillations should be done in order to understand the flow behaviour during mass oscillations better. When more detailed measurements are done, one may be able to suggest friction models that are based either on empirical observations or on physical variables. Investigations of the velocity profile should be done with PIV measurements, as suggested in this thesis. Experiments with other lengths of the rig should also be done, so that investigations of how the damping of the oscillations change for different frequencies can be done.

In this thesis, oscillations were induced by closing a valve in the hydraulic system. But oscillations occur also after valve opening, so experiments and simulations of damping of the oscillations after a valve has been opened could also be studied.

It would also be interesting to see how the results obtained from the measurements in the small-scale test rig differ from results for a full-scale hydropower plant. Therefore, measurements of oscillations in a full-scale hydropower plant could also be done.

Bibliography

[1] International Energy Agency. Renewables 2018 Analysis and forecasts to 2023, executive summary. `https://webstore.iea.org/download/summary/2312?fileName=English-Renewables-2018-ES.pdf`, 2018, Accessed 10.10.2018.

[2] T.K. Nielsen. Dynamisk dimensjonering av vannkraftverk, 1990.

[3] M.H. Chaudhry. *Applied Hydraulic Transients*. Springer, 3rd edition, 2014.

[4] M.S. Ghidaoui, M. Zhao, D.A. McInnis, and D.H. Axworthy. A review of water hammer theory and practice. *Applied Mechanics Reviews*, 58:49–75, 2005.

[5] F.M. White. *Viscous Fluid Flow*. McGraw-Hill, 3rd edition, 2006.

[6] Y.A. Çengel and J.M. Cimbala. *Fluid Mechanics: Fundamentals and applications*. McGraw-Hill, 2006.

[7] F.M. White. *Fluid Mechanics*. McGraw-Hill, 7th edition, 2009.

[8] J.P. Tullis. *Hydraulics of Pipelines: Pumps, Valves, Cavitation, Transients*. John Wiley & Sons, 1989.

[9] D.D. Ratnayaka, M.J. Brandt, and K.M. Johnson. *Water Supply*. Butterworth-Heinemann, 2009.

[10] O. Guttormsen. *Vassdragsteknikk II*. Akademika, 2016.

[11] R.W. Powell. History of Manning's formula. *Journal of Geophysical Research*, 65(4):1310–1311, 1960.

[12] C.P. Liou. Limitations and proper use of the Hazen-Williams equation. *Journal of Hydraulic Engineering*, 124(9):951–954, 1998.

[13] J.D. Valiantzas. Modified Hazen-Williams and Darcy-Weisbach equations for friction and local head losses along irrigation laterals. *Journal of Irrigation and Drainage Engineering*, 131(4):342–350, 2005.

[14] A. Bergant, A.R. Simpson, and J. Vítkovský. Developments in unsteady pipe friction modelling. *Journal of Hydraulic Research*, 39(3):249–257, 2001.

[15] A.E. Vardy and K.L. Hwang. A characteristics model of transient friction in pipes. *Journal of Hydraulic Research*, 29(5):669–684, 1991.

[16] W.F. Silva-Araya and M.H. Chaudhry. Computation of energy dissipation in transient flow. *Journal of Hydraulic Engineering*, 123(2):108–115, 1997.

[17] G. Pezzinga. Quasi-2D model for unsteady flow in pipe networks. *Journal of Hydraulic Engineering*, 125(7):676–685, 1999.

[18] P.T. Storli. Transient friction in pressurized pipes; the water hammer phenomenon, 2010.

[19] B. Brunone, U.M. Golia, and M. Greco. Some remarks on the momentum equation for fast transients. *International Meeting on Hydraulic Transients with Column Spearation, 9th Round Table*, pages 140–148, 1991.

[20] W. Zielke. Frequency-dependent friction in transient pipe flow. *Journal of Basic Engineering*, 90(1):109–115, 1968.

[21] K. Suzuki, T. Taketomi, and S. Sato. Improving Zielke's method of simulating frequency-dependent friction in laminar liquid pipe flow. *Journal of Fluids Engineering*, 113(4):569–573, 1991.

[22] A.E. Vardy, K.L. Hwang, and J.M.B. Brown. A weighting model of transient turbulent pipe friction. *Journal of Hydraulic Research*, 31:533–548, 1993.

[23] A.E. Vardy and J.M.B. Brown. Transient, turbulent, smooth pipe friction. *Journal of Hydraulic Research*, 33:435–456, 1995.

[24] L. Rikstad. Design of a test rig for investigations of flow transient, NTNU, 2016.

[25] I. Bergset. Investigations of a harmonic oscillatory flow, NTNU, 2017.

[26] E.B. Wylie, V.L. Streeter, and L. Suo. *Fluid Transients in Systems*. Prentice-Hall, Englewood Cliffs, NJ, 1993.

[27] K.A. Hamran. Simulations and measurements of friction in oscillating flow, NTNU, 2018.

[28] R. Vennatrø. An experimental and theoretical analysis of non-steady turbulent flow in circular smooth pipes, 2000.

[29] M.H. Chaudhry, M.A. Sabbah, and J.E. Fowler. Analysis and stability of closed surge tanks. *Journal of Hydraulic Engineering*, 111(7):1079–1096, 1985.

[30] J. Stoer and R. Bulirsch. *Introduction to Numerical Analysis*. Springer, 3rd edition, 2002.

[31] B.R. Munson, T.H. Okiishi, W.W. Huebsch, and A.P. Rothmayer. *Fluid Mechanics*. Wylie, 7th edition, 2013.

[32] P.P. Jonsson, J. Ramdal, and M.J. Cervantes. Development of the Gibson method - unsteady friction. *Flow Measurement and Instrumentation*, 23:19–25, 2012.

[33] L.R.J. Sundstrom and M.J. Cervantes. Transient wall shear stress measurements and estimates at high Reynolds numbers. *Flow Measurement and Instrumentation*, 58:112–119, 2017.

[34] A.S. Morris and R. Langari. *Measurement and Instrumentation Theory and Application*. Butterworth-Heinemann, 2012.

[35] F. Hofmann. Principles of electromagnetic flow measurement, 2011.

[36] Krohne. OPTIFLUX 2000 Technical Datasheet. `https://cdn.krohne.com/dlc/TD_OPTIFLUX2000_en_171123_4000086806_R10.pdf`, 2017, Accessed 31.01.2019.

[37] F. Hofmann. Fundamental principles of electromagnetic flow measurement. 2003.

[38] G. Fowles and W.H. Boyes. *Instrumentation Reference Book*. Butterworth-Heinemann, 4th edition edition, 2010.

[39] A.V. Oppenheim, R.W. Schafer, and J.R. Buck. *Discrete-time Signal Processing*. Prentice Hall, 2nd edition, 1998.

[40] SAC-Singlas (Singapore accreditation council). Technical guide 1 Guidelines on the evaluation and expression of measurement uncertainty, 2001.

[41] R.E Walpole, R.H Myers, S.L. Myers, and K. Ye. *Probability and Statistics for Engineers and Scientists*. Prentice Hall, 7th edition, 2002.

[42] K.D. Jensen. Flow measurements. *Journal of the Brazilian Society of Mechanical Sciences and Engineering*, 26(4):400–419, 2004.

[43] H. Hodson. Hot-wire anemometers. `http://www-g.eng.cam.ac.uk/whittle/current-research/hph/hot-wire/hot-wire.html`, Accessed 29.01.19. University of Cambridge.

[44] A. Tselentis. Application of hot-wire (-film) flowmeters to water velocity measurements in wells. *Journal of Hydrology*, 58(3-4):375–381, 1982.

[45] R.J. Goldstein. *Fluid Mechanics Measurements*. Taylor & Francis, 2nd edition, 1996.

[46] G.E. Miller. Position sensitivity of hot-film shear probes. *Journal of Physics E: Scientific Instruments*, 13(9), 1980.

[47] C.R. Lodahl, B.M. Sumer, and J. Fredsøe. Turbulent combined oscillatory flow and current in a pipe. *Journal of Fluid Mechanics*, 373:313–348, 1998.

[48] S. He and J.D. Jackson. A study of turbulence under conditions of transient flow in a pipe. *Journal of Fluid Mechanics*, 408:1–38, 2000.

[49] B. Brunone, B.W. Karney, M. Mecarelli, and M. Ferrante. Velocity profiles and unsteady pipe friction in transient flow. *Journal of Water Resources Planning and Management*, 126(4):236–244, 2000.

[50] P.E. Hughes and T.V. How. Pulsatile velocity distribution and wall shear rate measurement using pulsed doppler ultrasound. *Journal of Biomechanics*, 27(1):103–110, 1994.

[51] C.W.H. van Doorne and J. Westerweel. Measurement of laminar, transitional and turbulent pipe flow using stereoscopic-piv. *Experiments in Fluids*, 42(2):259–279, 2007.

[52] L.R.J. Sundstrom and M.J. Cervantes. On the similarity of pulsating and accelerating turbulent pipe flows. *Flow, Turbulence and Combustion*, 100:417–436, 2018.

[53] J. Takeuchi, S. Satake, N.B. Morley, T. Yokomine, T. Kunugi, and M.A. Abdou. Piv measurements of turbulence statistics and near-wall structure of fully developed pipe flow at high Reynolds number. *6th International Symposium on Particle Image Velocimetry*, 2005.

[54] GE Sensing. Ptx/pmp 1400 specifications. `http://oihcontrols.co.za/wp-content/uploads/2014/05/ptx-pmp_1400_0-1.pdf`, 2005.

[55] GE Oil and gas. UNIK 5000 pressure sensing platform. `https://www.industrial.ai/sites/g/files/cozyhq596/files/acquiadam_assets/unik_5000_datasheet.pdf`, 2009.

[56] Druck Limitd. Druck DPI 601 portable pressure indicator/calibrator user manual. `https://www.avionteq.com/document/DPI-601-user-manual.pdf`, 1995.

A Derivation of the governing equations for fluid transients

In this appendix the governing equations for fluid transients are derived. The derivations are excerpted and adapted from the project work [27] written by the author in the fall semester of 2018, which was based on derivations in [26, Chapter 2].

The equations governing transient flow can be derived from the equations for conservation of mass and conservation of momentum.

The forces acting on a fluid element with constant cross sectional area, A, are shown in Figure 45. There is a pressure force on each end, shear or friction force on the outer surface and gravity.

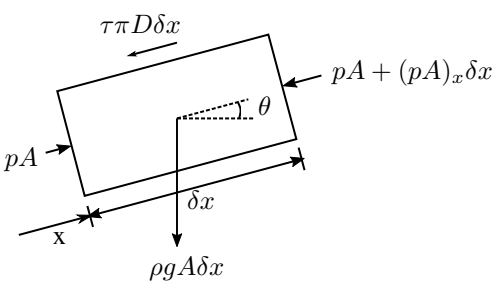

Figure 45: The shear, gravity and pressure forces acting on a fluid element with constant cross section. Figure based on [26].

According to the momentum equation, summation of forces should equal mass times acceleration for the fluid element. The momentum equation in x-direction yields

$$pA - (p + p_x\delta x)\,A - \tau\pi D\delta x - \rho gA\delta x \sin\theta = \rho A\delta x\dot{V} \tag{A.1}$$

where $\dot{V}$ is the total derivative, given by $\dot{V} = VV_x + V_t$. The pA in the equation above cancels. Dividing by δx yields

$$-p_x A - \tau\pi D - \rho gA\sin\theta = \rho A\dot{V} \tag{A.2}$$

Expanding the total derivative of the velocity, $\dot{V}$, yields

$$p_x A + \tau\pi D + \rho gA\sin\theta + \rho A(VV_x + V_t) = 0. \tag{A.3}$$

Using $A = \pi D^2/4$ for a circular cross section, and dividing by $A\rho g$ further yields

$$\frac{p_x}{\rho g} + \frac{4\tau}{\rho gD} + \sin\theta + \frac{1}{g}VV_x + \frac{1}{g}V_t = 0. \tag{A.4}$$

The piezometric head is $H = p/(\rho g) + z$ where z is the distance from datum to the fluid element. Differentiating this equation with respect to x yields

$$H_x = \frac{p_x}{\rho g} + \frac{dz}{dx} \tag{A.5}$$

where $\frac{dz}{dx} = \sin\theta$.

Using Equation A.5 to rewrite Equation A.4 for the piezometric head, yields

$$H_x + \frac{4\tau}{\rho gD} + \frac{1}{g}VV_x + \frac{1}{g}V_t = 0. \tag{A.6}$$

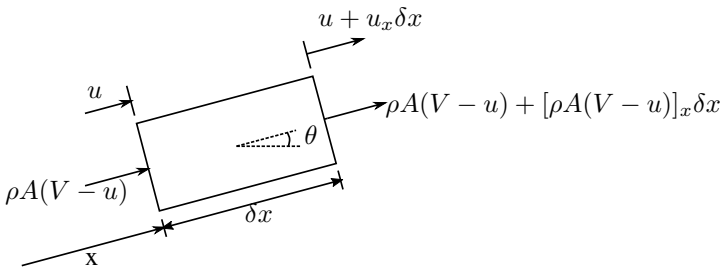

Figure 46: Control volume analysis for conservation of mass. Figure based on [26].

The continuity equation states that the net mass flux through a control surface must equal the time rate of change of mass inside the control volume. A control volume analysis for a pipe section is shown in Figure 46. The control volume is in this case fixed relative to the pipe, so that when the pipe stretches or moves, the control volume moves with it. For this case, continuity yields

$$-[\rho A(V-u)]_x\delta x = \frac{D'}{Dt}(\rho A\delta x) \tag{A.7}$$

where u is the velocity of the pipe wall in position x, V is the velocity of the fluid, and $\frac{D'}{Dt}$ is the total derivative with respect to the axial motion of the pipe, i.e. equal to $\frac{\partial}{\partial t} + u\frac{\partial}{\partial x}$. Expansion of Equation A.7 yields

$$[-(\rho AV)_x + (\rho Au)_x]\delta x = \delta x\frac{D'}{Dt}(\rho A) + \rho A\frac{D'}{Dt}\delta x \tag{A.8}$$

The time rate of increase of length δx of the control volume is

$$\frac{D'}{Dt}\delta x = u_x\delta x \tag{A.9}$$

so equation A.8 becomes

$$[-(\rho AV)_x + (\rho Au)_x]\delta x = \delta x\frac{D'}{Dt}(\rho A) + u_x\delta x\rho A \tag{A.10}$$

Dividing Equation A.10 by δx and expanding further by use of the total derivative, yields

$$(\rho AV)_x - (\rho Au)_x + (\rho A)_t + u(\rho A)_x + u_x\rho A = 0 \tag{A.11}$$

The second term in Equation A.11 cancels the two last terms on the left-hand side in the equation. Thus, one is left with the following,

$$(\rho AV)_x + (\rho A)_t = 0. \tag{A.12}$$

This can be written as $\rho AV_x + V(\rho A)_x + (\rho A)_t = 0$ where the two last terms on the left-hand side is the total derivative of ρA with respect to motion of a mass particle, $\frac{D}{Dt}(\rho A) = \frac{\partial}{\partial t}(\rho A) + V\frac{\partial}{\partial x}(\rho A)$. Thus, Equation A.12 can be written

$$\rho AV_x + \frac{D}{Dt}(\rho A) = 0, \tag{A.13}$$

The total derivative may be indicated by a dot over the dependent variable, so that $\frac{D}{Dt}(\rho A) = \rho\dot{A} + \dot{\rho}A$. Using this notation for equation A.13, and dividing by ρA yields

$$V_x + \frac{\dot{A}}{A} + \frac{\dot{\rho}}{\rho} = 0. \tag{A.14}$$

For prismatic tubes, $\dot{A}$ in the equation above will be a function of pressure only

$$\dot{A} = \frac{dA}{dp}\dot{p} \tag{A.15}$$

The third term in Equation A.14 can be rewritten to include the bulk modulus of elasticity of the fluid, defined as $K = \frac{\Delta p}{\Delta \rho / \rho}$. Doing this limits the validity of the equation to slightly compressible fluids only, but the third term can then be written as

$$\frac{\dot{\rho}}{\rho} = \frac{\dot{p}}{K}. \tag{A.16}$$

With A.15 and A.16, Equation A.14 becomes

$$V_x + \frac{\dot{p}}{K}\left(1 + \frac{K}{A}\frac{dA}{dp}\right) = 0. \tag{A.17}$$

With the speed of sound,

$$a = \sqrt{\frac{K/\rho}{1 + \frac{K}{A}\frac{\Delta A}{\Delta p}}} \tag{A.18}$$

as derived in Appendix B, Equation A.17 can be written

$$\rho a^2 V_x + \dot{p} = 0. \tag{A.19}$$

For steady flow, i.e. $\frac{\partial}{\partial t} = 0$, variation in density and pipe area are usually not considered for only slightly compressible fluids, so $V_x = 0$. Equation A.19 would thus yield $p_x = 0$ for steady flows. This seems to be a contradiction for steady flows in sloped tubes with or without friction or in horizontal tubes with friction. The inconsistency occurs since one allows elastic changes in the unsteady equation through the speed of sound, but one does not admit changes in density or area in steady state. To solve this inconsistency, V_x is eliminated by combining the complete unsteady partial differential equations of unsteady flows, Equation A.4 and Equation A.19. Inserting the expression for V_x obtained from Equation A.19 in Equation A.4 and expanding the total derivative of p, $\dot{p} = Vp_x + p_t$, yields after rearranging

$$p_x\left(1 - \left(\frac{V}{a}\right)^2\right) - \frac{V}{a^2}p_t + \rho V_t + \rho g \sin\theta + \frac{4\tau}{D} = 0. \tag{A.20}$$

For small Mach numbers, $Ma = \frac{V}{a} << 1$, the term containing this could be neglected in Equation A.20. In most applications, this is the case, and the transport term is neglected since it is very small compared to other terms. Thus, in the continuity equation, the term Vp_x is neglected. Leading to the following simplified continuity equation

$$\rho a^2 V_x + p_t = 0. \tag{A.21}$$

Equation A.21 is only valid for slightly compressible fluids flowing at low Mach numbers.

The pressure may be replaced by head, resulting in

$$H_t + \frac{a^2}{g}V_x = 0. \tag{A.22}$$

Similarly as in the continuity equation, the term VV_x can be neglected in the momentum equation, Equation A.6, for flow with low Mach number. This results in the following equation for conservation of momentum

$$H_x + h'_f + \frac{1}{g}V_t = 0. \tag{A.23}$$

where $h'_f = \frac{4\tau}{\rho g D}$ is head loss per unit length.

So the governing equations for transient flow are Equation A.22 and Equation A.23, where f is the friction factor and a is the speed of sound as given by Equation A.18. For thick-walled or rigid pipes $\Delta A/\Delta p$ is very small, so the term containing this part in the expression for the speed of sound is negligible. Thus, the speed of sound for a thick-walled pipe is

$$a = \sqrt{K/\rho}. \tag{A.24}$$

B Derivation of the speed of sound

This appendix is an excerpt from the derivation of speed of sound in the project work, written by this author in the fall semester of 2018 [27].

The derivation in this appendix is based on the one in [26, Chapter 1]. An expression for the speed of sound, a, can be derived from looking at stoppage of frictionless liquid in a horizontal pipe. The situation is depicted in Figure 47. As a valve is closed, a pressure wave will travel upstream with a velocity equal to the speed of sound.

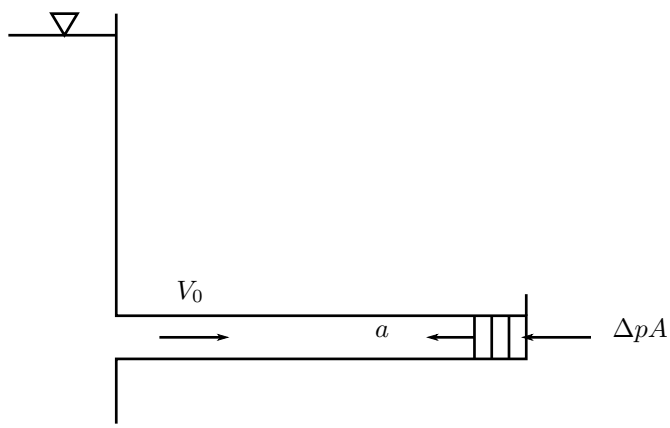

Figure 47: Stoppage of frictionless liquid in horizontal pipe. Figure from [26].

The momentum equation for the control volume in Figure 48 yields

$$-\Delta pA = A(a - V_0)[(\rho + \Delta\rho)(V_0 + \Delta V) - \rho V_0] + (\rho + \Delta\rho)A(V_0 + \Delta V)^2 - \rho A V_0^2 \tag{B.1}$$

where $A(a - V_0)\Delta t$ is the volume of fluid having its momentum changed.

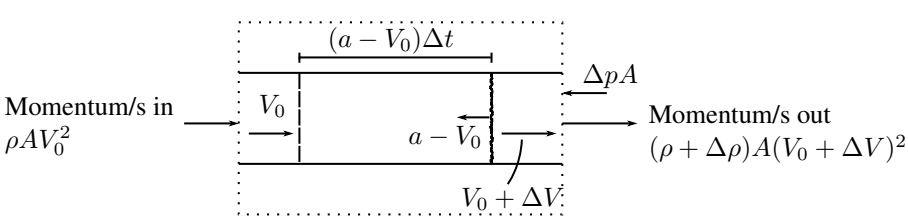

Figure 48: Control volume analysis for conservation of momentum. Figure from [26].

Conservation of mass yields

$$\rho A V_0 - (\rho + \Delta\rho)A(V_0 + V) = A(a - V_0)[(\rho + \Delta\rho) - \rho] \tag{B.2}$$

Combining the momentum equation, Equation B.1, and the continuity equation, Equation B.2, and simplifying yields

$$\Delta p = -\rho a \Delta V \tag{B.3}$$

To determine the magnitude of the speed of sound, Equation B.3 together with continuity is needed. In Figure 49, Δs is the length the pipe may stretch when a valve is closed downstream.

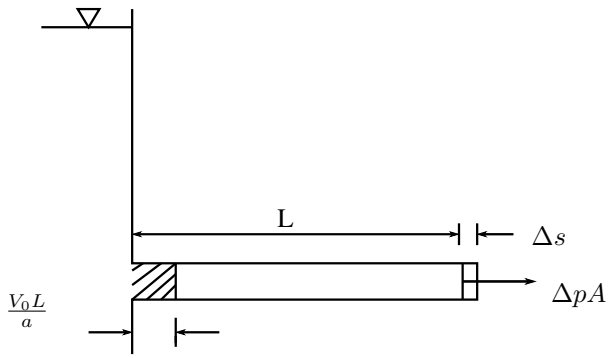

Figure 49: Continuity relations in pipe. Figure from [26].

The change in velocity of the fluid at the gate is

$$\Delta V = \frac{a\Delta s}{L} - V_0 \tag{B.4}$$

The mass entering the pipe during L/a seconds after valve closure is $\rho A V_0 L/a$. This extra mass is accommodated in the pipe by an increase in the cross sectional area, by utilizing the extra volume that occurred due to the pipe extension, Δs, and by compressing the liquid. Thus, continuity yields

$$\rho A V_0 \frac{L}{a} = \rho L \Delta A + \rho A \Delta s + L A \Delta \rho \tag{B.5}$$

Using Equation B.4 to eliminate V_0 in Equation B.5, and reorganizing, yields

$$-\frac{\Delta V}{a} = \frac{\Delta A}{A} + \frac{\Delta \rho}{\rho} \tag{B.6}$$

Using $\Delta p = -\rho a \Delta V$ to eliminate ΔV in Equation B.6, yields

$$\frac{\Delta p}{\rho a^2} = \frac{\Delta A}{A} + \frac{\Delta \rho}{\rho}. \tag{B.7}$$

Reorganizing this yields

$$a^2 = \frac{\Delta p/\rho}{\Delta A/A + \Delta \rho/\rho}. \tag{B.8}$$

With the definition of bulk velocity

$$K = \frac{\Delta p}{\Delta \rho/\rho}, \tag{B.9}$$

the expression for the speed of sound can be written as

$$a = \sqrt{\frac{K/\rho}{1 + (K/A)(\Delta A/\Delta p)}}. \tag{B.10}$$

For thick-walled pipes, $\Delta A/\Delta p$ is very small, so the term containing this part is negligible. Thus, the speed of sound for thick-walled pipes is

$$a = \sqrt{K/\rho}. \tag{B.11}$$

C Method of Characteristics

The derivation and description of the method of characteristics in this appendix is, unless otherwise stated, based on chapter 3 in Wylie and Streeter's Fluid Transients in Systems [26]. The partial differential equations for transient flow C.1 and C.2 are quasilinear hyperbolic partial differential equations where the velocity, V, and the hydraulic grade-line elevation, H, are the dependent variables, and time, t, and distance along the pipe, x, are the independent variables.

$$H_t + \frac{a^2}{g} V_x = 0 \tag{C.1}$$

$$gH_x + V_t + gh'_f = 0 \tag{C.2}$$

With the method of characteristics, these equations are transformed into four ordinary differential equations by linear combination of equation C.1 and equation C.2. Multiplying equation C.1 by an unknown constant, λ, and adding it to equation C.2 yields

$$\lambda \left(H_x \frac{g}{\lambda} + H_t \right) + \left(V_x \lambda \frac{a^2}{g} + V_t \right) + gh'_f = 0 \tag{C.3}$$

Since this equation is a linear combination of the two independent equations, C.1 and C.2, any two real, distinct values of λ will yield two equations that are equivalent to equation C.1 and C.2. By choosing the two values of λ in a certain way, equation C.3 will be simplified. Both V and H are generally functions of x and t. By setting the independent variable x to be a function of t, i.e. $x = x(t)$, the total derivatives of H and V are, by use of the chain rule, as follows.

$$\frac{dH}{dt} = H_x \frac{dx}{dt} + H_t \tag{C.4}$$

$$\frac{dV}{dt} = V_x \frac{dx}{dt} + V_t \tag{C.5}$$

Comparing equation C.4 and C.5 with C.3, it can be seen that for certain values of λ, equation C.3 can be written in terms of the total derivatives. In order for the parentheses in equation C.3 to be equal to the total derivatives, one must have the following

$$\frac{dx}{dt} = \frac{g}{\lambda} = \frac{\lambda a^2}{g} \tag{C.6}$$

This leads to

$$\lambda = \pm \frac{g}{a} \tag{C.7}$$

Equation C.3 can now be written as

$$\lambda \frac{dH}{dt} + \frac{dV}{dt} + gh'_f = 0 \tag{C.8}$$

for the values of λ given in equation C.7. Substituting C.7 back into C.6, the following relation is found

$$\frac{dx}{dt} = \pm a \tag{C.9}$$

So with the method of characteristics, the partial differential equations C.1 and C.2 are transformed into the following ordinary differential equations which are valid along characteristic lines in the x-t plane. The C$^+$ equation

$$\frac{g}{a}\frac{dH}{dt} + \frac{dV}{dt} + gh'_f = 0 \tag{C.10}$$

is valid along the characteristic line defined by $\frac{dx}{dt} = +a$, and the C$^-$ equation

$$-\frac{g}{a}\frac{dH}{dt} + \frac{dV}{dt} + gh'_f = 0 \tag{C.11}$$

is valid for $\frac{dx}{dt} = -a$.

The C$^+$ and C$^-$ equations can be solved by finite differences. A pipe of length L where solutions are wanted, is divided into N sections of length Δx. Solutions are found at each grid point or node. With N sections, there will be N+1 nodes.

Writing the C$^+$ equation in terms of Q rather than V, and multiplying it by $a\frac{dt}{g} = \frac{dx}{g}$, and integrating along the C$^+$ characteristic, yields [26, Chapter 3]

$$\int_{H_{i-1}}^{H_i} dH + \frac{a}{gA}\int_{Q_{i-1}}^{Q_i} dQ + \frac{f}{2gDA^2}\int_{x_{i-1}}^{x_i} Q|Q|dx = 0 \tag{C.12}$$

For the final term, the variation of Q with x is unknown, and an approximation must therefore be used [26, Chapter 3]. Using integration by parts to evaluate the last integral, the following is found.

$$\int_{x_{i-1}}^{x_i} Q^2 dx = Q^2 x\Big|_{x_{i-1}}^{x_i} - 2\int_{x_{i-1}}^{x_i} xQdQ \tag{C.13}$$

With the trapezoidal rule this integral can be approximated as

$$\int_{x_{i-1}}^{x_i} Q^2 dx \approx Q_i^2 x_i - Q_{i-1}^2 x_{i-1} - 2\left[\frac{x_i Q_i + x_{i-1}Q_{i-1}}{2}(Q_i - Q_{i-1})\right] \approx Q_i|Q_{i-1}|(x_i - x_{i-1}) \tag{C.14}$$

With this approximation, the linear form of the integrated equations is maintained. It is a second-order accurate approximation which is satisfactory for most cases. Other approximations may also be used, and can be found in for example Chaudhry's book Applied Hydraulic Transients [3, Chapter 3]. By use of the second-order approximation, equation C.12 becomes

$$H_i - H_{i-1} + \frac{a}{gA}(Q_i - Q_{i-1}) + \frac{f\Delta x}{2gDA^2}Q_i|Q_{i-1}| = 0 \tag{C.15}$$

Similarly, integration of the C$^-$ equation will yield the following equation,

$$H_i - H_{i+1} - \frac{a}{gA}(Q_i - Q_{i+1}) - \frac{f\Delta x}{2gDA^2}Q_i|Q_{i+1}| = 0 \tag{C.16}$$

Solving for H_P this becomes

$$H_i = H_{i-1} - B(Q_i - Q_{i-1}) - RQ_i|Q_{i-1}| \tag{C.17}$$

$$H_i = H_{i+1} + B(Q_i - Q_{i+1}) - RQ_i|Q_{i+1}| = 0 \tag{C.18}$$

with $B = \frac{a}{gA}$ and $R = \frac{f\Delta x}{2gDA^2}$.

By introducing the following coefficients

$$C_P = H_{i-1} + BQ_{i-1} \tag{C.19}$$

$$C_M = H_{i+1} - BQ_{i+1} \tag{C.20}$$

$$B_P = B + R|Q_{i-1}| \tag{C.21}$$

$$B_M = B + R|Q_{i+1}| \tag{C.22}$$

the C^+ and C^- equations may be rewritten as mentioned in section 3.3.1, into the following equations

$$H_i = C_P - B_P Q_i \tag{C.23}$$

and

$$H_i = C_M + B_M Q_i \tag{C.24}$$

By combining equation C.23 and C.24, Q_i can be eliminated, and the following expression for H_i may be obtained

$$H_i = \frac{C_P B_M + C_M B_P}{B_P + B_M} \tag{C.25}$$

Q_i can be found directly from equation C.23 or C.24, or from the following expression, which was found by combining C.23 and C.24

$$Q_i = \frac{C_P - C_M}{B_P + B_M}. \tag{C.26}$$

C.1 Boundary conditions

C.1.1 Reservoir

When the entrance losses at the inlet from the reservoir to the pipe is included, the equation for the head at the first node is as described in the theory section

$$H_{1,j+1} = H_{res} - (1+k)\frac{Q_{1,j+1}^2}{2gA^2} \tag{C.27}$$

by use of the energy equation. k is the loss coefficient. The C^- equation, equation C.24, for $i = 1$, may be used to eliminate $H_{1,j+1}$ from equation C.27. The following equation is found after rearranging

$$\frac{1+k}{2gA^2}Q_{1,j+1}^2 + B_M Q + C_M - H_{res} = 0 \tag{C.28}$$

This quadratic equation is easily solved for $Q_{i,j+1}$, resulting in the following expression for the flow rate at the reservoir boundary

$$Q_{1,j+1} = \frac{-B_M + \sqrt{B_M^2 - 4k_1(C_M H_{res}}}{2k_1} \tag{C.29}$$

The head may then be found from equation C.24.

C.1.2 Valve

At the valve, located at node $N+1$, an orifice equation can be used for the flow through the valve.

$$Q_{N+1} = C_d A_G \sqrt{2gH_{N+1}} \tag{C.30}$$

where C_d is the discharge coefficient and A_G the area of the valve opening. Dividing this by the equation for flow through the valve for the initial steady flow, $Q_0 = (C_d A_G)_0 \sqrt{2gH_0}$, yields

$$Q_{N+1} = \frac{Q_0}{\sqrt{H_0}} \tau \sqrt{H_{N+1}} \tag{C.31}$$

Inserting the expression for H_{N+1} from equation C.23 into this equation, yields the following quadratic equation

$$Q_{N+1} + \frac{(Q_0\tau)^2}{H_0} B_P Q_{N+1} - \frac{(Q_0\tau)^2}{H_0} C_P = 0 \tag{C.32}$$

Solving this equation for Q_{N+1}, yields the following boundary condition for the flow rate at the valve

$$Q_{N+1} = -B_P C_v + \sqrt{(B_P C_v)^2 + 2C_v C_P} \tag{C.33}$$

where $C_v = \frac{(Q_0\tau)^2}{2H_0}$. The head at the valve, H_{N+1} can be found from equation C.23.

C.1.3 Surge shaft

The equations in this section are taken from Tullis' book Hydraulics of Pipelines [8, Chapter 9], but the same notation as in Fluid Transients in Systems have been used for the C^+ and C^- equations, i.e. the coefficients C_P and C_M are as defined previously in this thesis, and not equal to Tullis' definitions of the coefficients. The following equations are used in order to find $H(i, j+1)$ and $Q(i, j+1)$ at the surge shaft. Both the C^+ and C^- equations are needed:

$$H(i, j+1) = C_P - B_P Q(i, j+1) \tag{C.34}$$

$$H(i, j+1) = C_M + B_M Q(i+1, j+1) \tag{C.35}$$

where equation C.37 was used in the last equation. The continuity equation is used, with flow into the surge shaft, Qs, defined as positive.

$$Q(i, j+1) = Qs(j+1) + Q(i+1, j+1) \tag{C.36}$$

And the energy equation at the junction, when losses are neglected

$$H(i, j+1) = H(i+1, j+1) \tag{C.37}$$

The datum is set equal to the middle of the pipe.

For the surge shaft one assumes that the water level changes relatively little during one time interval, Δt, and the head loss at the junction of the surge shaft and the pipe is neglected [8, Chapter 9]. Then, the water level in the surge tank can be found either with a first or second order approximation [8, Chapter 9]. The first order approximation is as follows

$$H(i, j+1) = H(i, j) + Qs(j) \frac{\Delta t}{A} \tag{C.38}$$

With this approximation, the solution of the all the above equations is direct, starting from $H(i, j+1)$. However, the following second order approximation is recommended [8, Chapter 9].

$$H(i, j+1) = H(i, j) + \frac{\Delta t(Qs(j+1) + Qs(j))}{2A} \tag{C.39}$$

With the second order approximation, the equations have to be solved with the following expressions. By substituting equation C.34 and C.36 into equation C.39, one obtains

$$C_P - B_P Q(i, j+1) = H(i, j) + \frac{\Delta t}{2A}(Q(i, j+1) - Q(i+1, j+1) + Qs(j)). \tag{C.40}$$

From equation C.35 with C.34 the following expression for the flow one node downstream of the surge shaft at the new time level, $Q(i+1, j+1)$ is obtained as

$$Q(i+1, j+1) = \frac{H(i, j+1) - C_M}{B_P} = \frac{C_P - B_P Q(i, j+1) - C_M}{B_P} \tag{C.41}$$

Inserting this into equation C.40 and solving for $Q(i, j+1)$ yields

$$Q(i, j+1) = \frac{C1 + C3}{2 + C2} \tag{C.42}$$

with $C1 = 2A\frac{C_P - H(i,j)}{\Delta t} - Qs(j)$, $C2 = 2\frac{AB_P}{\Delta t}$ and $C3 = \frac{C_P - C_M}{B_P}$.

$H(i, j+1)$ can then be found from equation C.34, $Q(i+1, j+1)$ from equation C.35, and $Qs(j+1)$ from C.36 [8, Chapter 9].

D Simplification of the governing equations with rigid liquid column theory

By assuming that the water in the pipe acts as a rigid liquid column the governing equations 3 and 4 are reduced to ordinary differential equations. As described in section 3.2, the water is considered incompressible and the pipe walls are considered rigid [26, Chapter 5]. Since the mass density is constant, the bulk modulus of elasticity, K, will go to infinity, and thus the speed of sound, a, will also go to infinity [26, Chapter 5]. The continuity equation,

$$H_t + \frac{a^2}{g} V_x = 0 \tag{D.1}$$

is then reduced to the following by dividing by a^2 and then neglecting the term H_t/a^2 as this will go to zero when a goes to infinity.

$$V_x = 0 \tag{D.2}$$

This implies that when rigid liquid column theory is assumed, the velocity will not be a function of position, only of time. Thus, there will at all instants, be one common fluid particle velocity in the pipe [26, Chapter 5].

Since the velocity is a function of time only, it can be written as the time derivative of the position. For the position of the free surface in the surge shaft this means $V = \frac{dz}{dt}$. Since flow rate is equal to velocity times cross sectional area, an expression for the flow in the surge shaft is

$$Q_s = VA_s = \frac{dz}{dt} A_s \tag{D.3}$$

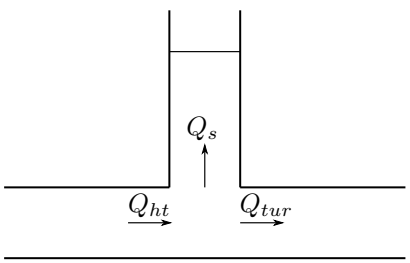

Figure 50: Flow at the surge shaft junction.

Conservation of mass at the junction of the surge shaft and the horizontal pipe, yields

$$Q_{ht} = Q_s + Q_{tur} \tag{D.4}$$

where Q_{ht} is the flow in the headrace tunnel, Q_s is the flow into the surge shaft, and Q_{tur} is the flow into the surge shaft as seen in Figure 50 [3, Chapter 11].

Inserting the expression for Q_s from equation D.4 into equation D.3, yields the following expression for the change in water level in the surge shaft [3, Chapter 11]

$$\frac{dz}{dt} = \frac{1}{A_s}(Q_{ht} - Q_{tur}) \tag{D.5}$$

After the valve is closed, and the oscillations have started, $Q_{tur} = 0$, so that equation D.5 becomes

$$\frac{dz}{dt} = \frac{1}{A_s} Q_{ht} \tag{D.6}$$

The second equation governing transient flow, derived from the momentum equation,

$$H_x + \frac{1}{g} V_t + h'_f = 0 \tag{D.7}$$

may be simplified by replacing the x-derivative of the head, H, with $\frac{H_2-H_1}{L}$. Also writing the equation in terms of Q instead of V, i.e. replacing V_t with $\frac{Q_t}{A}$, yields

$$\frac{H_2 - H_1}{L} + \frac{1}{g}\frac{Q_t}{A} + h'_f = 0 \tag{D.8}$$

Multiplying by L and rearranging yields

$$\frac{L}{gA}Q_t = H_1 - H_2 - h_f \tag{D.9}$$

with $z = H_1 - H - 2$ this is equal to equation 18.

Approximate formulas for the frequency and the amplitude of the oscillations can be found by looking at the case when losses are neglected.

When losses are neglected, the momentum equation becomes

$$\frac{dQ_t}{dt} = -\frac{gA_t}{L}z \tag{D.10}$$

Differentiating equation D.6 with respect to time and inserting the resulting expression for dQ_t/dt into equation D.10, yields the following differential equation.

$$\frac{d^2z}{dt^2} + \frac{gA_t}{A_sL}z = 0 \tag{D.11}$$

The solution to this equation is [3, Chapter 11]

$$z = C_1 \cos\sqrt{\frac{gA_t}{LA_s}}t + C_2 \sin\sqrt{\frac{gA_t}{LA_s}}t \tag{D.12}$$

The constants C_1 and C_2 can be found from the initial conditions [3, Chapter 11]. In this case, $z(t = 0) = 0$ and $\frac{dz(t=0)}{dt} = \frac{Q_0}{A_s}$, so that $C_1 = 0$ and $C_2 = Q_0\sqrt{\frac{L}{gA_sA_t}}$. The solution of D.11 thus becomes

$$z = Q_0\sqrt{\frac{L}{gA_sA_t}} \sin\sqrt{\frac{gA_t}{LA_s}}t \tag{D.13}$$

The amplitude of the oscillations in the surge shaft can be found from equation D.13 as

$$Z = Q_0\sqrt{\frac{L}{gA_sA_t}} \tag{D.14}$$

when losses are neglected [3, Chapter 11]. The frequency of the oscillations is

$$\omega = \sqrt{\frac{gA_t}{LA_s}}, \tag{D.15}$$

and, consequently, the period is [2]

$$T = \frac{2\pi}{\omega}. \tag{D.16}$$

E Calibration

E.1 Calibration of the electromagnetic flowmeter

The points used for the calibration of the flowmeter are shown in Table 9, and the resulting linear calibration graph is shown in Figure 51.

Voltage [V]	Flow rate [m^3/h]
2.000	0.0
2.190	4.8
2.240	6.0
2.300	7.5
2.421	10.5
2.613	15.3
2.754	18.8
2.910	22.7
3.030	25.7
3.110	27.7
3.144	28.5
3.190	29.7
3.300	32.4
3.450	36.2
3.570	39.2
3.740	43.4

Table 9: Points used for the calibration of the electromagnetic flowmeter.

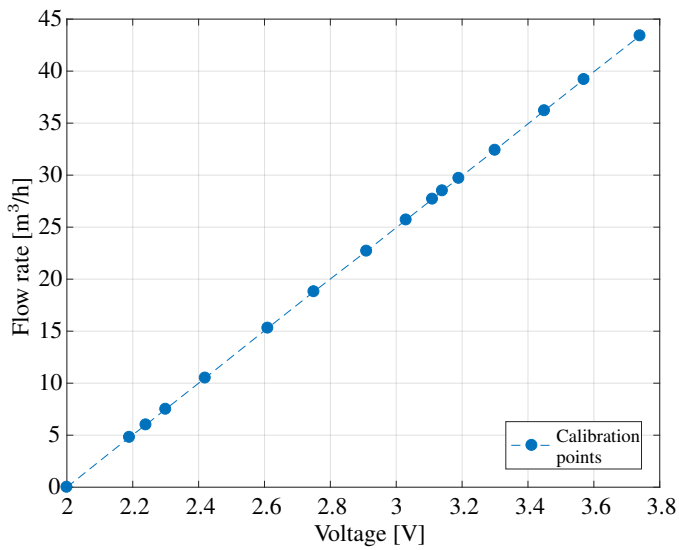

Figure 51: Linear regression graph for the calibration of the electromagnetic flowmeter.

E.2 Calibration of the pressure transducers

The calibration for each of the four pressure transducers are shown in this section. The points used for the calibration of the transducers are shown in Tables 10, 11, 12, and 13, for the PT1, PT2, PT3, and the PT4, respectively. The resulting calibration graphs are shown in Figures 52, 53, 54, and 55.

PT1	
2.05	0.000
2.35	0.096
2.80	0.237
3.23	0.372
3.50	0.456
3.72	0.526
3.95	0.598
4.39	0.735
4.58	0.796
4.93	0.905
5.23	1.000

Table 10: Points used for the calibration of the PT1.

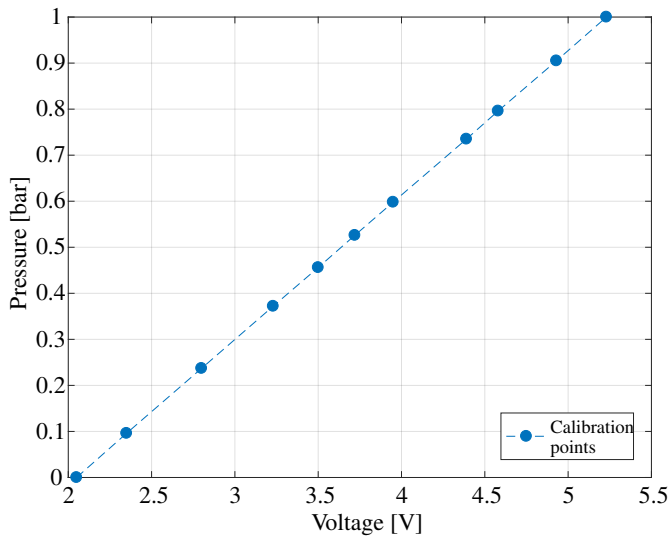

Figure 52: Linear regression graph for the calibration of the PT1.

PT2	
2.01	0.000
2.23	0.140
2.32	0.195
2.51	0.314
2.68	0.419
2.87	0.540
3.06	0.657
3.22	0.761
3.36	0.845
3.51	0.940
3.66	1.031

Table 11: Points used for the calibration of the PT2.

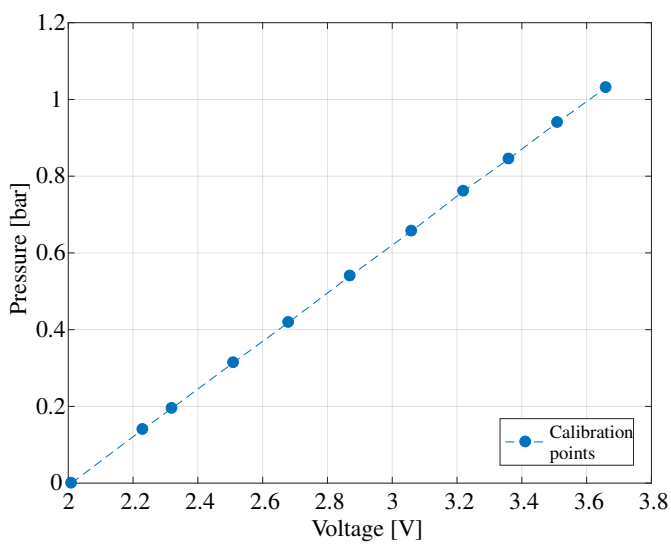

Figure 53: Linear regression graph for the calibration of the PT2.

PT3	
2.00	0.000
2.14	0.084
2.33	0.203
2.44	0.276
2.60	0.370
2.73	0.453
2.93	0.577
3.26	0.785
3.43	0.889
3.64	1.020
3.78	1.109

Table 12: Points used for the calibration of the PT3.

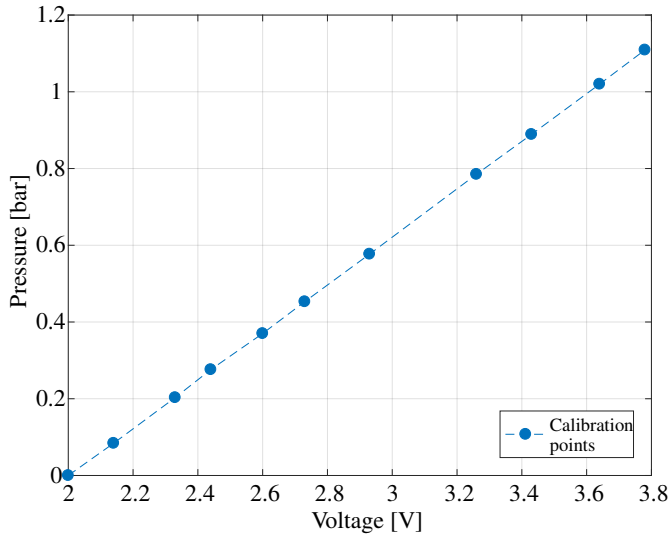

Figure 54: Linear regression graph for the calibration of the PT3.

PT4	
2.01	0.000
2.18	0.108
2.37	0.225
2.54	0.333
2.70	0.431
2.96	0.595
3.10	0.682
3.27	0.786
3.47	0.910
3.59	0.987
3.66	1.032

Table 13: The points used for the calibration of the PT4.

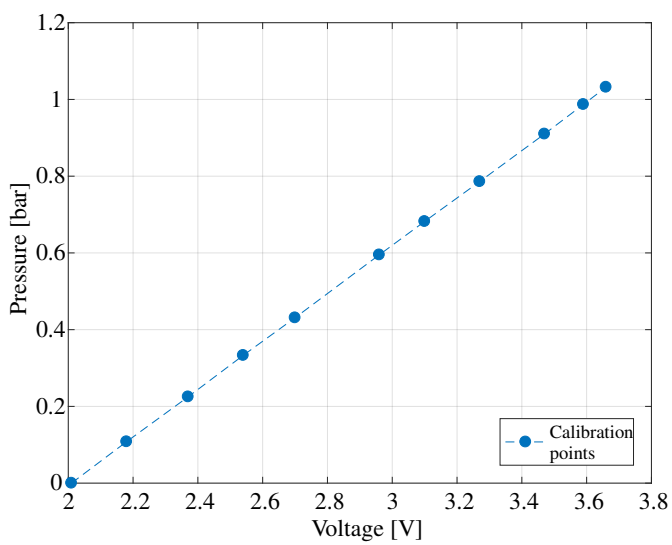

Figure 55: Linear regression graphs from the calibration of the PT4.

F Experimental results

The following figures show plots from the experiments with initial flow rate equal to 0.007 m^3/s. In the figures on the left, Figure 56a, 57a, 58a, 59a, and 60a, the measurement results for the five valve closures are plotted together. In the figures on the right, Figure 56b, 57b, 58b, 59b, and 60b, the average of the five runs is plotted, for PT1, PT2, PT3, PT4 and the EMF, respectively.

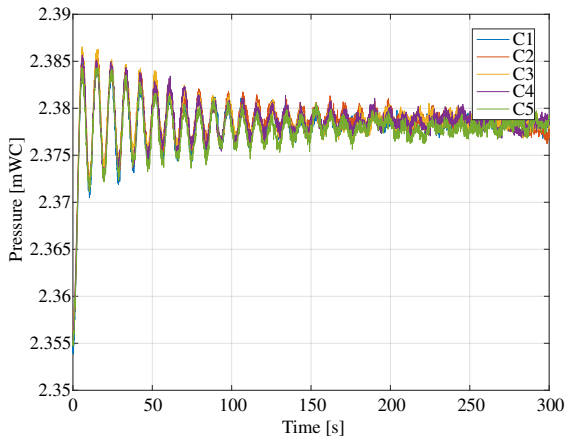

(a) All PT1 measurements for the five closures plotted together.

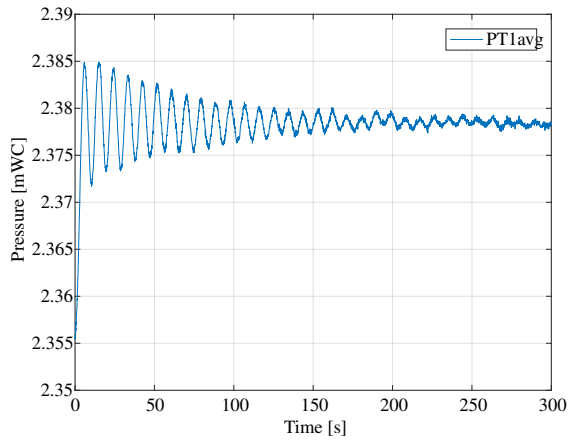

(b) Average of the five PT1 measurements.

Figure 56: Raw measurement data and averaged data from PT1.

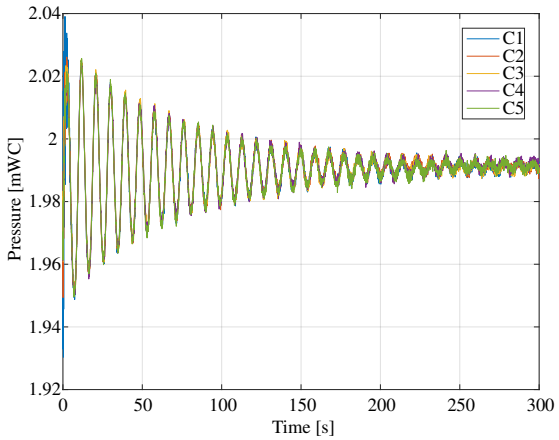

(a) All PT2 measurements for the five closures plotted together.

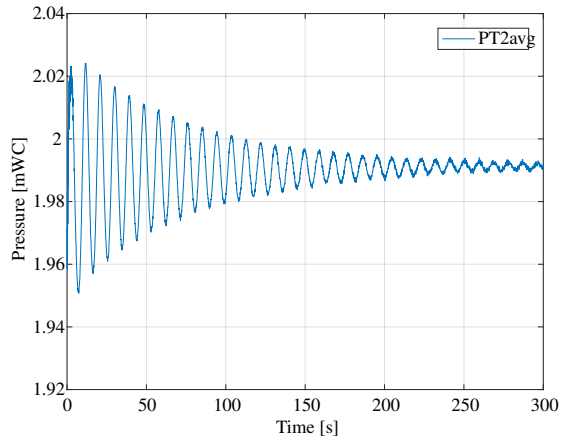

(b) Average of the five PT2 measurements.

Figure 57: Raw measurement data and averaged data from PT2.

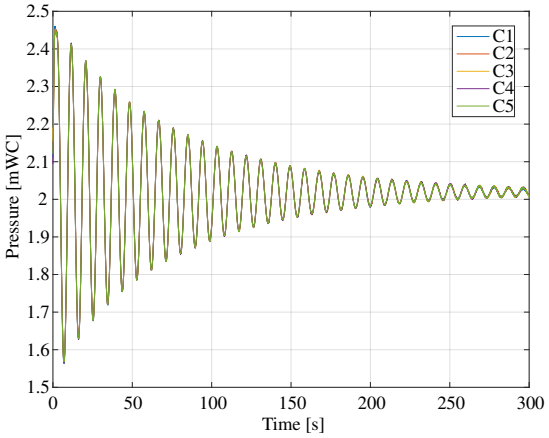

(a) All PT3 measurements for the five closures plotted together.

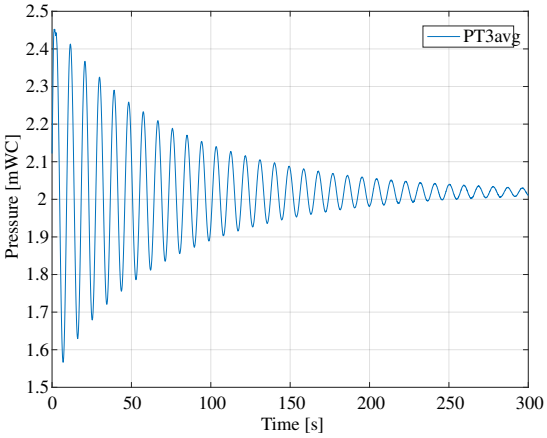

(b) Average of the five PT3 measurements.

Figure 58: Raw measurement data and averaged data from PT3.

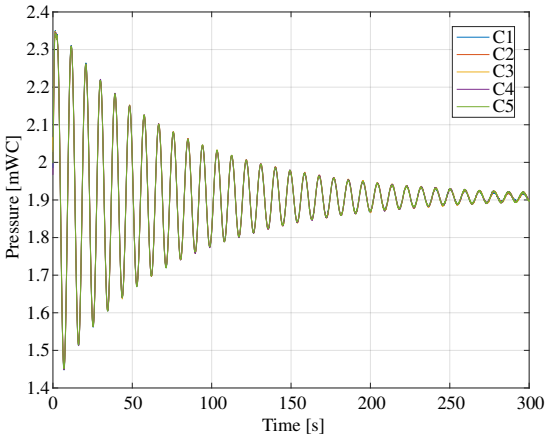

(a) All PT4 measurements for the five closures plotted together.

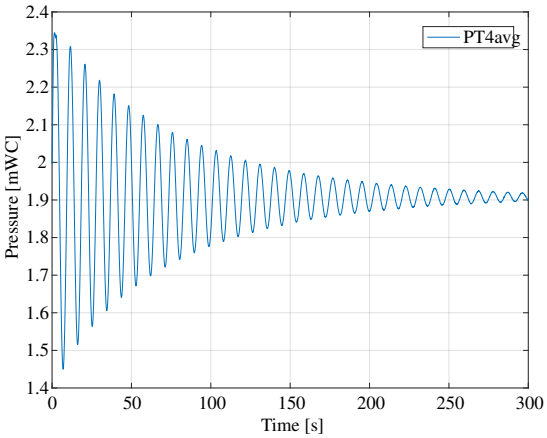

(b) Average of the five PT4 measurements.

Figure 59: Raw measurement data and averaged data from PT4.

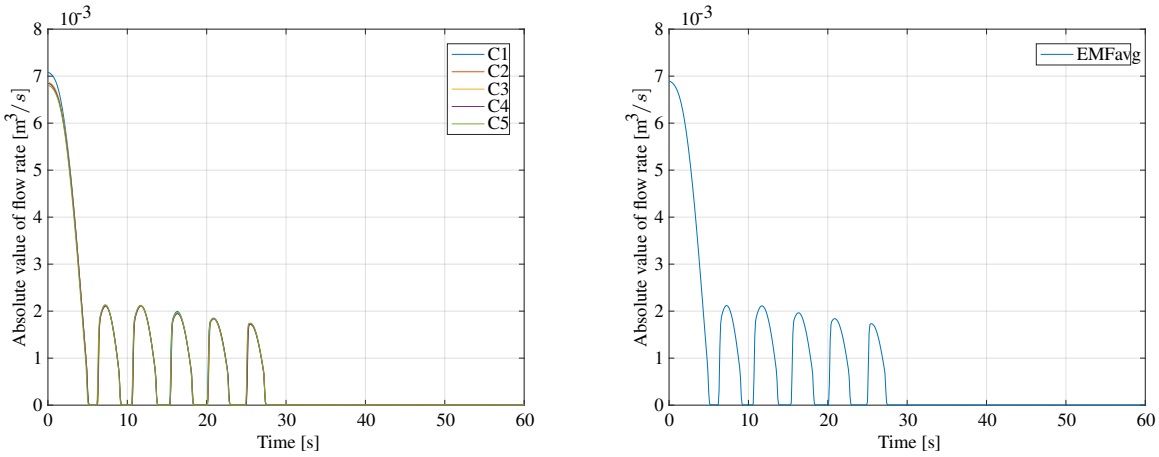

(a) All EMF measurements for the five closures plotted together.

(b) Average of the five EMF measurements.

Figure 60: Raw measurement data and averaged data from the EMF.

G MATLAB code: Uncertainty calculations

The MATLAB script used to calculate the uncertainty of the pressure and flow rate measurements is included in the following pages.

```
%% Uncertainty calculations
clear all
close all
clc

% Constants
g=9.82; % Gravitational acceleration [m/s^2]
rho=999.1; % Density [kg/m^3]

% Load the measurement files, and select the elements for the valve
% closures and apply calibration constants
file=load('test007.lvm');
timeC1=file(173860:273860,1)-file(173860,1); % [s]
EMFC1=(file(173860:273860,2)*24.933-49.83)/3600; % [m^3/s]
PT1C1=(file(173860:273860,3)*0.314-0.6427)*10^5/(rho*g); % [mWC]
PT2C1=(file(173860:273860,4)*0.6254-1.2558)*10^5/(rho*g); % [mWC]
PT3C1=(file(173860:273860,5)*0.6234-1.2484)*10^5/(rho*g); % [mWC]
PT4C1=(file(173860:273860,6)*0.624-1.2532)*10^5/(rho*g); % [mWC]
timeC2=file(435460:535460,1)-file(435460,1); % [s]
EMFC2=(file(435460:535460,2)*24.933-49.83)/3600; % [m^3/s]
PT1C2=(file(435460:535460,3)*0.314-0.6427)*10^5/(rho*g); % [mWC]
PT2C2=(file(435460:535460,4)*0.6254-1.2558)*10^5/(rho*g); % [mWC]
PT3C2=(file(435460:535460,5)*0.6234-1.2484)*10^5/(rho*g); % [mWC]
PT4C2=(file(435460:535460,6)*0.624-1.2532)*10^5/(rho*g); % [mWC]
timeC3=file(673805:773805,1)-file(673805,1); % [s]
EMFC3=(file(673805:773805,2)*24.933-49.83)/3600; % [m^3/s]
PT1C3=(file(673805:773805,3)*0.314-0.6427)*10^5/(rho*g); % [mWC]
PT2C3=(file(673805:773805,4)*0.6254-1.2558)*10^5/(rho*g); % [mWC]
PT3C3=(file(673805:773805,5)*0.6234-1.2484)*10^5/(rho*g); % [mWC]
PT4C3=(file(673805:773805,6)*0.624-1.2532)*10^5/(rho*g); % [mWC]
timeC4=file(912920:1012920,1)-file(912920,1); % [s]
EMFC4=(file(912920:1012920,2)*24.933-49.83)/3600; % [m^3/s]
```

```
PT1C4=(file(912920:1012920,3)*0.314-0.6427)*10^5/(rho*g); % [mWC]
PT2C4=(file(912920:1012920,4)*0.6254-1.2558)*10^5/(rho*g); % [mWC]
PT3C4=(file(912920:1012920,5)*0.6234-1.2484)*10^5/(rho*g); % [mWC]
PT4C4=(file(912920:1012920,6)*0.624-1.2532)*10^5/(rho*g); % [mWC]
timeC5=file(1153780:1253780,1)-file(1153780,1); % [s]
EMFC5=(file(1153780:1253780,2)*24.933-49.83)/3600; % [m^3/s]
PT1C5=(file(1153780:1253780,3)*0.314-0.6427)*10^5/(rho*g); % [mWC]
PT2C5=(file(1153780:1253780,4)*0.6254-1.2558)*10^5/(rho*g); % [mWC]
PT3C5=(file(1153780:1253780,5)*0.6234-1.2484)*10^5/(rho*g); % [mWC]
PT4C5=(file(1153780:1253780,6)*0.624-1.2532)*10^5/(rho*g); % [mWC]

time=[timeC1'; timeC2'; timeC3'; timeC4'; timeC5'];
EMF=[EMFC1'; EMFC2'; EMFC3'; EMFC4'; EMFC5'];
PT1=[PT1C1'; PT1C2'; PT1C3'; PT1C4'; PT1C5'];
PT2=[PT2C1'; PT2C2'; PT2C3'; PT2C4'; PT2C5'];
PT3=[PT3C1'; PT3C2'; PT3C3'; PT3C4'; PT3C5'];
PT4=[PT4C1'; PT4C2'; PT4C3'; PT4C4'; PT4C5'];

% Standard deviation of the five measurements
std_time=std(time);
std_EMF=std(EMF);
std_PT1=std(PT1);
std_PT2=std(PT2);
std_PT3=std(PT3);
std_PT4=std(PT4);

% Average of the five measurements
n=5;
EMFavg=(EMFC1+EMFC2+EMFC3+EMFC4+EMFC5)/n;
PT1avg=(PT1C1+PT1C2+PT1C3+PT1C4+PT1C5)/n;
PT2avg=(PT2C1+PT2C2+PT2C3+PT2C4+PT2C5)/n;
PT3avg=(PT3C1+PT3C2+PT3C3+PT3C4+PT3C5)/n;
PT4avg=(PT4C1+PT4C2+PT4C3+PT4C4+PT4C5)/n;

% Student t-value for a confidence level of 95% with n-1 degrees of freedom
t_value=tinv(0.95,n-1);
```

```
%Random error due to averaging of the five measurements
err_r_EMF=t_value*std_EMF./sqrt(n);
err_r_PT1=t_value*std_PT1./sqrt(n);
err_r_PT2=t_value*std_PT2./sqrt(n);
err_r_PT3=t_value*std_PT3./sqrt(n);
err_r_PT4=t_value*std_PT4./sqrt(n);

%Uncertainty
f_r_EMF=err_r_EMF./EMFavg';
f_r_PT1=err_r_PT1./PT1avg';
f_r_PT2=err_r_PT2./PT2avg';
f_r_PT3=err_r_PT3./PT3avg';
f_r_PT4=err_r_PT4./PT4avg';

%Systematic error for the pressure measurements
err_s_PTcal=0.05/100*10*10^5/(rho*g); % Systematic uncertainty in the DPI601: Accuracy=0.05% of full-scale value which is 10 bar, equal to 10*10^5/(rho*g) mWC.
err_s_PT1=0.15/100*2.5*10^5/(rho*g); %Systematic uncertainty PTX1400 pressure transducer: Accuracy: 0.15% of full-scale, 2.5 bar.
err_s_PT234=0.04/100*5*10^5/(rho*g); %Systematic uncertainty UNIK 5000 pressure transducer: Accuracy: 0.04% of full-scale, 5 bar.

%Combining the systematic errors with the root-sum-square method
f_s_PT1=@(P) sqrt((err_s_PTcal./P).^2+(err_s_PT1./P).^2); % Uncertainty for PT1.
f_s_PT234=@(P) sqrt((err_s_PTcal./P).^2+(err_s_PT234./P).^2); % Uncertainty for PT2, PT3, and PT4.

%Systematic error for the flowmeter
e_s_EMF=0.2/100*0.5556; %Systematic uncertainty flowmeter: Accuracy 0.2% of full-scale, 0.5556 m3/s
f_s_EMF=@(Q) sqrt((e_s_EMF./Q).^2); %Total systematic uncertainty in percent

%Total uncertainty for each point
```

```
f_EMF=sqrt(f_s_EMF(EMFavg').^2+f_r_EMF.^2); %Total uncertainty EMF
f_PT1=sqrt(f_s_PT1(PT1avg').^2+f_r_PT1.^2); %Total uncertainty PT1
f_PT2=sqrt(f_s_PT234(PT2avg').^2+f_r_PT2.^2); %Total uncertainty PT2
f_PT3=sqrt(f_s_PT234(PT3avg').^2+f_r_PT3.^2); %Total uncertainty PT3
f_PT4=sqrt(f_s_PT234(PT4avg').^2+f_r_PT4.^2); %Total uncertainty PT4

%Total error in each average point
e_EMF=abs(f_EMF.*EMFavg');
e_PT1=abs(f_PT1.*PT1avg');
e_PT2=abs(f_PT2.*PT2avg');
e_PT3=abs(f_PT3.*PT3avg');
e_PT4=abs(f_PT4.*PT4avg');


figure(1)
plot(timeC1,EMFavg,timeC1,EMFavg+e_EMF',timeC1,EMFavg-e_EMF')
legend('EMF','Upper bound','Lower bound')
xlabel('Time [s]')
ylabel('Absolute value of flow rate [m$^3$/s]')

figure(2)
plot(timeC1,PT1avg,timeC1,PT1avg+e_PT1',timeC1,PT1avg-e_PT1')
legend('PT1','Upper bound','Lower bound')
xlabel('Time [s]')
ylabel('Pressure [mWC]')

figure(3)
plot(timeC1,PT2avg,timeC1,PT2avg+e_PT2',timeC1,PT2avg-e_PT2')
legend('PT2','Upper bound','Lower bound')
xlabel('Time [s]')
ylabel('Pressure [mWC]')

figure(4)
plot(timeC1,PT3avg,timeC1,PT3avg+e_PT3',timeC1,PT3avg-e_PT3')
legend('PT3','Upper bound','Lower bound')
xlabel('Time [s]')
```

```
ylabel('Pressure [mWC]')

figure(5)
plot(timeC1,PT4avg,timeC1,PT4avg+e_PT4',timeC1,PT4avg-e_PT4')
legend('PT4','Upper bound','Lower bound')
xlabel('Time [s]')
ylabel('Pressure [mWC]')


% Uncertainty due to average across every 20th elements
n=20;
timeavg20=arrayfun(@(i) mean(timeC1(i:i+n-1)),1:n:length(timeC1)-n+1)';
EMFavg20=arrayfun(@(i) mean(EMFavg(i:i+n-1)),1:n:length(EMFavg)-n+1)';
PT1avg20=arrayfun(@(i) mean(PT1avg(i:i+n-1)),1:n:length(PT1avg)-n+1)';
PT2avg20=arrayfun(@(i) mean(PT2avg(i:i+n-1)),1:n:length(PT2avg)-n+1)';
PT3avg20=arrayfun(@(i) mean(PT3avg(i:i+n-1)),1:n:length(PT3avg)-n+1)';
PT4avg20=arrayfun(@(i) mean(PT4avg(i:i+n-1)),1:n:length(PT4avg)-n+1)';

% Standard deviation
std_EMFn20=arrayfun(@(i) std(EMFavg(i:i+n-1)),1:n:length(EMFavg)-n+1);
std_PT1n20=arrayfun(@(i) std(PT1avg(i:i+n-1)),1:n:length(PT1avg)-n+1);
std_PT2n20=arrayfun(@(i) std(PT2avg(i:i+n-1)),1:n:length(PT2avg)-n+1);
std_PT3n20=arrayfun(@(i) std(PT3avg(i:i+n-1)),1:n:length(PT3avg)-n+1);
std_PT4n20=arrayfun(@(i) std(PT4avg(i:i+n-1)),1:n:length(PT4avg)-n+1);

% Finding the student t-value
t_valuen20=tinv(0.95,n-1);

%Random error due to averaging with n=20
err_r_EMF20=((t_valuen20*std_EMFn20)./sqrt(n));
err_r_PT120=((t_valuen20*std_PT1n20)./sqrt(n));
err_r_PT220=((t_valuen20*std_PT2n20)./sqrt(n));
err_r_PT320=((t_valuen20*std_PT3n20)./sqrt(n));
err_r_PT420=((t_valuen20*std_PT4n20)./sqrt(n));

%Uncertainty
```

```
f_r_EMF20=(err_r_EMF20./EMFavg20');
f_r_PT120=(err_r_PT120./PT1avg20');
f_r_PT220=(err_r_PT220./PT2avg20');
f_r_PT320=(err_r_PT320./PT3avg20');
f_r_PT420=(err_r_PT420./PT4avg20');

n=20;
timen20C1=arrayfun(@(i) mean(timeC1(i:i+n-1)),1:n:length(timeC1)-n+1)';
timen20C2=arrayfun(@(i) mean(timeC2(i:i+n-1)),1:n:length(timeC2)-n+1)';
timen20C3=arrayfun(@(i) mean(timeC3(i:i+n-1)),1:n:length(timeC3)-n+1)';
timen20C4=arrayfun(@(i) mean(timeC4(i:i+n-1)),1:n:length(timeC4)-n+1)';
timen20C5=arrayfun(@(i) mean(timeC5(i:i+n-1)),1:n:length(timeC5)-n+1)';
EMFn20C1=arrayfun(@(i) mean(EMFC1(i:i+n-1)),1:n:length(EMFC1)-n+1)';
EMFn20C2=arrayfun(@(i) mean(EMFC2(i:i+n-1)),1:n:length(EMFC2)-n+1)';
EMFn20C3=arrayfun(@(i) mean(EMFC3(i:i+n-1)),1:n:length(EMFC3)-n+1)';
EMFn20C4=arrayfun(@(i) mean(EMFC4(i:i+n-1)),1:n:length(EMFC4)-n+1)';
EMFn20C5=arrayfun(@(i) mean(EMFC5(i:i+n-1)),1:n:length(EMFC5)-n+1)';
PT1n20C1=arrayfun(@(i) mean(PT1C1(i:i+n-1)),1:n:length(PT1C1)-n+1)';
PT1n20C2=arrayfun(@(i) mean(PT1C2(i:i+n-1)),1:n:length(PT1C2)-n+1)';
PT1n20C3=arrayfun(@(i) mean(PT1C3(i:i+n-1)),1:n:length(PT1C3)-n+1)';
PT1n20C4=arrayfun(@(i) mean(PT1C4(i:i+n-1)),1:n:length(PT1C4)-n+1)';
PT1n20C5=arrayfun(@(i) mean(PT1C5(i:i+n-1)),1:n:length(PT1C5)-n+1)';
PT2n20C1=arrayfun(@(i) mean(PT2C1(i:i+n-1)),1:n:length(PT2C1)-n+1)';
PT2n20C2=arrayfun(@(i) mean(PT2C2(i:i+n-1)),1:n:length(PT2C2)-n+1)';
PT2n20C3=arrayfun(@(i) mean(PT2C3(i:i+n-1)),1:n:length(PT2C3)-n+1)';
PT2n20C4=arrayfun(@(i) mean(PT2C4(i:i+n-1)),1:n:length(PT2C4)-n+1)';
PT2n20C5=arrayfun(@(i) mean(PT2C5(i:i+n-1)),1:n:length(PT2C5)-n+1)';
PT3n20C1=arrayfun(@(i) mean(PT3C1(i:i+n-1)),1:n:length(PT3C1)-n+1)';
PT3n20C2=arrayfun(@(i) mean(PT3C2(i:i+n-1)),1:n:length(PT3C2)-n+1)';
PT3n20C3=arrayfun(@(i) mean(PT3C3(i:i+n-1)),1:n:length(PT3C3)-n+1)';
PT3n20C4=arrayfun(@(i) mean(PT3C4(i:i+n-1)),1:n:length(PT3C4)-n+1)';
PT3n20C5=arrayfun(@(i) mean(PT3C5(i:i+n-1)),1:n:length(PT3C5)-n+1)';
PT4n20C1=arrayfun(@(i) mean(PT4C1(i:i+n-1)),1:n:length(PT4C1)-n+1)';
PT4n20C2=arrayfun(@(i) mean(PT4C2(i:i+n-1)),1:n:length(PT4C2)-n+1)';
PT4n20C3=arrayfun(@(i) mean(PT4C3(i:i+n-1)),1:n:length(PT4C3)-n+1)';
PT4n20C4=arrayfun(@(i) mean(PT4C4(i:i+n-1)),1:n:length(PT4C4)-n+1)';
```

```
PT4n20C5=arrayfun(@(i) mean(PT4C5(i:i+n-1)),1:n:length(PT4C5)-n+1)';


time=[timen20C1'; timen20C2'; timen20C3'; timen20C4'; timen20C5'];
EMF=[EMFn20C1'; EMFn20C2'; EMFn20C3'; EMFn20C4'; EMFn20C5'];
PT1=[PT1n20C1'; PT1n20C2'; PT1n20C3'; PT1n20C4'; PT1n20C5'];
PT2=[PT2n20C1'; PT2n20C2'; PT2n20C3'; PT2n20C4'; PT2n20C5'];
PT3=[PT3n20C1'; PT3n20C2'; PT3n20C3'; PT3n20C4'; PT3n20C5'];
PT4=[PT4n20C1'; PT4n20C2'; PT4n20C3'; PT4n20C4'; PT4n20C5'];

% Standard deviation between the five measurements
std_EMF=std(time);
std_PT1=std(EMF);
std_PT2=std(PT1);
std_PT3=std(PT3);
std_PT4=std(PT4);

% Averaging across the five measurements
n=5;
timeULTavg=(timen20C1+timen20C2+timen20C3+timen20C4+timen20C5)/n;
EMFULTavg=(EMFn20C1+EMFn20C2+EMFn20C3+EMFn20C4+EMFn20C5)/n;
PT1ULTavg=(PT1n20C1+PT1n20C2+PT1n20C3+PT1n20C4+PT1n20C5)/n;
PT2ULTavg=(PT2n20C1+PT2n20C2+PT2n20C3+PT2n20C4+PT2n20C5)/n;
PT3ULTavg=(PT3n20C1+PT3n20C2+PT3n20C3+PT3n20C4+PT3n20C5)/n;
PT4ULTavg=(PT4n20C1+PT4n20C2+PT4n20C3+PT4n20C4+PT4n20C5)/n;

% Student t-value for a confidence level of 95% with n-1 degrees of freedom
t_value=tinv(0.95,n-1);

%Random error due to averaging of the five measurements
err_r_EMF=((t_value*std_EMF)./sqrt(n));
err_r_PT1=((t_value*std_PT1)./sqrt(n));
err_r_PT2=((t_value*std_PT2)./sqrt(n));
err_r_PT3=((t_value*std_PT3)./sqrt(n));
err_r_PT4=((t_value*std_PT4)./sqrt(n));

```

```
%Uncertainty
f_r_EMF=(err_r_EMF./EMFULTavg');
f_r_PT1=(err_r_PT1./PT1ULTavg');
f_r_PT2=(err_r_PT2./PT2ULTavg');
f_r_PT3=(err_r_PT3./PT3ULTavg');
f_r_PT4=(err_r_PT4./PT4ULTavg');

%Systematic error for the pressure measurements
err_s_PTcal=0.05/100*10*10^5/(rho*g); % Systematic uncertainty in the DPI601: Accuracy=0.05% of full-scale value which is 10 bar, equal to 10*10^5/(rho*g) mWC.
err_s_PT1=0.15/100*2.5*10^5/(rho*g); %Systematic uncertainty PTX1400 pressure transducer: Accuracy: 0.15% of full-scale, 2.5 bar.
err_s_PT234=0.04/100*5*10^5/(rho*g); %Systematic uncertainty UNIK 5000 pressure transducer: Accuracy: 0.04% of full-scale, 5 bar.

%Combining the systematic errors with the root-sum-square method
f_s_PT1=@(P) sqrt((err_s_PTcal./P).^2+(err_s_PT1./P).^2); % Uncertainty for PT1.
f_s_PT234=@(P) sqrt((err_s_PTcal./P).^2+(err_s_PT234./P).^2); % Uncertainty for PT2, PT3, and PT4.

%Systematic error for the flowmeter
e_s_EMF=0.2/100*0.5556; %Systematic uncertainty flowmeter: Accuracy 0.2% of full-scale, 0.5556 m3/s
f_s_EMF=@(Q) sqrt((e_s_EMF./Q).^2); %Total systematic uncertainty in percent

%Total uncertainty for each point
f_EMF=sqrt((f_s_EMF(EMFULTavg').^2)+(f_r_EMF.^2)+f_r_EMF20.^2); %Total uncertainty EMF
f_PT1=sqrt((f_s_PT1(PT1ULTavg').^2)+(f_r_PT1.^2)+f_r_PT120.^2); %Total uncertainty PT1
f_PT2=sqrt((f_s_PT234(PT2ULTavg').^2)+(f_r_PT2.^2)+f_r_PT220.^2); %Total uncertainty PT2
f_PT3=sqrt((f_s_PT234(PT3ULTavg').^2)+(f_r_PT3.^2)+f_r_PT320.^2); %Total uncertainty PT3
```

```
f_PT4=sqrt((f_s_PT234(PT4ULTavg').^2)+(f_r_PT4.^2)+f_r_PT420.^2); %Total uncertainty PT4

%Total error in each average point
e_EMF=abs(f_EMF.*EMFULTavg');
e_PT1=abs(f_PT1.*PT1ULTavg');
e_PT2=abs(f_PT2.*PT2ULTavg');
e_PT3=abs(f_PT3.*PT3ULTavg');
e_PT4=abs(f_PT4.*PT4ULTavg');

%% Plots
figure(1)
plot(timeULTavg,EMFULTavg,timeULTavg,EMFULTavg+e_EMF',timeULTavg,EMFULTavg-e_EMF')
legend('EMF','Upper bound','Lower bound')
xlabel('Time [s]')
ylabel('Absolute value of flow rate [m$^3$/s]')

figure(2)
plot(timeULTavg,EMFULTavg,timeULTavg,EMFULTavg+e_EMF',timeULTavg,EMFULTavg-e_EMF')
legend('EMF','Upper bound','Lower bound')
xlabel('Time [s]')
ylabel('Absolute value of flow rate [m$^3$/s]')
xlim([0 50])

figure(3)
plot(timen20C1,PT1ULTavg,timen20C1,PT1ULTavg+e_PT1',timen20C1,PT1ULTavg-e_PT1')
legend('PT1','Upper bound','Lower bound')
xlabel('Time [s]')
ylabel('Pressure [mWC]')

figure(4)
plot(timen20C1,PT1ULTavg,timen20C1,PT1ULTavg+e_PT1',timen20C1,PT1ULTavg-e_PT1')
```

```
legend('PT1','Upper bound','Lower bound')
xlabel('Time [s]')
ylabel('Pressure [mWC]')
xlim([0 50])

figure(5)
plot(timen20C1,PT2ULTavg,timen20C1,PT2ULTavg+e_PT2',timen20C1,PT2ULTavg-e_PT2
    ')
legend('PT2','Upper bound','Lower bound')
xlabel('Time [s]')
ylabel('Pressure [mWC]')

figure(6)
plot(timen20C1,PT2ULTavg,timen20C1,PT2ULTavg+e_PT2',timen20C1,PT2ULTavg-e_PT2
    ')
legend('PT2','Upper bound','Lower bound')
xlabel('Time [s]')
ylabel('Pressure [mWC]')
xlim([0 50])

figure(7)
plot(timen20C1,PT3ULTavg,timen20C1,PT3ULTavg+e_PT3',timen20C1,PT3ULTavg-e_PT3
    ')
legend('PT3','Upper bound','Lower bound')
xlabel('Time [s]')
ylabel('Pressure [mWC]')

figure(8)
plot(timen20C1,PT3ULTavg,timen20C1,PT3ULTavg+e_PT3',timen20C1,PT3ULTavg-e_PT3
    ')
legend('PT3','Upper bound','Lower bound')
xlabel('Time [s]')
ylabel('Pressure [mWC]')
xlim([100 150])

figure(9)
```

```
plot(timen20C1,PT4ULTavg,timen20C1,PT4ULTavg+e_PT4',timen20C1,PT4ULTavg-e_PT4
    ')
legend('PT4','Upper bound','Lower bound')
xlabel('Time [s]')
ylabel('Pressure [mWC]')

figure(10)
plot(timen20C1,PT4ULTavg,timen20C1,PT4ULTavg+e_PT4',timen20C1,PT4ULTavg-e_PT4
    ')
legend('PT4','Upper bound','Lower bound')
xlabel('Time [s]')
ylabel('Pressure [mWC]')
xlim([100 150])

% Maximum errors
maxEMFerror=max(e_EMF);
maxPT1error=max(e_PT1);
maxPT2error=max(e_PT2);
maxPT3error=max(e_PT3);
maxPT4error=max(e_PT4);
```

H MATLAB code: Method of Characteristics

The MATLAB script for the simulations with the method of characteristics is included in the following pages.

```
%% Method of Characteristics
% Simulations of mass oscillations with the method of characteristics
clear all
close all
clc

% Constants
D=0.15; % Pipe diameter [m]
A=pi*D^2/4; % Pipe cross sectional area [m^2]
g=9.82; % Gravitational acceleration [m/s^2]
rho=999.1; % Density [kg/m^3]
mu=1.138e-3; % Dynamic viscosity [kg/(ms)]
nu=mu/rho; % Kinematic viscosity [m^2/s]
epsilon=2e-6; %Pipe roughness [m]
K=2.15e9; % Bulk modulus of water [Pa]

% Defining colors for the plots
myblue=[0 0.447 0.7410];
myred=[0.85 0.325 0.098];

%% Method of Characteristics
a=900; % Speed of sound [m/s]

Qinit=0.007;
Re=abs(Qinit)/A*D/nu; % Reynolds number
if Re<2300
    f=64/Re;
else
    f=1/(-1.8*log10(6.9/Re+((epsilon/D)/3.7)^1.11))^2; % Turbulent friction
        factor given by Haaland's relation
end
k=3.5; % Minor loss coefficient
hm=k/(2*g*A^2)*Qinit*abs(Qinit); % Minor loss
```

```
Hres=2.0209; % Reservoir level

N=140;
L=21;
dx=L/N;
dt=dx/a;

x=1:L/dx+1;
xmeters=x*dx-dx;

B=a/(g*A); % Pipeline characteristic impedance (Wylie and Streeter)
R=f*dx/(2*g*D*A^2); % Pipeline resistance coefficient (Wylie and Streeter)

tmax=501;
itend=tmax/dt;

H=zeros(N+1,round(itend)+1);
Q=zeros(N+1,round(itend)+1);
tauvec=zeros(1,round(itend)+1);
tauvec(1,:)=1;

%Steady state flow
Q0=0.007;
H0=Hres-R*N*Q0^2;

%Initial values
QI=Q0;
Q(:,1)=QI;
for i=1:N-1
    H(i,1)=Hres-((i-1)*f*dx/D+k)*QI^2;
end
H(N,1)=H(N-1,1);
for i=N+1
    H(i,1)=Hres-((i-2)*f*dx/D+k)*QI^2;
end
```

```
QT=zeros(1,round(itend)+1);
QT(1,1)=0;
tidisek=0;

for j=1:tmax/dt

    for i=2:N-2 % Interior points located before the surge shaft
        Re=abs(Q(i,j))/A*D/nu; % Updating the Reynolds number
        if Re<2300
            f=64/Re; % Laminar friction factor
        else
            f=1/(-1.8*log10(6.9/Re+((epsilon/D)/3.7)^1.11))^2; % Turbulent
                friction factor given by Haaland's relation
        end
        R=f*dx/(2*g*D*A^2);

        Cp=H(i-1,j)+B*Q(i-1,j);
        Bp=B+R*abs(Q(i-1,j));
        Cm=H(i+1,j)-B*Q(i+1,j);
        Bm=B+R*abs(Q(i+1,j));

        H(i,j+1)=(Cp*Bm+Cm*Bp)/(Bp+Bm);
        Q(i,j+1)=(Cp-Cm)/(Bp+Bm);
    end

    for i=N-1 %SURGE SHAFT
        CP=H(i-1,j)+B*Q(i-1,j);% Wylies notation
        CM=H(i+1,j)-B*Q(i+1,j);
        BP=B+R*abs(Q(i-1,j));
        C1=2*A*(CP-H(i,j))/dt-QT(1,j);
        C2=2*A*BP/dt;
        C3=(CP-CM)/BP;
        Q(i,j+1)=(C1+C3)/(2+C2);

        H(i,j+1)=CP-BP*Q(i,j+1);
```

```
        BM=B+R*abs(Q(i+2,j));
        CMdownstream=H(i+2,j)-BM*Q(i+2,j);
        Q(i+1,j+1)=(H(i,j+1)-CMdownstream)/BP;
        QT(1,j+1)=Q(i,j+1)-Q(i+1,j+1);

        H(i,j+1)=H(i,j)+dt*(QT(1,j+1)+QT(1,j))/(2*A);
        H(i+1,j+1)=H(i,j+1);
    end

    for i=1 % Reservoir boundary
        BM=B+R*abs(Q(i+1,j));
        CM=H(i+1,j)-B*Q(i+1,j);
        Q(i,j+1)=(-BM+sqrt(BM^2-4*(1+k)/(2*g*A^2)*(CM-Hres)))/(2*(1+k)/(2*g*A
            ^2));
        H(i,j+1)=CM+BM*Q(i,j+1);
    end

    for i=N+1 % Valve
        Re=abs(Q(i,j))/A*D/nu; % Reynolds number
        if tidisek<=2
            tau=1-(1-0)*(tidisek/2)^0.75;
        else
            tau=0;
        end
        CVP=Q0*Q0/(2*H0);
        CV=tau*tau*CVP;
        CP=H(i-1,j)+Q(i-1,j)*B;
        BP=B+R*abs(Q(i-1,j));
        Q(i,j+1)=-CV*BP+sqrt(CV*CV*BP*BP+CV*CP*2);
        H(i,j+1)=CP-BP*Q(i,j+1);
    end
    tauvec(j+1)=tau;
    tidisek=tidisek+dt;
end

time=0:1:tmax/dt+1;
```

```
timeMOC=time*dt;

%% Measurements
file=load('test007.lvm');
time=file(:,1);
EMF=file(:,2);
PT1=file(:,3);
PT2=file(:,4);
PT3=file(:,5);
PT4=file(:,6);

% Calibration
EMF=(EMF*24.933-49.83)/3600; % [m^3/s]
PT1=(PT1*0.314-0.6427)*10.1925; % [mWC]
PT2=(PT2*0.6254-1.2558)*10.1925; % [mWC]
PT3=(PT3*0.6234-1.2484)*10.1925; % [mWC]
PT4=(PT4*0.624-1.2532)*10.1925; % [mWC]

% Averaging a bit
n=20;
timeavg=arrayfun(@(i) mean(time(i:i+n-1)),1:n:length(time)-n+1)';
EMFavg=arrayfun(@(i) mean(EMF(i:i+n-1)),1:n:length(EMF)-n+1)';
PT1avg=arrayfun(@(i) mean(PT1(i:i+n-1)),1:n:length(PT1)-n+1)';
PT2avg=arrayfun(@(i) mean(PT2(i:i+n-1)),1:n:length(PT2)-n+1)';
PT3avg=arrayfun(@(i) mean(PT3(i:i+n-1)),1:n:length(PT3)-n+1)';
PT4avg=arrayfun(@(i) mean(PT4(i:i+n-1)),1:n:length(PT4)-n+1)';

% Location of the transients
C1=8685:13693;
C2=21765:26773;
C3=33682:38690;
C4=45638:50646;
C5=57681:62689;

% Starting the time vectors at zero
timeavgC1=timeavg(C1);
```

```
timeavgC1=timeavgC1-timeavgC1(1);
timeavgC2=timeavg(C2);
timeavgC2=timeavgC2-timeavgC2(1);
timeavgC3=timeavg(C3);
timeavgC3=timeavgC3-timeavgC3(1);
timeavgC4=timeavg(C4);
timeavgC4=timeavgC4-timeavgC4(1);
timeavgC5=timeavg(C5);
timeavgC5=timeavgC5-timeavgC5(1);

% Average of the five measurements
CaverageEMF=(EMFavg(C1)+EMFavg(C2)+EMFavg(C3)+EMFavg(C4)+EMFavg(C5))/5;
CaveragePT1=(PT1avg(C1)+PT1avg(C2)+PT1avg(C3)+PT1avg(C4)+PT1avg(C5))/5;
CaveragePT2=(PT2avg(C1)+PT2avg(C2)+PT2avg(C3)+PT2avg(C4)+PT2avg(C5))/5;
CaveragePT3=(PT3avg(C1)+PT3avg(C2)+PT3avg(C3)+PT3avg(C4)+PT3avg(C5))/5;
CaveragePT4=(PT4avg(C1)+PT4avg(C2)+PT4avg(C3)+PT4avg(C4)+PT4avg(C5))/5;

% Plots of the head at the surge shaft
figure(1)
plot(timeMOC,H(N-1,:),'color',myred)
hold on
plot(timeavgC1,CaveragePT3,'color',myblue)
grid on
legend('MOC-QS','Measurement')
xlabel('Time [s]')
ylabel('Pressure [mWC]')
xlim([0 500])

figure(2)
plot(timeMOC,H(N-1,:),'color',myred)
hold on
plot(timeavgC1,CaveragePT3,'color',myblue)
grid on
legend('MOC-QS','Measurement')
xlabel('Time [s]')
ylabel('Pressure [mWC]')
```

```
xlim([0 100])

% Plot of the dimensionless valve opening
figure(3)
plot(timeMOC,tauvec)
grid on
legend('\tau')
xlabel('Time [s]')
ylabel('\tau [-]')
xlim([0 5])

% Difference calculations
Zvec3interp=interp1(timeMOC,H(N-1,:),timeavgC1); % Interpolates Zvec so it can be compared in the same points as CaveragePT3
% Preallocation
peakQS=zeros(1,54);
lowQS=zeros(1,54);
peakMeasQS=zeros(1,54);
lowMeasQS=zeros(1,54);
peaktimesQS=zeros(1,54);
lowtimesQS=zeros(1,54);
peakMeastime=zeros(1,54);
lowMeastime=zeros(1,54);

% Frequency for the mass oscillations
omegaM=sqrt(g./(A.*L./A));
% Period for the mass oscillations:
TM=2*pi./omegaM;

count=1;
i=1;
while count<length(CaveragePT3)-round(10*TM)
    [peakQS(i),indexpeakQS]=max(Zvec3interp(count:count+round(10*TM))); % 10*TM to get the peak, since in CaveragePT3 there is 0.1 s between each point
    [lowQS(i),indexlowQS]=min(Zvec3interp(count:count+round(10*TM)));
```

```
    [peakMeasQS(i),indexMEASpeak]=max(CaveragePT3(count:count+round(10*TM)));
    [lowMeasQS(i),indexMEASlow]=min(CaveragePT3(count:count+round(10*TM)));
    peaktimesQS(i)=timeavgC1(indexpeakQS+count); % time of the peaks in the QS model
    lowtimesQS(i)=timeavgC1(indexlowQS+count); % time of the mins in the QS model
    peakMeastime(i)=timeavgC1(indexMEASpeak+count);
    lowMeastime(i)=timeavgC1(indexMEASlow+count);
    count=count+round(10*TM);
    i=i+1;
end

% Removing the first peak
peakQS=peakQS(2:length(peakQS));
peakMeasQS=peakMeasQS(2:length(peakMeasQS));
peaktimesQS=peaktimesQS(2:length(peaktimesQS));
peakMeastime=peakMeastime(2:length(peakMeastime));

differencePeakQS=abs(peakQS-peakMeasQS);
differenceLowQS=abs(lowQS-lowMeasQS);
meandiffQSpeak=mean(differencePeakQS); %Mean of the difference in peaks btw the model and measurements
meandiffQSmin=mean(differenceLowQS); %Mean of the differences in minimas btw the model and measurements
meandiffQS=(meandiffQSpeak+meandiffQSmin)/2; % The average absolute difference between experimental results and simulations in each peak
maxdiffQSpeak=max(differencePeakQS); % The maximum absolute difference among the maxima
maxdiffQSlow=max(differenceLowQS); % The maximum absolute difference among the minima

% Finding the relative error
relativeErrorPeaks=abs((peakMeasQS-peakQS)./peakMeasQS);
relativeErrorLow=abs((lowMeasQS-lowQS)./lowMeasQS);
meanRelErrPeaks=mean(relativeErrorPeaks);
meanRelErrLow=mean(relativeErrorLow);
```

```
meanRelErr=(meanRelErrPeaks+meanRelErrLow)/2;
meanRelErrinPercent=meanRelErr*100;

% Plot of the relative error
figure(4)
r=plot(lowtimesQS,relativeErrorLow*100,'o','color','k');
hold on
s=plot(peaktimesQS,relativeErrorPeaks*100,'o','color',myblue);
grid on
r.MarkerSize = 3;
r.MarkerFaceColor='k';
s.MarkerSize = 3;
s.MarkerFaceColor=myblue;
xlabel('Time [s]')
ylabel('Relative error MOC QS [%]')
legend('Local minima','Local maxima','location','southeast')
```

I MATLAB code: Rigid Liquid Column Theory

The MATLAB script for the simulations with rigid liquid column theory is included in the following pages.

```
%% Rigid Liquid Column Theory
% Simulations of mass oscillations with rigid liquid column theory and
% Euler's method
clear all
close all
clc

%% Constants
D=0.15; % Pipe diameter [m]
A=pi*D^2/4; % Pipe cross sectional area [m^2]
g=9.82; % Gravitational acceleration [m/s^2]
rho=999.1; % Density [kg/m^3]
mu=1.138e-3; % Dynamic viscosity [kg/(ms)]
nu=mu/rho; % Kinematic viscosity [m^2/s]
epsilon=2e-6; %Pipe roughness [m]
K=2.15e9; % Bulk modulus of water [Pa]
L=21; % Length of pipe [m]

% Defining colors for the plots
myblue=[0 0.447 0.7410];
myred=[0.85 0.325 0.098];

%% Frequency calculations
% Frequency for the mass oscillations
omegaM=sqrt(g./(A.*L./A));

% Period for the mass oscillations:
TM=2*pi./omegaM;

% Speed of sound for a rigid pipe
a=sqrt(K/rho);

% Frequency for the water hammer
```

```
TW=4.*L/a;

% Period for the water hammer
omegaW=1./TW;

%% Measurements of test case with flow rate around 0.007 m^3/s

% Loading the experimental measurements
file=load('test007.lvm');
time=file(:,1);
EMF=file(:,2);
PT1=file(:,3);
PT2=file(:,4);
PT3=file(:,5);
PT4=file(:,6);

% Calibration and conversion from m^3/h to m^3/s, and bar to mWC
EMF=(EMF*24.933-49.83)/3600; % [m^3/s]
PT1=(PT1*0.314-0.6427)*10^5/(rho*g); % [mWC]
PT2=(PT2*0.6254-1.2558)*10^5/(rho*g); % [mWC]
PT3=(PT3*0.6234-1.2484)*10^5/(rho*g); % [mWC]
PT4=(PT4*0.624-1.2532)*10^5/(rho*g); % [mWC]

% Averaging
n=20;
timeavg=arrayfun(@(i) mean(time(i:i+n-1)),1:n:length(time)-n+1)';
EMFavg=arrayfun(@(i) mean(EMF(i:i+n-1)),1:n:length(EMF)-n+1)';
PT1avg=arrayfun(@(i) mean(PT1(i:i+n-1)),1:n:length(PT1)-n+1)';
PT2avg=arrayfun(@(i) mean(PT2(i:i+n-1)),1:n:length(PT2)-n+1)';
PT3avg=arrayfun(@(i) mean(PT3(i:i+n-1)),1:n:length(PT3)-n+1)';
PT4avg=arrayfun(@(i) mean(PT4(i:i+n-1)),1:n:length(PT4)-n+1)';

% Location of the transients, C1=transient after the first valve
% closure, etc.
C1=8694:13693;
C2=21774:26773;
```

```
C3=33691:38690;
C4=45647:50646;
C5=57690:62689;

% Starting the time at zero for each closure
timeavgC1=timeavg(C1);
timeavgC1=timeavgC1-timeavgC1(1);
timeavgC2=timeavg(C2);
timeavgC2=timeavgC2-timeavgC2(1);
timeavgC3=timeavg(C3);
timeavgC3=timeavgC3-timeavgC3(1);
timeavgC4=timeavg(C4);
timeavgC4=timeavgC4-timeavgC4(1);
timeavgC5=timeavg(C5);
timeavgC5=timeavgC5-timeavgC5(1);

% Measurement values averaged across the five runs
CaverageEMF=(EMFavg(C1)+EMFavg(C2)+EMFavg(C3)+EMFavg(C4)+EMFavg(C5))/5;
CaveragePT1=(PT1avg(C1)+PT1avg(C2)+PT1avg(C3)+PT1avg(C4)+PT1avg(C5))/5;
CaveragePT2=(PT2avg(C1)+PT2avg(C2)+PT2avg(C3)+PT2avg(C4)+PT2avg(C5))/5;
CaveragePT3=(PT3avg(C1)+PT3avg(C2)+PT3avg(C3)+PT3avg(C4)+PT3avg(C5))/5;
CaveragePT4=(PT4avg(C1)+PT4avg(C2)+PT4avg(C3)+PT4avg(C4)+PT4avg(C5))/5;

%% Quasi-steady friction model

dt=0.01; % Time step
tmax=600; % Maximum time for simulation

Q=-0.007; % Initial flow rate
Z=0; % Level variation in surge shaft
Zvec=zeros(1,tmax/dt); % Vector for storing the different Z values
counter=1;
Qvec=Zvec;
hLvec=Zvec;
hfvec=Zvec; % Vector for storing the friction loss
hmvec=Zvec; % Vector for storing the minor loss
```

```
for t=0:dt:tmax
    Re=abs(Q)/A*D/nu; % Updating the Reynolds number

    if Re<2300
        f=64/Re; % Laminar friction factor
    else
        f=1/(-1.8*log10(6.9/Re+((epsilon/D)/3.7)^1.11))^2; % Turbulent
            friction factor given by Haaland's relation
    end

    hf=f*L/(2*g*A^2*D)*Q*abs(Q); % Friction loss
    hfvec(counter)=hf;
    k=3.5; % Minor loss coefficient
    hm=k/(2*g*A^2)*Q*abs(Q); % Minor loss
    hmvec(counter)=hm;

    Q=Q+dt*g*A/L*(Z-hf-hm); % Updating the flow rate
    Z=Z-dt*Q/A; % Updating the water level
    Zvec(counter)=Z; % Storing the new water level in the Z vector
    Qvec(counter)=Q; % Storing the flow rate

    counter=counter+1; % Updating the iteration counter
end

% Plot
t=0:dt:tmax; % Creating the time vector for plotting
Zvec3=Zvec+mean(CaveragePT3); % Adding a constant so the model oscillates
    around the same point as the measurements

figure(1)
plot(t,Zvec3,'color',myred)
hold on
plot(timeavgC1,CaveragePT3,'color',myblue)
legend('RLCT-QS','Measurement')
grid on
```

```
xlabel('Time [s]')
ylabel('Pressure [mWC]')
xlim([0 500])


% Difference calculations
Zvec3interp=interp1(t,Zvec3,timeavgC1); % Interpolates Zvec so it can be compared in the same points as CaveragePT3

%Preallocation
peakQS=zeros(1,54);
lowQS=zeros(1,54);
peakMeasQS=zeros(1,54);
lowMeasQS=zeros(1,54);
peaktimesQS=zeros(1,54);
lowtimesQS=zeros(1,54);
peakMeastime=zeros(1,54);
lowMeastime=zeros(1,54);

count=1;
i=1;
while count<length(CaveragePT3)-round(10*TM)
[peakQS(i),indexpeakQS]=max(Zvec3interp(count:count+round(10*TM))); % 10*TM to get the peak, since in CaveragePT3 there is 0.1 s between each point
[lowQS(i),indexlowQS]=min(Zvec3interp(count:count+round(10*TM)));
[peakMeasQS(i),indexMEASpeak]=max(CaveragePT3(count:count+round(10*TM)));
[lowMeasQS(i),indexMEASlow]=min(CaveragePT3(count:count+round(10*TM)));
peaktimesQS(i)=timeavgC1(indexpeakQS+count); % time of the peaks in the QS model
lowtimesQS(i)=timeavgC1(indexlowQS+count); % time of the minima in the QS model
peakMeastime(i)=timeavgC1(indexMEASpeak+count);
lowMeastime(i)=timeavgC1(indexMEASlow+count);
count=count+round(10*TM);
i=i+1;
end
```

```
% Removing the first peak
peakQS=peakQS(2:length(peakQS));
peakMeasQS=peakMeasQS(2:length(peakMeasQS));
peaktimesQS=peaktimesQS(2:length(peaktimesQS));

differencePeakQS=abs(peakQS-peakMeasQS);
differenceLowQS=abs(lowQS-lowMeasQS);

meandiffQSpeak=mean(differencePeakQS); %Mean of the difference in peaks btw the model and measurements
meandiffQSmin=mean(differenceLowQS); %Mean of the differences in minimas btw the model and measurements
meandiffQS=(meandiffQSpeak+meandiffQSmin)/2; % The average absolute difference between experimental results and simulations in each peak
maxdiffQSpeak=max(differencePeakQS); % The maximum absolute difference among the maxima
maxdiffQSlow=max(differenceLowQS); % The maximum absolute difference among the minima

% Finding the relative error
relativeErrorPeaks=abs((peakMeasQS-peakQS)./peakMeasQS);
relativeErrorLow=abs((lowMeasQS-lowQS)./lowMeasQS);
meanRelErrPeaks=mean(relativeErrorPeaks);
meanRelErrLow=mean(relativeErrorLow);
meanRelErr=(meanRelErrPeaks+meanRelErrLow)/2;
meanRelErrinPercent=meanRelErr*100;

% Plot of the relative error
figure(2)
r=plot(lowtimesQS,relativeErrorLow*100,'o','color','k');
hold on
s=plot(peaktimesQS,relativeErrorPeaks*100,'o','color',myblue);
grid on
r.MarkerSize = 3;
r.MarkerFaceColor='k';
```

```
s.MarkerSize = 3;
s.MarkerFaceColor=myblue;
xlabel('Time [s]')
ylabel('Relative error Q-S [%]')
legend('Local minima','Local maxima','location','southeast')


% Plot of the head loss in the quasi-steady model
hLvec=hfvec+hmvec;
figure(3)
plot(t,abs(hLvec),t,abs(hfvec),t,abs(hmvec))
grid on
legend('h_L','h_f','h_m')
xlabel('Time [s]')
ylabel('Head loss [mWC]')
xlim([0 100])
ylim([0 0.05])

figure(4)
plot(t,abs(hfvec),t,abs(hmvec))
grid on
legend('h_f','h_m')
xlabel('Time [s]')
ylabel('Head loss [mWC]')
xlim([100 150])


%% Vitkovsky's friction model
Z=0; % Initial water fluctuation [m]
Q=-0.007; % Initial flow rate
dQ=0.007; % Initial change in flow rate

Zvec=zeros(1,tmax/dt); % Vector for storing the different Z values
fvec=Zvec;
counter=1;

```

```
for t=0:dt:tmax
    Re=abs(Q)/A*D/nu; % Updating the Reynolds number

    if Re<2300
        f=64/Re; % Laminar friction factor
        C=0.00476; % Vardy's shear decay coefficient C for laminar flow
    else
        f =1/(1.8*log10(6.9/Re+(epsilon*D/3.7)^1.11))^2; % Turbulent friction
            factor given by Haaland's relation
        C=7.41/Re^(log(14.3/Re^0.05)); % Vardy's shear decay coefficent C for
            turbulent flow
    end
    k=sqrt(C)/2; % k coefficient
    V=Q/A;
    dV=dQ/A;
    fVit=k*D/(V*abs(V))*abs(dV/dt)*sign(V);
    fvec(counter)=fVit;

    Kl=3.5; % Minor loss coefficient

    hL=(f*L/D+fVit*L/D+Kl)*abs(Q)*Q/(2*g*A^2); % Total loss

    dQ=dt*g*A/L*(Z-hL); %Change in flow rate
    Q=Q+dQ; % Updating the flow rate

    Z=Z-dt*Q/A; % Updating the water level
    Zvec(counter)=Z; % Storing the new water level in the vector Zvec

    counter=counter+1; % Updating the iteration counter
end


% Plot
t=0:dt:tmax; % Creating the time vector for plotting
Zvec=Zvec+mean(CaveragePT3); % Adding a constant so the model oscillates
    around the same point as the measurements
```

```
figure(5)
plot(t,Zvec,'color',myred)
hold on
plot(timeavgC1,CaveragePT3,'color',myblue)
grid on
legend('RLCT-Vit.','Measurement')
xlabel('Time [s]')
ylabel('Pressure [mWC]')
xlim([0 500])

% Difference calculations
% Preallocation
peakVit=zeros(1,54);
lowVit=zeros(1,54);
peakMeasVit=zeros(1,54);
lowMeasVit=zeros(1,54);
peaktimesVit=zeros(1,54);
lowtimesVit=zeros(1,54);

Zvecinterp=interp1(t,Zvec,timeavgC1); % Interpolates Zvec so it can be compared in the same points as CaveragePT3
count=1;
i=1;
while count<length(CaveragePT3)-round(10*TM)
[peakVit(i),indexpeakVit]=max(Zvecinterp(count:count+round(10*TM))); % 10*TM to get peak, since in CaveragePT3 there is 0.1 s between each point
[lowVit(i),indexlowVit]=min(Zvecinterp(count:count+round(10*TM)));
[peakMeasVit(i),indexMeaspeak]=max(CaveragePT3(count:count+round(10*TM)));
[lowMeasVit(i),indexMeaslow]=min(CaveragePT3(count:count+round(10*TM)));
peaktimesVit(i)=timeavgC1(indexpeakVit+count);
lowtimesVit(i)=timeavgC1(indexlowVit+count);
count=count+round(10*TM);
i=i+1;
end

```

```
% Removing the first peak
peakVit=peakVit(2:length(peakVit));
peakMeasVit=peakMeasVit(2:length(peakMeasVit));
peaktimesVit=peaktimesVit(2:length(peaktimesVit));

differencePeakVit=abs(peakVit-peakMeasVit);
differenceLowVit=abs(lowVit-lowMeasVit);

meandiffVitpeak=mean(differencePeakVit);%Mean of the difference in peaks btw the model and measurements
meandiffVitmin=mean(differenceLowVit); %Mean of the differences in minimas btw the model and measurements
meandiffVit=(meandiffVitpeak+meandiffVitmin)/2; % The average absolute difference between experimental results and simulations in each peak
maxdiffVitpeak=max(differencePeakVit); % The maximum absolute difference among the maxima
maxdiffVitlow=max(differenceLowVit); % The maximum absolute difference among the minima

% Finding the relative error
relativeErrorPeaksVit=abs((peakMeasVit-peakVit)./peakMeasVit);
relativeErrorLowVit=abs((lowMeasVit-lowVit)./lowMeasVit);
meanRelErrPeaksVit=mean(relativeErrorPeaksVit);
meanRelErrLowVit=mean(relativeErrorLowVit);
meanRelErrVit=(meanRelErrPeaksVit+meanRelErrLowVit)/2;
meanRelErrinPercentVit=meanRelErrVit*100;

% Plot of the relative error
figure(6)
r=plot(lowtimesVit,relativeErrorLowVit*100,'o','color','k');
hold on
s=plot(peaktimesVit,relativeErrorPeaksVit*100,'o','color',myblue);
grid on
r.MarkerSize = 3;
r.MarkerFaceColor='k';
s.MarkerSize = 3;
```

```
s.MarkerFaceColor=myblue;
xlabel('Time [s]')
ylabel('Relative error Vitkovsky [%]')
legend('Local minima','Local maxima','location','southeast')

%% One-term friction model
%Finding the B coefficient
D1=D; % Diameter in first section
Q=0.007; % Flow rate [m^3/s]
A1=pi*D1^2/4; % Area [m^2]
V1=Q/A1; % Velocity [m^2/s]

D2=0.325; % Arbitrarily chosen value of diameter in second section
A2=pi*D2^2/4; % Area [m^2]
V2=Q/A2; % Velocity [m^2/s]

Re1=rho*V1*D1/mu; % Reynolds number
Re2=rho*V2*D2/mu; % Reynolds number

f1 =1/(1.8*log10(6.9/Re1+(epsilon*D1/3.7)^1.11))^2; % Steady state friction factor
f2 =1/(1.8*log10(6.9/Re2+(epsilon*D2/3.7)^1.11))^2; % Steady state friction factor

dx=1;

B=(f2/f1*(D1/D2)^5)^(1/((g)*V1*(V2-V1)/dx)); % Correction coefficient

k_loss = 3.5; % Minor loss coefficient

Z=0; % Initial water fluctuation
Q=-0.007; % Initial flow rate
dQ=0.007; % Initial change in flow rate

dt=0.01;
tmax=600;
```

```
Zvec=zeros(1,tmax/dt); % Vector for storing the water level
Bvec=Zvec; % Vector for monitoring the Bterm
expvec=Zvec; % Vector for monitoring the exponent

counter=1;

for t=0:dt:tmax

    Re=abs(Q)/A*D/nu; % Updating the Reynolds number

    if Re<2300
        f = 64/Re; % Laminar friction factor
    else
        f =1/(1.8*log10(6.9/Re+(epsilon*D/3.7)^1.11))^2; % Turbulent friction factor
    end

    dV=dQ/A; % Change in velocity
    hf_f = B^(dV/g)*f*L/D*Q*abs(Q)/(2*g*A^2); %Friction loss
    hf_m = k_loss*Q*abs(Q)/(2*g*A^2); % Minor loss

    hf_loss = hf_f + hf_m; % Total head loss

    dQ = dt*g*A/L*(Z-hf_loss); % Flow change in the U-tube
    Q = Q + dQ; % Updating the flow rate

    Z=Z-dt*Q/A; % Updating the water level

    Zvec(counter)=Z;
    Bvec(counter)=B^abs(dV);
    expvec(counter)=abs(dV);
    counter=counter+1;

end
```

```
% Plot
t=0:dt:tmax; % Creating the time vector for plotting
Zvec=Zvec+mean(CaveragePT3); % Adding a constant so the model oscillates around the same point as the measurements

figure(7)
plot(t,Zvec,'color',myred)
hold on
plot(timeavgC1,CaveragePT3,'color',myblue)
grid
legend('RLCT-OT','Measurement')
xlabel ('Time [s]')
ylabel ('Pressure [mWC]')
xlim([0 500])

meanBvec=mean(Bvec);
meanexpvec=mean(expvec);

% Difference calculations
% Preallocation
peakOT=zeros(1,54);
lowOT=zeros(1,54);
peakMeasOT=zeros(1,54);
lowMeasOT=zeros(1,54);
peaktimesOT=zeros(1,54);
lowtimesOT=zeros(1,54);
lowMeastime=zeros(1,54);

Zvecinterp=interp1(t,Zvec,timeavgC1); % Interpolates Zvec so it can be compared in the same points as CaveragePT3
count=1;
i=1;
while count<length(CaveragePT3)-round(10*TM)
[peakOT(i),indexpeakOT]=max(Zvecinterp(count:count+round(10*TM))); % 10*TM to get index, since in CaveragePT3 there is 0.1 s between each point
[lowOT(i),indexlowOT]=min(Zvecinterp(count:count+round(10*TM)));
```

```
[peakMeasOT(i),indexMEASpeak]=max(CaveragePT3(count:count+round(10*TM)));
[lowMeasOT(i),indexMEASlow]=min(CaveragePT3(count:count+round(10*TM)));
peaktimesOT(i)=timeavgC1(indexpeakOT+count);
lowtimesOT(i)=timeavgC1(indexlowOT+count); % time of the mins in the QS model
lowMeastime(i)=timeavgC1(indexMEASlow+count);
count=count+round(10*TM);
i=i+1;
end


% Removing the first peak
peakOT=peakOT(2:length(peakOT));
peakMeasOT=peakMeasOT(2:length(peakMeasOT));
peaktimesOT=peaktimesOT(2:length(peaktimesOT));

differencePeakOT=abs(peakOT-peakMeasOT);
differenceLowOT=abs(lowOT-lowMeasOT);


meandiffOTpeak=mean(differencePeakOT);%Mean of the difference in peaks btw the model and measurements
meandiffOTmin=mean(differenceLowOT);%Mean of the difference in minimums btw the model and measurements
meandiffOT=(meandiffOTpeak+meandiffOTmin)/2; % The average absolute difference between experimental results and simulations in each peak
maxdiffOTpeak=max(differencePeakOT); % The maximum absolute difference among the maxima
maxdiffOTlow=max(differenceLowOT); % The maximum absolute difference among the minima
mindiffOTpeak=min(differencePeakOT);
mindiffOTlow=min(differenceLowOT);

% Finding the relative error
relativeErrorPeaksOT=abs((peakMeasOT-peakOT)./peakMeasOT);
relativeErrorLowOT=abs((lowMeasOT-lowOT)./lowMeasOT);
meanRelErrPeaksOT=mean(relativeErrorPeaksOT);
```

```
meanRelErrLowOT=mean(relativeErrorLowOT);
meanRelErrOT=(meanRelErrPeaksOT+meanRelErrLowOT)/2;
meanRelErrinPercentOT=meanRelErrOT*100; % Mean relative error in %

% Plot of the relative error
figure(8)
r=plot(lowtimesOT,relativeErrorLowOT*100,'o','color','k');
hold on
s=plot(peaktimesOT,relativeErrorPeaksOT*100,'o','color',myblue);
grid on
r.MarkerSize = 3;
r.MarkerFaceColor='k';
s.MarkerSize = 3;
s.MarkerFaceColor=myblue;
xlabel('Time [s]')
ylabel('Relative error O-T [%]')
legend('Local minima','Local maxima','location','southeast')
```

J Risk assessment

The risk assessment for the master thesis is included in the following pages. The risk assessment report for the work in the experimental rig is also included.

There were no incidents severely affecting the health or environment related to the experiments. However, the shaft on one of the butterfly valves broke off during one of the experiments. This was solved by instead using a wrench to open and close the valve in the subsequent experiments.

NTNU	Hazardous activity identification process	Prepared by	Number	Date
		HSE section	HMSRV2601E	09.01.2013
HSE		Approved by		Replaces
		The Rector		01.12.2006

Unit: *Department of Energy and Prosess engineering* **Date:** **17.01.2019**

Line manager: Terese Løvås

Participants in the identification process (including their function)**:**

Short description of the main activity/main process: Master project for student Kathrine Albjerk Hamran. Simulations and measurements of friction in oscillating flow.

Is the project work purely theoretical? (YES/NO): NO *Answer "YES" implies that supervisor is assured that no activities requiring risk assessment are involved in the work. If YES, briefly describe the activities below. The risk assessment form need not be filled out.*

Signatures: *Responsible supervisor: Pål-Tore Selbo Storli* *Student: Kathrine Albjerk Hamran*

ID nr.	Activity/process	Responsible person	Existing documentation	Existing safety measures	Laws, regulations etc.	Comment
01	Operating a dynamic test rig for water flow in a pipe system. Pressure, velocity and flow measurements.	Kathrine Albjerk Hamran	- Risk assessment for project work in fall 2018		HMS course	

NTNU	Risk assessment	Prepared by	Number	Date
		HSE section	HMSRV2603E	04.02.2011
HSE/KS		Approved by		Replaces
		The Rector		01.12.2006

Unit: *Department of Energy and Prosess engineering* **Date:** 17.01.19

Line manager: Terese Løvås

Participants in the identification process (including their function)**:** Kathrine Albjerk Hamran, student.

Short description of the main activity/main process: Master project for student Kathrine Albjerk Hamran. Project title: Simulations and measurements of friction in oscillating flow.

Signatures: *Responsible supervisor: Pål-Tore Storli* *Student: Kathrine Albjerk Hamran*

Activity from the identification process form	**Potential undesirable incident/strain**	**Likelihood:**	**Consequence:**			**Risk Value (human)**	**Comments/status Suggested measures**
		Likelihood (1-5)	Human (A-E)	Environment (A-E)	Economy/ material (A-E)		
Work on higher plan (above normal ground, 2. floor or higher)	- Fall injuries - Dropping items that can injure personnel around and the item itself	3	C	A	B	C3	- Stand on a safety ground - Use safety equipment if necessary
Water leakage from the pipe system	- Slippery floor - Water stream at high pressure	3	C	B	C	C3	- Protect eyes with glasses - Beware of slippery floor
Other work in the laboratory	- High noise - Falling items hitting personnel	4	C	A	B	C4	- Beware of other projects and work in the laboratory - Always use safety and protection gear to protect ears and eyes - Consider using helmets and other protection gear such as protected shoes and protection/work clothes

Likelihood, e.g.:
1. *Minimal*
2. *Low*
3. *Medium*
4. *High*
5. *Very high*

Consequence, e.g.:
A. *Safe*
B. *Relatively safe*
C. *Dangerous*
D. *Critical*
E. *Very critical*

Risk value (each one to be estimated separately):
Human = Likelihood x Human Consequence
Environmental = Likelihood x Environmental consequence
Financial/material = Likelihood x Consequence for Economy/materiel

Potential undesirable incident/strain

Identify possible incidents and conditions that may lead to situations that pose a hazard to people, the environment and any materiel/equipment involved.

Criteria for the assessment of likelihood and consequence in relation to fieldwork

Each activity is assessed according to a worst-case scenario. Likelihood and consequence are to be assessed separately for each potential undesirable incident. Before starting on the quantification, the participants should agree what they understand by the assessment criteria:

Likelihood

Minimal 1	Low 2	Medium 3	High 4	Very high 5
Once every 50 years or less	Once every 10 years or less	Once a year or less	Once a month or less	Once a week

Consequence

Grading	Human	Environment	Financial/material
E Very critical	May produce fatality/ies	Very prolonged, non-reversible damage	Shutdown of work >1 year.
D Critical	Permanent injury, may produce serious serious health damage/sickness	Prolonged damage. Long recovery time.	Shutdown of work 0.5-1 year.
C Dangerous	Serious personal injury	Minor damage. Long recovery time	Shutdown of work < 1 month
B Relatively safe	Injury that requires medical treatment	Minor damage. Short recovery time	Shutdown of work < 1week
A Safe	Injury that requires first aid	Insignificant damage. Short recovery time	Shutdown of work < 1day

The unit makes its own decision as to whether opting to fill in or not consequences for economy/materiel, for example if the unit is going to use particularly valuable equipment. It is up to the individual unit to choose the assessment criteria for this column.

Risk = Likelihood x Consequence
Please calculate the risk value for “Human”, “Environment” and, if chosen, “Economy/materiel”, separately.

About the column ”Comments/status, suggested preventative and corrective measures”:
Measures can impact on both likelihood and consequences. Prioritise measures that can prevent the incident from occurring; in other words, likelihood-reducing measures are to be prioritised above greater emergency preparedness, i.e. consequence-reducing measures.

MATRIX FOR RISK ASSESSMENTS at NTNU

CONSEQUENCE	Extremely serious	E1	E2	E3	E4	E5
	Serious	D1	D2	D3	D4	D5
	Moderate	C1	C2	C3	C4	C5
	Minor	B1	B2	B3	B4	B5
	Not significant	A1	A2	A3	A4	A5
		Very low	Low	Medium	High	Very high
		LIKELIHOOD				

Principle for acceptance criteria. Explanation of the colours used in the risk matrix.

Colour		Description
Red		Unacceptable risk. Measures must be taken to reduce the risk.
Yellow		Assessment range. Measures must be considered.
Green		Acceptable risk Measures can be considered based on other considerations.

NTNU

Risikovurderingsrapport

Dynamisk testrigg for oscillerende strømning

Prosjekttittel	Simuleringer og målinger av friksjon i oscillerende strømning
Apparatur	Dynamisk testrigg for oscillerende strømning
Enhet	NTNU
Apparaturansvarlig	Bård Aslak Brandåstrø
Prosjektleder	Pål-Tore Selbo Storli
HMS-koordinator	Morten Grønli
HMS-ansvarlig (linjeleder)	Terese Løvås
Plassering	Vannkraftlaboratoriet
Romnummer	11,21
Risikovurdering utført av	Kathrine Albjerk Hamran

Godkjenning:

Apparatur kort (UNIT CARD) valid for:	**12 måneder**
Forsøk pågår kort (EXPERIMENT IN PROGRESS) valid for:	**12 måneder**

Rolle	Navn	Dato	Signatur
Prosjektleder	Pål-Tore Selbo Storli	22/11 18	
HMS koordinator	Morten Grønli	26/11 18	
HMS ansvarlig (linjeleder)	Terese Løvås	30/11-18	Terese Løvås

INNHOLDSFORTEGNELSE

1 INNLEDNING 1

2 ORGANISERING 1

3 RISIKOSTYRING AV PROSJEKTET 1

4 BESKRIVELSER AV FORSØKSOPPSETT 2

5 EVAKUERING FRA FORSØKSOPPSETNINGEN 3

6 VARSLING 3

6.1 Før forsøkskjøring 3
6.2 Ved uønskede hendelser 3

7 VURDERING AV TEKNISK SIKKERHET 4

7.1 HAZOP 4
7.2 Brannfarlig, reaksjonsfarlig og trykksatt stoff og gass 4
7.3 Trykkpåkjent utstyr 4
7.4 Påvirkning av ytre miljø (utslipp til luft/vann, støy, temperatur, rystelser, lukt) 4
7.5 Stråling 5
7.6 Kjemikalier 5
7.7 El sikkerhet (behov for å avvike fra gjeldende forskrifter og normer) 5

8 VURDERING AV OPERASJONELL SIKKERHET 5

8.1 Prosedyre HAZOP 5
8.2 Forsøksprosedyre og nødstopps prosedyre 5
8.3 Opplæring av operatører 6
8.4 Tekniske modifikasjoner 6
8.5 Personlig verneutstyr 6
8.6 Generell sikkerhet 6
8.7 Sikkerhetsutrustning 6
8.8 Spesielle tiltak 6

9 TALLFESTING AV RESTRISIKO – RISIKOMATRISE 6

10 LOVER FORSKRIFTER OG PÅLEGG SOM GJELDER 8

11 DOKUMENTASJON 8

1 INNLEDNING

Prosjektarbeid for Kathrine Albjerk Hamran. Målinger av trykk og volumstrøm ved massesvingninger i den dynamiske testriggen.

2 ORGANISERING

Rolle	NTNU
Prosjektleder	Pål-Tore Selbo Storli
Apparaturansvarlig	Bård Aslak Brandåstrø
Romansvarlig	Joar Grilstad
HMS koordinator	Morten Grønli
HMS ansvarlig (linjeleder):	Terese Løvås

3 RISIKOSTYRING AV PROSJEKTET

Hovedaktiviteter risikostyring	Nødvendige tiltak, dokumentasjon	DTG
Prosjekt initiering	Prosjekt initiering mal	
Veiledningsmøte	Skjema for Veiledningsmøte med pre-risikovurdering	
Innledende risikovurdering	Fareidentifikasjon – HAZID Skjema grovanalyse	
Vurdering av teknisk sikkerhet	Prosess-HAZOP Tekniske dokumentasjoner	
Vurdering av operasjonell sikkerhet	Prosedyre-HAZOP Opplæringsplan for operatører	
Sluttvurdering, kvalitetssikring	Uavhengig kontroll Utstedelse av apparaturkort Utstedelse av forsøk pågår kort	

4 BESKRIVELSER AV FORSØKSOPPSETT

Illustrasjon vist under. Riggen er knyttet til Pelton-pumpen i Vannkraftlaboratoriet.

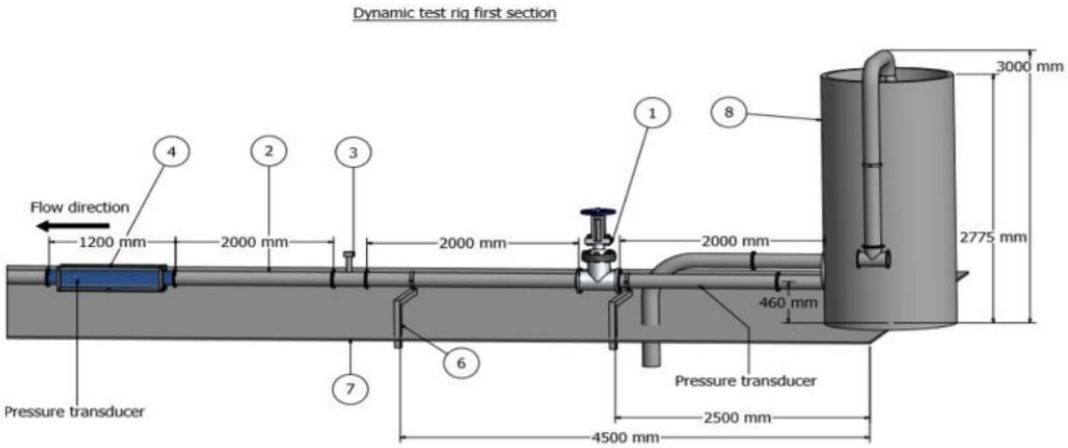

PARTS LIST	
ITEM	PART
1	Gate valve
2	Penstock
3	Electromagnatic flowmeter
4	Test section
5	Surge shaft
6	Support
7	Floor
8	Upper resavoir

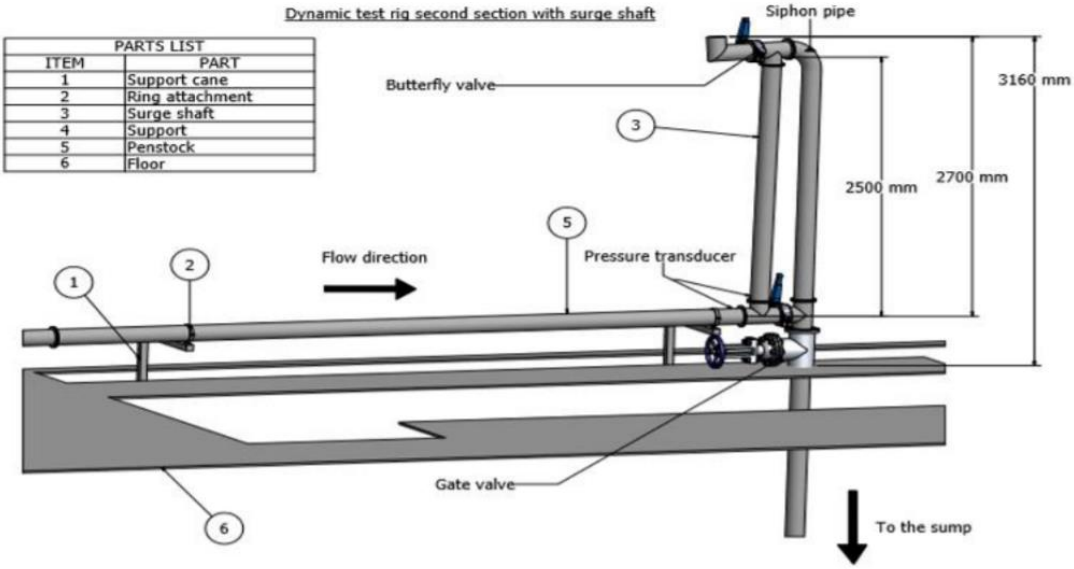

PARTS LIST	
ITEM	PART
1	Support cane
2	Ring attachment
3	Surge shaft
4	Support
5	Penstock
6	Floor

5 EVAKUERING FRA FORSØKSOPPSETNINGEN

Evakuering skjer på signal fra alarmklokker eller lokale gassalarmstasjon med egen lokal varsling med lyd og lys utenfor aktuelle rom, se 6.2.

Evakuering fra rigg området foregår igjennom merkede nødutganger til møteplass, (hjørnet gamle kjemi/kjelhuset eller parkeringsplass 1a-b.)

Aksjon på rigg ved evakuering:
Nødavstenging av pumpen.

6 VARSLING

6.1 Før forsøkskjøring

Varsling per e-post, til **iept-experiments@ivt.ntnu.no**

I e-posten skal det stå:
- Navn på forsøksleder:
- Navn på forsøksrigg:
- Tid for start: (dato og klokkelslett)
- Tid for stop: (dato og klokkelslett)

All forsøkskjøringen skal planlegges og legges inn i aktivitetskalender for lab. Forsøksleder må få bekreftelse på at forsøkene er klarert med øvrig labdrift før forsøk kan iverksettes.

6.2 Ved uønskede hendelser

BRANN
Ved brann en ikke selv er i stand til å slukke med rimelige lokalt tilgjengelige slukkemidler, skal nærmeste brannalarm utløses og arealet evakueres raskest mulig. En skal så være tilgjengelig for brannvesen/bygningsvaktmester for å påvise brannsted.
Om mulig varsles så:

NTNU
Morten Grønli, Mob: 918 97 515
Terese Løvås: Mob: 918 97 007
NTNU – SINTEF Beredskapstelefon

GASSALARM
Ved gassalarm skal gassflasker stenges umiddelbart og området ventileres. Klarer man ikke innen rimelig tid å få ned nivået på gasskonsentrasjonen så utløses brannalarm og laben evakueres. Dedikert personell og eller brannvesen sjekker så lekkasjested for å fastslå om det er mulig å tette lekkasje og lufte ut området på en forsvarlig måte.
Varslingsrekkefølge som i overstående punkt.

PERSONSKADE

- Førstehjelpsutstyr i Brann/førstehjelpsstasjoner,
- Rop på hjelp,
- Start livreddende førstehjelp
- **Ring 113** hvis det er eller det er tvil om det er alvorlig skade.

ANDRE UØNSKEDE HENDELSER (AVVIK)

NTNU:
Rapportering av uønskede hendelser, Innsida, avviksmeldinger
https://innsida.ntnu.no/wiki/-/wiki/Norsk/Melde+avvik

7 VURDERING AV TEKNISK SIKKERHET

7.1 HAZOP

Forsøksoppsetningen deles inn i følgende noder:

Node 1	Rørsystem med pumpe

Vedlegg, skjema: Hazop_mal
Konklusjon: (Sikkerhet ivaretatt)

7.2 Brannfarlig, reaksjonsfarlig og trykksatt stoff og gass

Inneholder forsøkene brannfarlig, reaksjonsfarlig og trykksatt stoff

JA	Trykksatt vann

Vurdering: *Arbeidsmedium er vann. Trykk under 0.25bar gage. Alle rør er levert av eksternt firma.*

7.3 Trykkpåkjent utstyr

Inneholder forsøksoppsetningen trykkpåkjent utstyr?

JA	
NEI	

Vedlegg:
Konklusjon:

7.4 Påvirkning av ytre miljø (utslipp til luft/vann, støy, temperatur, rystelser, lukt)

Vil eksperimentene generere utslipp av røyk, gass, lukt eller unormalt avfall.? Mengder/konsistens. Er det behov for utslippstillatelse, ekstraordinære tiltak?

NEI	x

Konklusjon: Ingen fare.

7.5 Stråling

JA	
NEI	x

Konklusjon: Ingen fare.

7.6 Kjemikalier

Inneholder eksperimentene bruk og behandling av kjemikalier. Hvilke og hvilke mengder? Hvordan skal dette avhendes, oppbevares? Risikovurder i henhold til sikkerhetsdatablad Er det behov for beskyttelses tiltak tillegges disse i operasjonell prosedyre.

JA	
NEI	x

Konklusjon: Ingen fare.

7.7 El sikkerhet (behov for å avvike fra gjeldende forskrifter og normer)

Her forstås montasje og bruk i forhold til normer og forskrifter med tanke på berøringsfare

JA	
NEI	x

Konklusjon: Ikke behov for å avvike fra gjeldende forskrifter og normer.

8 VURDERING AV OPERASJONELL SIKKERHET

Sikrer at etablerte prosedyrer dekker alle identifiserte risikoforhold som må håndteres gjennom operasjonelle barrierer og at operatører og teknisk utførende har tilstrekkelig kompetanse.

8.1 Prosedyre HAZOP

Metoden er en undersøkelse av operasjonsprosedyrer, og identifiserer årsaker og farekilder for operasjonelle problemer.

Vedlegg: HAZOP_MAL_Prosedyre

8.2 Forsøksprosedyre og nødstopps prosedyre

Driftsprosedyren er en sjekkliste som skal fylles ut for hvert forsøk.
Nødstopp prosedyren skal sette forsøksoppsetningen i en harmløs tilstand ved uforutsette hendelser.

Vedlegg: Forsøksprosedyre
Nødstopp prosedyre: Nødavstegning pumpen.

8.3 Opplæring av operatører

Dokument som viser Opplæringsplan for operatører utarbeides for alle forøksrigger.

Vedlegg*:* Opplæringsplan for operatører

8.4 Tekniske modifikasjoner

- *Tekniske modifikasjoner som kan gjøres av Operatør (for eksempel. skifting av komponenter, likt mot likt)*
- *Tekniske modifikasjoner som må gjøres av Teknisk personale: (for eksempel modifikasjon på trykkpåkjent utstyr).*
- *Hvilke tekniske modifikasjoner utløser krav om ny risikovurdering;(ved endring av risikobildet)?*

Konklusjon: Ikke behov for tekniske modifikasjoner.

8.5 Personlig verneutstyr

- *Det er påbudt med vernebriller i sonen anlegget er plassert i.*

8.6 Generell sikkerhet

- *Traverskran og truck kjøring skal ikke foregå i nærheten under eksperimentet.*
- *Gassflasker skal plasseres i godkjent stativ med avstengningsventil lett tilgjengelig.*
- *Vann og trykklufttilførsel i slanger skal stenges/kobles fra ved nærmeste fastpunkt når riggen ikke er i bruk.*

8.7 Sikkerhetsutrustning

- *Portable gassdetektorer skal benyttes under forsøkskjøring*.
- *Fare skilting, se* Forskrift om Sikkerhetsskilting og signalgivning på arbeidsplassen

8.8 Spesielle tiltak

For eksempel:
- *Overvåkning.*
- *Beredskap.*
- *Sikker jobb analyse ved modifikasjoner, (SJA)*
- *Arbeid i høyden*
- *Brannfarlig/giftig gass eller kjemikalier*

9 TALLFESTING AV RESTRISIKO – RISIKOMATRISE

Risikomatrisen vil gi en visualisering og en samlet oversikt over aktivitetens risikoforhold slik at ledelse og brukere får et mest mulig komplett bilde av risikoforhold.

IDnr	Aktivitet-hendelse	Konsekvens	Sannsynlighet	RV
1	*Rørbrudd*	A	1	A1
2	*Fremmedlegemer i vannet*	A	1	A1
3	*Pumpen bryter sammen*	A	1	A1

Vurdering restrisiko: *Det er liten restrisiko ved forsøket. Fremmedlegemer i vannet gir liten risiko for personskade. Trykksatt vann fordrer bruk av vernebriller.*

RISIKOMATRISE

KONSEKVENS	(E) Svært alvorlig	**E1**	**E2**	**E3**	**E4**	**E5**
	(D) Alvorlig	**D1**	**D2**	**D3**	**D4**	**D5**
	(C) Moderat	**C1**	**C2**	**C3**	**C4**	**C5**
	(B) Liten	**B1**	**B2**	**B3**	**B4**	**B5**
	(A) Ubetydelig	**A1**	**A2**	**A3**	**A4**	**A5**
		(1) Veldig lav	(2) Lav	(3) Middels	(4) Stor	(5) Svært Stor
		SANSYNLIGHET				

Prinsipp over akseptkriterium. Forklaring av fargene som er brukt i risikomatrisen.

Farge		Beskrivelse
Rød		Uakseptabel risiko. Tiltak skal gjennomføres for å redusere risikoen.
Gul		Vurderingsområde. Tiltak skal vurderes.
Grønn		Akseptabel risiko. Tiltak kan vurderes ut fra andre hensyn.

10 LOVER FORSKRIFTER OG PÅLEGG SOM GJELDER

Se http://www.arbeidstilsynet.no/regelverk/index.html

- Lov om tilsyn med elektriske anlegg og elektrisk utstyr (1929)
- Arbeidsmiljøloven
- Forskrift om systematisk helse-, miljø- og sikkerhetsarbeid (HMS Internkontrollforskrift)
- Forskrift om sikkerhet ved arbeid og drift av elektriske anlegg (FSE 2006)
- Forskrift om elektriske forsyningsanlegg (FEF 2006)
- Forskrift om utstyr og sikkerhetssystem til bruk i eksplosjonsfarlig område NEK 420
- Forskrift om håndtering av brannfarlig, reaksjonsfarlig og trykksatt stoff samt utstyr og anlegg som benyttes ved håndteringen
- Forskrift om Håndtering av eksplosjonsfarlig stoff
- Forskrift om bruk av arbeidsutstyr.
- Forskrift om Arbeidsplasser og arbeidslokaler
- Forskrift om Bruk av personlig verneutstyr på arbeidsplassen
- Forskrift om Helse og sikkerhet i eksplosjonsfarlige atmosfærer
- Forskrift om Høytrykksspyling
- Forskrift om Maskiner
- Forskrift om Sikkerhetsskilting og signalgivning på arbeidsplassen
- Forskrift om Stillaser, stiger og arbeid på tak m.m.
- Forskrift om Sveising, termisk skjæring, termisk sprøyting, kullbuemeisling, lodding og sliping (varmt arbeid)
- Forskrift om Tekniske innretninger
- Forskrift om Tungt og ensformig arbeid
- Forskrift om Vern mot eksponering for kjemikalier på arbeidsplassen (Kjemikalieforskriften)
- Forskrift om Vern mot kunstig optisk stråling på arbeidsplassen
- Forskrift om Vern mot mekaniske vibrasjoner
- Forskrift om Vern mot støy på arbeidsplassen

Veiledninger fra arbeidstilsynet
se: http://www.arbeidstilsynet.no/regelverk/veiledninger.html

11 DOKUMENTASJON

- Tegninger, foto, beskrivelser av forsøksoppsetningen
- Hazop_mal
- Sertifikat for trykkpåkjent utstyr
- Håndtering avfall i NTNU
- Sikker bruk av LASERE, retningslinje
- HAZOP_MAL_Prosedyre
- Forsøksprosedyre
- Opplæringsplan for operatører
- Skjema for sikker jobb analyse, (SJA)
- Apparaturkortet
- Forsøk pågår kort

NTNU

Vedlegg til Risikovurderingsrapport

Dynamic test rig

Prosjekttittel	Simulations and measurements of friction in oscillating flow
Apparatur	Dynamic test rig for oscillatory flow
Enhet	NTNU
Apparaturansvarlig	Bård Aslak Brandåstrø
Prosjektleder	Pål-Tore Selbo Storli
HMS-koordinator	Morten Grønli
HMS-ansvarlig (linjeleder)	Terese Løvås
Plassering	Vannkraftlaboratoriet
Romnummer	11,21
Risikovurdering utført av	Kathrine Albjerk Hamran

INNHOLDSFORTEGNELSE

VEDLEGG A: PROSESS OG INSTRUMENTERINGSDIAGRAM 1

VEDLEGG B: FORSØKSPROSEDYRE 3

VEDLEGG C: OPPLÆRINGSPLAN FOR OPPERATØRER 5

APPARATURKORT / UNITCARD 6

FORSØK PÅGÅR /EXPERIMENT IN PROGRESS 7

NTNU

VEDLEGG A: PROSESS OG INSTRUMENTERINGSDIAGRAM

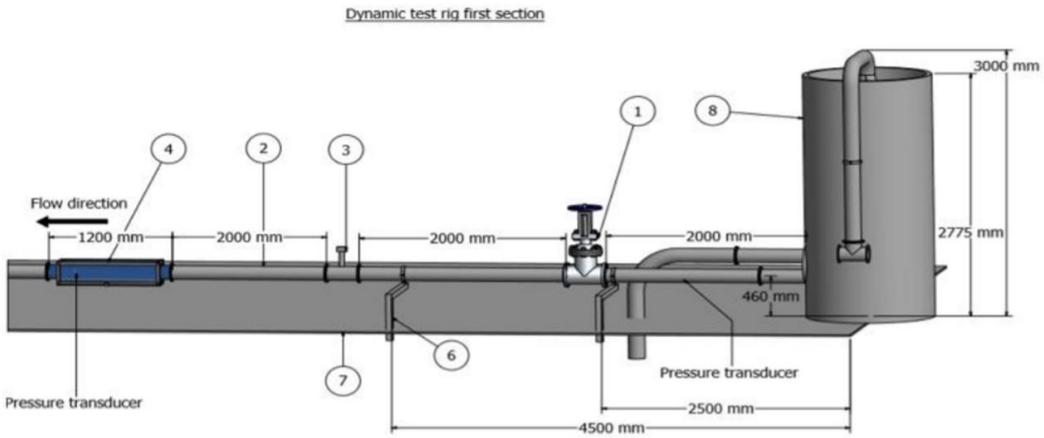

PARTS LIST	
ITEM	PART
1	Gate valve
2	Penstock
3	Electromagnatic flowmeter
4	Test section
5	Surge shaft
6	Support
7	Floor
8	Upper resavoir

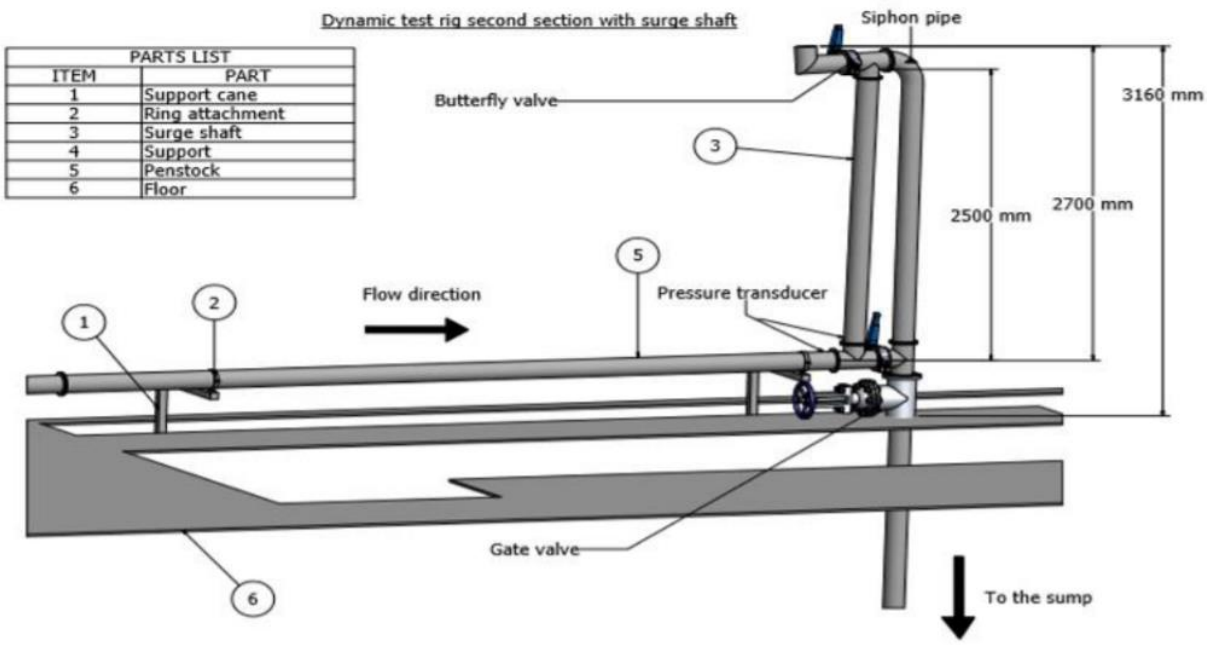

PARTS LIST	
ITEM	PART
1	Support cane
2	Ring attachment
3	Surge shaft
4	Support
5	Penstock
6	Floor

VEDLEGG B: FORSØKSPROSEDYRE

Prosjekt Målinger av friksjon i oscillerende strømning		
Apparatur Dynamisk testrigg for oscillerende strømning	**Dato**	**Signatur**
Prosjektleder Pål-Tore Selbo Storli	27/4 18	

	Conditions for the experiment:	**Completed**
	Experiments should be run in normal working hours, 08:00-16:00 during winter time and 08.00-15.00 during summer time. Experiments outside normal working hours shall be approved.	✓
	One person must always be present while running experiments, and should be approved as an experimental leader.	✓
	An early warning is given according to the lab rules, and accepted by authorized personnel.	✓
	Be sure that everyone taking part of the experiment is wearing the necessary protecting equipment and is aware of the shut down procedure and escape routes.	✓
	Preparations	**Carried out**
	Post the "Experiment in progress" sign.	✓
	Start up procedure: - *Make sure the draft tube is filled with water, by opening the valve by the pump until water drips from the tube, and then close the valve again.* - *Check that all the valves connected to the pipe system are in the right position, before starting the pump.* - *After starting the pump, make sure to ramp up slowly from 100 rpm to the desired rpm.*	✓
	During the experiment	✓
	- *Check on the pump from time to time, to make sure nothing is wrong with it.*	✓
	End of experiment	
	Shut down procedure: - *Ramp the pump down to 100 rpm in several steps, before turning off the pump.* - *Empty the pipe system of water.*	✓
	Remove all obstructions/barriers/signs around the experiment.	✓
	Tidy up and return all tools and equipment.	✓
	Tidy and cleanup work areas.	✓
	Return equipment and systems back to their normal operation settings (fire alarm)	✓
	To reflect on before the next experiment and experience useful for others	
	Was the experiment completed as planned and on scheduled in professional terms?	✓

	Was the competence which was needed for security and completion of the experiment available to you?	✓
	Do you have any information/ knowledge from the experiment that you should document and share with fellow colleagues?	

Operatører:

Navn	Dato	Signatur
Kathrine Albjerk Hamran	22/11-2018	Kathrine Albjerk Hamran

VEDLEGG C: OPPLÆRINGSPLAN FOR OPPERATØRER

Prosjekt Målinger av friksjon i oscillerende strømning		
Apparatur Dynamisk testrigg for oscillerende strømning	**Dato**	**Signatur**
Prosjektleder Pål-Tore Selbo Storli	22/11 18	

	Kjennskap til EPT LAB generelt	
	Lab • adgang • rutiner/regler • arbeidstid	✓
	Kjenner til evakueringsprosedyrer	✓
	Aktivitetskalender	✓
	Innmelding av forsøk til: iept-experiments@ivt.ntnu.no	
	Kjennskap til forsøkene	
	Prosedyrer for forsøkene	✓
	Nødstopp	✓
	Nærmeste brann/førstehjelpsstasjon	✓

Jeg erklærer herved at jeg har gjennomgått og forstått HMS-regelverket, har fått hensiktsmessig opplæring for å kjøre dette eksperimentet og er klar over mitt personlige ansvar ved å arbeide i EPT laboratorier.

Operatører

Navn	Dato	Signatur
Kathrine Albjerk Hamran	22/11-2018	Kathrine Albjerk Hamran

APPARATURKORT

Enhet (unit) og bygg/romnr. (building/room no.):

NTNU-E	324	11	1. etg

Laboratorium

Dette kortet SKAL henges godt synlig ved maskinen!
This card MUST be posted on a visible place on the unit!

Apparatur (Unit) **Dynamisk Testrigg**	**Dato Godkjent (Date Approved)** torsdag 22. november 2018
Prosjektleder (Project Leader) Pål Tore Selbo Storli	**Telefon mobil/privat (Phone no. mobile/private)** 97782146
Apparaturansvarlig (Unit Responsible) Bård Aslak Brandåstrø	**Telefon mobil/privat (Phone no. mobile/private)** 91897257
Sikkerhetsrisikoer (Safety hazards) - Pump breakdown - Pipe system failure	
Sikkerhetsregler (Safety rules) Wear appropriate safety goggles	
Nødstopp prosedyre (Emergency shutdown) Turn off the pump if something is unusual (leakage, smoke from pump, etc)	
Her finner du (Here you will find): **Prosedyrer (Procedures)** **Bruksanvisning (User manual)**	 Ved rigg Ved rigg
Brannslukningsapparat (Fire extinguisher) **Førsthjelpsskap (First aid cabinet)**	1. etasje v/trapp 1. etasje v/trapp

NTNU
Institutt for energi og prosessteknikk

Dato 30/11-18

Signert Terese Lovin

NTNU SINTEF

FORSØK PÅGÅR

Enhet (unit) og bygg/romnr. (building/room no.):

NTNU-E	324	11	1. etg

Laboratorium

Dette kortet SKAL henges opp før forsøk kan starte!
This card MUST be posted on the unit before the experiment startup!

Apparatur (Unit) **Dynamisk Testrigg**	**Dato godkjent (Date Approved)** torsdag 22. november 2018
Prosjektleder (Project Leader) Pål Tore Selbo Storli	**Telefon mobil/privat (Phone no. mobile/private)** 97782146
Apparaturansvarlig (Unit Responsible) Bård Aslak Brandåstrø	**Telefon mobil/privat (Phone no. mobile/private)** 91897257

Godkjente operatører (Approved Operators)

Navn/Name	Telefon/Phone	Mobil
Albjerk Hamran, Kathrine		
Storli, Pål Tore Selbo	735 92518	97782146

Prosjekt (Project)

Measurements of friction in oscillating flow

Forsøkstid / Experimental time (start - stop)

22.11.2018 - 22.11.2019

Kort beskrivelse av forsøket og relaterte farer (Short description of the experiment and related hazards)

Pressure measurements with static pressure transducers and flow measurements with an electromagnetic flowmeter. Transient dynamics are generated by rapidly closing a valve downstream. Pressure and flow parameters will change in an oscillatory behavior. This change can in worst-case cause pipe failure or system breakdown, which can make parts fall down. This can be a direct danger for people standing close to the rig. It is important to have control on the pump, in case of breakdown (mechanical damage or fire). In addition, water leakage is possible with failure, causing danger to electrical equipment, etc.

NTNU

Institutt for energi og prosessteknikk

Dato 30/11-18

Signert Jørgen Løvås

NTNU SINTEF

K Article for the CRHT-IX conference

The following paper was written by the author for the *9th International symposium on Current Research in Hydropower Technologies* (CRHT-IX) at Kathmandu University in Nepal. The paper presents parts of the project work done by the author in the fall of 2018, and was also presented at the conference.

Simulations and measurements of friction in oscillating flow

K A Hamran

Department of Energy and Process Engineering, Norwegian University of Science and Technology, Trondheim, Norway

E-mail: kathriah@stud.ntnu.no

Abstract. Rapid changes in the operating point of a hydropower plant cause transients in the hydraulic system. The flow will oscillate between the surge shaft and the reservoir until the oscillations are damped out by the friction. This paper investigates different friction models for oscillating flow, such as a quasi-steady model, Vítkovský's model, and a one-term model. The governing equations for transient flow were solved by using rigid water column theory. The simulations were compared with experimental results from a small-scale test rig. The test rig consisted of a small reservoir, a horizontal pipe, and a surge shaft. The oscillations were induced by closing a valve downstream of the surge shaft. Measurements were obtained with pressure transducers.

1. Introduction

Changes in the operating point of a hydropower plant induce transients in the hydraulic system. Transients are often split into fast transients such as the water hammer and slow transients such as mass oscillations [1]. The friction in such transitional, unsteady flow is different than the friction in steady flow [2]. But few models are able to accurately account for the friction loss in transient flow, while at the same time being computationally efficient and easy to use. This paper investigates a few different friction models for the slow transient mass oscillations and compares them with experimental results.

Fluid transients have been studied since the 17th century [2]. But the equations governing transient flow were not fully established until the 1960s [3].

For slow transients, the governing equations are often simplified. Rigid water column theory in which the pipe walls are considered rigid and the water is considered incompressible, is often used for mass oscillations since it is simpler than taking the elasticity into account and still captures the physics quite well [4].

Conventionally, the friction relations for steady flow have been expected to hold at every instant in time in transient flow analysis [3]. The expression for the head loss in steady flow was proposed by Weisbach in 1850 and is well-known today as the Darcy-Weisbach equation [5]. The head loss is caused by viscosity, and is related to the wall shear stress [6]. A quasi-steady approach is sometimes used, in which the steady friction relation is updated at each instant in time. However, the Darcy-Weisbach head loss relation is usually not satisfactory for transient flow, since flow reversal will occur in transient flow and due to the no-slip condition at the pipe wall, this will yield larger wall shear stresses than in steady flow [3]. Indeed, research has

shown that using steady or quasi-steady relations results in discrepancies between experimental and numerical results [3]. An unsteady component is therefore often included in the friction expression for transient flow.

Daily et al. [7] found that accelerating flow had a slight increase in frictional resistance compared with steady flow, while decelerating flow had a slightly smaller frictional resistance. They argued that this was because during acceleration the velocity profile steepens and gives higher shear. They developed an expression for the unsteady friction, in which it depends on the instantaneous mean velocity, V, and the instantaneous local acceleration, $\partial V/\partial t$.

Brunone modified the model proposed by Daily et al. and included the instantaneous convective acceleration, $\partial V/\partial x$ [8].

Vítkovský introduced a sign term and an absolute value around the instantaneous convective acceleration in Brunone's formulation of the friction model in order to ensure that the convective term has the correct sign for all cases [8]. Since his investigations had shown that the original formulation gave the wrong sign of the convective term, $-a\partial V/\partial x$ for some cases, such as closure of upstream valve where initial flow in the pipe is in positive x-direction [8]. Bergant et al. [8] showed that Vítkovský's model gave a better fit than the quasi-steady model when compared with measurements of an upstream valve closure when looking at the first second following the valve closure. Even though Brunone's friction model was developed for the fast transient water hammer, it is expected to perform well for mass oscillations as well, since many of the flow characteristics which occurs in water hammer flow such as flow reversal, also occurs in mass oscillations.

Bergset [9] proposed a new one-term model which builds on the quasi-steady friction model. In order to correct the quasi-steady friction model, he proposed to multiply the friction term by a constant which had the nondimensionalized convective acceleration and instantaneous local acceleration terms in the exponent.

2. Theory

2.1. Governing equations

The equations governing transient flow in pipes with circular cross-section can be derived from conservation of mass and continuity as shown in for example [10]. The resulting continuity and momentum equation for transient flow, expressed in terms of the piezometric head, H, are equation (1) and equation (2), respectively.

$$\frac{\partial H}{\partial t} + \frac{a^2}{g}\frac{\partial V}{\partial x} = 0 \tag{1}$$

$$\frac{\partial H}{\partial x} + \frac{1}{g}\frac{\partial V}{\partial t} + h_f = 0 \tag{2}$$

These equations are valid for slightly compressible fluids flowing at low Mach numbers. H is as mentioned the piezometric head, a is the speed of sound, g is the gravitational acceleration, V is the fluid velocity, and h_f is the head loss per unit length. For transient flow, the head loss is often split into a steady and unsteady part, $h_f = h_{f,s} + f_{h,u}$. The speed of sound, a, for a thick-walled or rigid pipe is $a = \sqrt{K/\rho}$ where K is the bulk modulus of elasticity of the fluid, and ρ is the density of the fluid [10].

2.2. Methods of Solutions

The partial differential equations governing transient flow, equation (1) and (2), can be solved by different numerical methods. The method of characteristics is the most common method used when investigating water hammers [10]. For slow transients, such as mass oscillations, it is common to solve the equations using rigid liquid column theory. Under the assumption

that mass oscillations act as a rigid liquid column, the partial differential equations reduce to a set of ordinary differential equations. With rigid liquid column theory, the fluid is considered incompressible, and the pipe walls are considered rigid. This implies an infinite speed of sound [10]. Consequently, at any point in the system, a flow change is transmitted instantaneously throughout the system, and the water will have a common fluid particle velocity along the pipe [2]. With the assumptions above, the partial differential equations reduce to ordinary differential equations since the flow variables do not vary with distance, only with time [2]. The continuity equation becomes

$$Q = -A\frac{dz}{dt} \tag{3}$$

and the momentum equation is reduced to

$$\frac{L}{gA}\frac{dQ}{dt} = z - kQ|Q| \tag{4}$$

where $k = f\frac{L}{2gA^2D}$ with L being the length of the pipe. A is the cross sectional area of the pipe, Q is the flow rate, and z is the height of the free surface in the surge shaft. Equations (1) and (2) are thus reduced to an initial value problem consisting of two ordinary differential equations, equation (3) and (4) with two unknowns, z and Q, and two known initial values, z_0 and Q_0. Solutions of this can be found by different numerical methods, such as the Euler method, a modified Euler method or a Runge-Kutta method. In this paper, the Euler method was chosen. For equation (3) and equation (4), the Euler method yields

$$Q_{n+1} = Q_n + \Delta t \cdot f(Q_n) \tag{5}$$

with $f(Q_n) = \frac{gA}{L}(z - kQ_n|Q_n|)$, and

$$z_{n+1} = z_n - \Delta t \cdot \frac{Q_n}{A} \tag{6}$$

This method is first-order accurate in time, meaning that the error is of order Δt. Thus, Δt should not be chosen too large.

2.3. Friction models

The steady component in the expression for the head loss is simply taken as the head loss in steady flow. This is well-known as the Darcy-Weisbach equation. Expressed per unit length, the steady part of the head loss in a pipe with diameter, D, is

$$h_{f,s} = f\frac{Q^2}{2gDA^2} \tag{7}$$

where the friction factor, f, can be found from Moody's diagram or a formula approximating Moody's diagram such as Haaland's or Colebrook's equation. For the simulations presented in this paper, Haaland's equation was used. The quasi-steady friction model uses head loss relation for steady flow, but updates the flow variables with each time step. The unsteady term is zero in the quasi-steady approach [3].

Different expressions for the unsteady friction component have been proposed. Vítkovský's formulation of the unsteady friction term takes the sign of the convection term in Brunone's model into account, and is expressed per unit length as follows [8]

$$h_{f,u} = \frac{kD}{V|V|}\left(\frac{\partial V}{\partial t} + a\text{sign}(V)\left|\frac{\partial V}{\partial x}\right|\right)\frac{Q^2}{2gDA^2} \tag{8}$$

where k is the Brunone friction coefficient which can be given by $k = \frac{\sqrt{C}}{2}$ with $C = 0.00476$ for laminar flow and $C = \frac{7.41}{Re^{\log\left(\frac{14.3}{Re^{0.05}}\right)}}$ for turbulent flow. For slow transient flow where the speed of sound, a, is assumed to go towards infinity, the model can be modified in the following way [9]

$$h_{f,u} = \frac{kD}{V|V|}\left|\frac{dV}{dt}\right| \cdot \text{sign}(V)\frac{Q^2}{2gDA^2} \tag{9}$$

Bergset [9] developed a one-term model for the friction loss based on the quasi-steady model. The friction expression was modified by a term taking the velocity change into account, as seen in equation (10). The model was then implemented in the same way as the quasi-steady model, by updating the friction factor to correspond with the current Reynolds number. Per unit length the proposed head loss was as follows

$$h_f = B^{\frac{1}{g}\left(\frac{\partial V}{\partial t} + V\frac{\partial V}{\partial x}\right)} \cdot f \cdot \frac{Q|Q|}{2gDA^2} \tag{10}$$

The proposed expression for the constant B was

$$B = \left(\frac{f_1}{f_2} \cdot \left(\frac{D_1}{D_2}\right)^5\right)^{g\Delta x/(V_1(V_2 - V_1))} \tag{11}$$

where the subscripts 1 and 2 denote sections of a pipe with different diameter.

3. Experiment

A drawing of the test rig which was used for the experiments can be seen in figure 1. The rig consists of an upper reservoir, a 21 m long headrace tunnel, a surge shaft and siphon system. The reservoir has a spillway which ensures that the water level in the reservoir stays constant

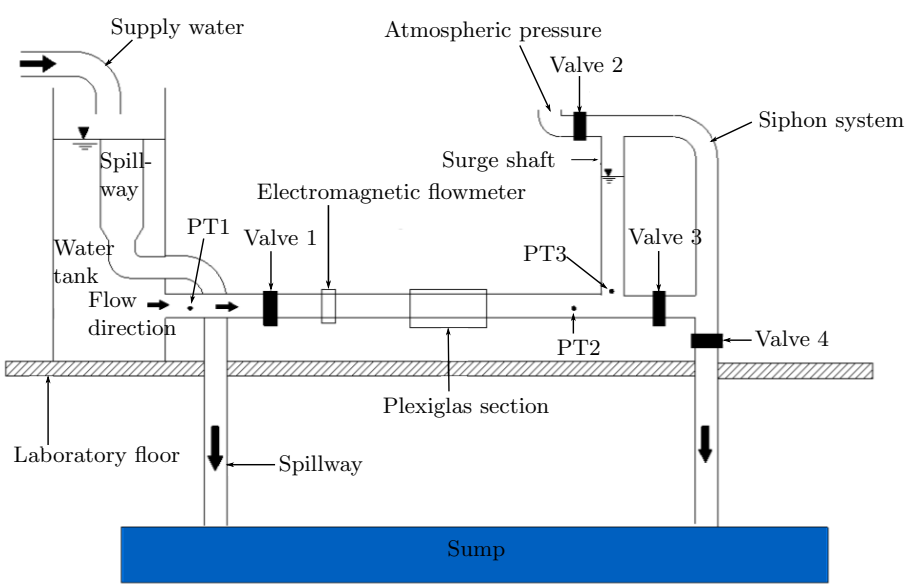

Figure 1: Simplified drawing of the dynamic test rig in the Waterpower Laboratory. Figure from [9], not drawn to scale.

at 2 mWC. The pipe is 0.15 m in diameter and made of steel with a roughness coefficient of 0.002 mm, except for a small pipe section which is made of Plexiglas.

Measurements were done with three UNIK 5000 pressure transducers from GE Druck, located at three different places of the rig as seen in figure 1. An electromagnetic flowmeter from Krohne, called OPTIFLUX 2300C, was used for measurements of volume flow. Data acquisition from the measuring instruments was done with a NI USB-6211 device, and sampling was done at a frequency of 10 Hz.

The fluid in the experiment was water with an assumed dynamic viscosity of 1.138e-3 kg/(ms). Initial flow rates ranging from 0.0033 m^3/s to 0.0015 m^3/s were tested. Valve 1 through 3 were open initially, while valve 4 was adjusted to control the flow rate. The mass oscillations were induced in the system by manually closing a butterfly valve downstream of the surge shaft, valve 3 in figure 1.

4. Results

The simulations were done in MATLAB. The Euler method was used to solve the initial value problem, with initial conditions for the flow rate as given by the measured flow rate before valve closure. Different time steps were tried, and the results presented here are from the simulations with time step $\Delta t = 0.01$.

The results for the different initial flow rates showed the same tendencies so results for only one flow rate is presented here, flow rate 0.0033 m^3/s.

The simulations with the quasi-steady friction model, Vítkovský's friction model and the one-term model is plotted together with measurements of the pressure from one of the experimental runs, in figure 2a, 2b, and 2c, respectively. The pressure measurements are from the third pressure transducer, PT3, in figure 1, situated in the surge shaft.

The three friction models performs quite similarly. They all model the first peak accurately. But with time, none of the models provide enough damping compared with the damping measured in the experiment.

Vítkovský's model performs marginally better than the quasi-steady model. This is difficult to see from plots in figure 2a and 2b, however when the difference between the simulated results and the measured result is studied at each local extrema, one can see that Vítkovský's model provides a slightly larger frictional loss than the quasi-steady model. This can be seen in table 1 where the mean and largest absolute difference between the measurements and the simulations are presented.

Table 1: Mean absolute difference and largest absolute difference between the simulations and experimental results.

Model	Mean absolute difference (mWC)	Largest absolute difference (mWC)
Quasi-steady	0.0543	0.0757
Vítkovský	0.0519	0.0741
One-term	0.0543	0.0757
Modified one-term	0.0143	0.0399

The quasi-steady model as seen in figure 2a and the one-term model as seen in figure 2c turns out to be very similar since the correction term in the one-term model becomes approximately 1. The coefficient B has an exponent which is on average of the order e-6 during the time period for the oscillations. In this project, B, was found in the same way as Bergset proposed in [9]. With this method, the B will be completely dependent on the diameter change. For this rig there is no diameter change, and the diameter D_2 was arbitrarily chosen to be the same as Bergset used. Simply choosing a different D_2 will therefore yield completely different results. The D_2 value

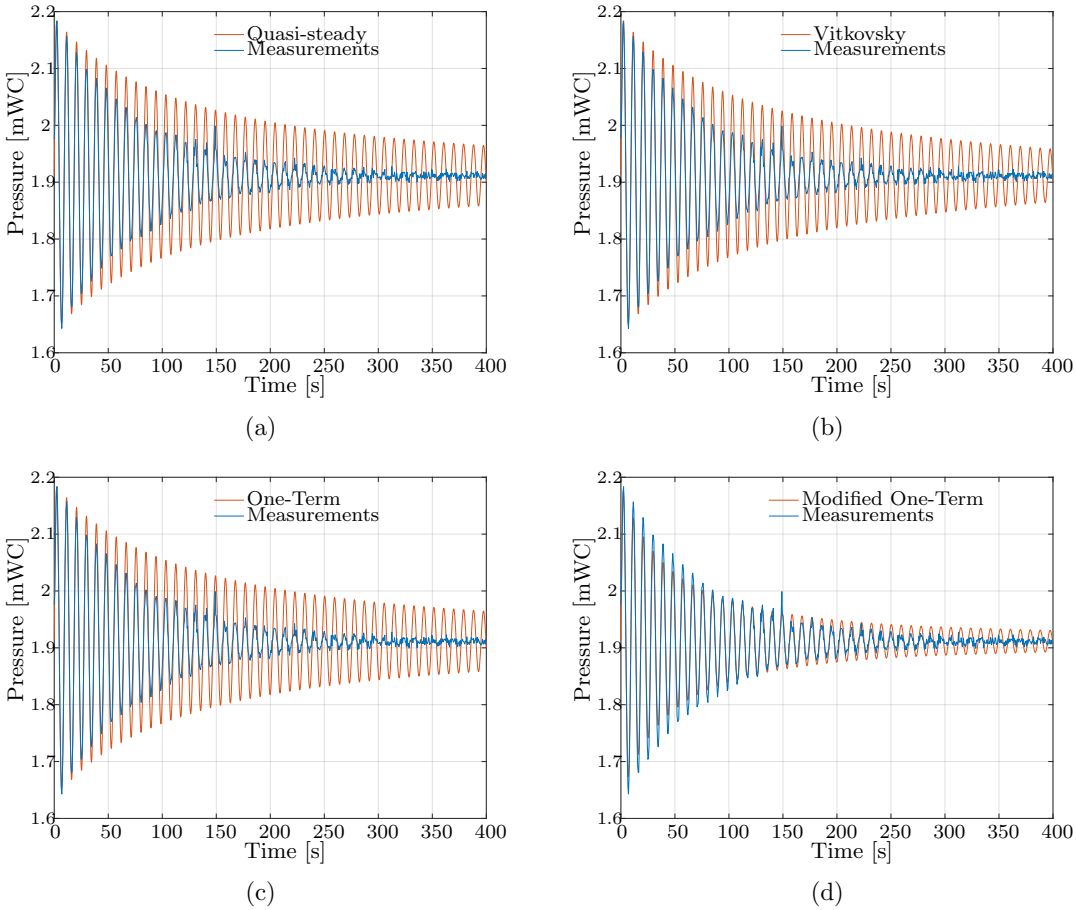

Figure 2: Measurements of pressure oscillations compared with simulations with (a) the quasi-steady model, (b) Vítkovský's model, (c) the one-term model, and (d) the modified one-term model.

was set to 0.325 m, and with the flow rate from this experiment, 0.0033 m^3/s, this resulted in a B equal to 8.1250e+05. However, as the exponent is so small the value of B doesn't really matter much in the case tested, as the whole correction term will tend towards 1.

In an attempt to better match the one-term model to the experimental results, different modifications were tested. As the exponent in the correction term is so small, simply increasing the value of B did not help much. The best way that was found was to multiply the friction loss by a factor larger than one. Through trial and error it was found that multiplication by 3.2 yielded the best results. This modification of the one-term model can be seen in figure 2d.

After this modification, the model yields too much damping in the beginning and for about the first 140 s, while it does not yield enough damping towards the end. As for the other three simulations, the pressure waves are not fully damped out.

The modification of the one-term model reduces the mean absolute difference between the simulations and the experimental results by nearly 74 % compared with the original one-term model. The largest difference between the simulation and experimental results in a single extrema is reduced by 47 %.

The modification improved the fit of the one-term model compared with the experimental

results, however the fact that it yields too much damping in the beginning is undesirable. Thus, further investigations of how the friction models can be modified to accurately predict the friction loss for oscillating flow should be done.

5. Conclusion

Simulations with the quasi-steady friction model, Vítkovský's formulation of Brunone's friction model and the one-term friction model have been compared with experimental measurements. The models perform quite similarly. The model by Vítkovský performs only slightly better than the other two. They all match well for the first peak, but for the following peaks they do not yield enough damping of the oscillations. A modification of the one-term model was also investigated, in which the friction term was multiplied by a constant. This resulted in more damping, however the fit for the first peaks are then not satisfactory as the model yields too much damping for the first peaks.

6. Further work

Further investigations of the characteristics of transient flow should be done. More measurements of mass oscillations should therefore be performed, and finding measurement techniques that can give more detailed insight into the flow characteristics is essential. For example, particle image velocimetry, laser Doppler anemometry or constant temperature anemometry could be considered as measuring techniques which could increase the knowledge of the velocity profile and the shear stress in slow transient flow.

In this paper, the governing equations for transient flow were simplified by assuming that the mass oscillations act as a rigid liquid column, thus neglecting the compressibility of the water and the elastic effects of the pipe. Other methods of solving the partial differential equations such as the well-known method of characteristics could therefore be used instead, as this takes the compressibility and elasticity into account.

The unsteady friction models do not yield enough damping of mass oscillations, and further research must be done to find good modifications of the models so that they match better with experimental measurements.

Acknowledgments

Thanks are extended to the Waterpower Laboratory at NTNU and their employees for their help and guidance.

References

[1] J. P. Tullis. *Hydraulics of Pipelines: Pumps, Valves, Cavitation, Transients.* John Wiley & Sons, 1989.

[2] M.H. Chaudhry. *Applied Hydraulic Transients.* Springer, 3rd edition, 2014.

[3] M.S. Ghidaoui, M. Zhao, D.A. McInnis, and D.H. Axworthy. A review of water hammer theory and practice. *Applied Mechanics Reviews*, 58:49–75, 2005.

[4] D. Stephenson. *Developments in water science: Pipeflow analysis.* Elsevier, 1984.

[5] F.M. White. *Fluid Mechanics.* McGraw-Hill, 7th edition edition, 2011.

[6] Y.A. Çengel and J.M. Cimbala. *Fluid Mechanics: Fundamentals and applications.* McGraw-Hill, 2006.

[7] J.W. Daily, W.L. Hankey, R.W. Olive, and J.M. Jordaan. Resistance coefficients for accelerated and decelerated flows through smooth tubes and orifices. *ASME*, 1955.

[8] A. Bergant, A.R. Simpson, and J. Vítkovský. Developments in unsteady pipe friction modelling. *Journal of Hydraulic Research*, 39(3):249–257, 2001.

[9] I. Bergset. Investigations of a harmonic oscillatory flow, 2017.

[10] E.B. Wylie, V.L. Streeter, and L. Suo. *Fluid Transients in Systems*. Prentice-Hall, Englewood Cliffs, NJ, 1993.